A Parametric Study of Blended Wing Body Geometry Using a Hybridization Factor and CST Approach

Pelayo Casanovas de Alós

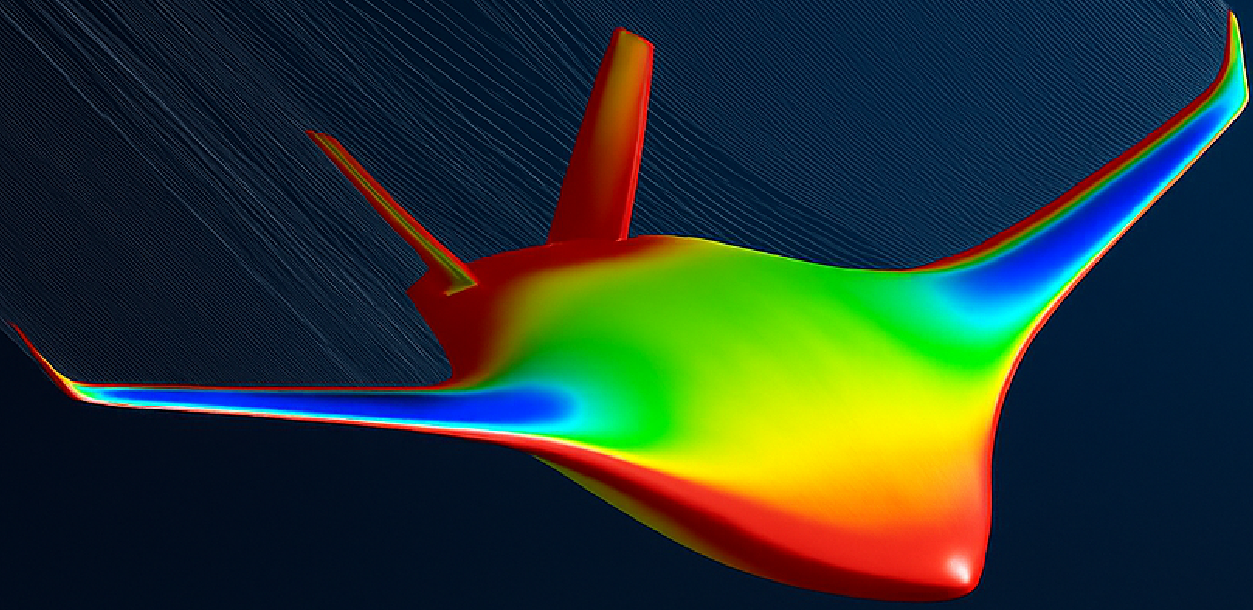

A Parametric Study of Blended Wing Body Geometry Using a Hybridization Factor and CST Approach

by

Pelayo Casanovas de Alós

in partial fulfillment of the requirements for the degree of

Master of Science
in Aerospace Engineering

at the Delft University of Technology,
to be defended publicly on Monday February 23rd, 2026 at 2:00 PM.

Supervisor:	Dr. ir. F. Orefice
Thesis committee:	Dr. ir. C. Varriale
	Dr. ir. N. Yue

Preface

This project marks the end of a challenging and fruitful masters degree that has shown me what it means to be an aerospace engineer. The quality of education at TU Delft has surpassed my expectations and, although challenging, has taught me much more than I imagined. This work was initiated thanks to Rick and Zach from Aerohauler, who provided valuable connections to make this work possible. I would like to thank my supervisor, Dr. Orefice, for his valuable feedback and making time to meet every week. I want to thank my family for their constant support and care during this Master's degree. This work would not have been possible without the assistance of my friends and fellow colleagues that I met through this program, especially Camo, Dani, Robin, Manu, Pablo and Diego, who always provided support and a good laugh when I needed it the most. Finally, I would like to thank my girlfriend, Irene, for always showing me love and understanding throughout this process.

Pelayo Casanovas de Alós
Delft, January 2026

Contents

List of Figures

List of Tables

Nomenclature

α	Angle of attack [deg]
χ	Hybridization factor [-]
Δz	Vertical displacement [m]
η	Spanwise coordinate [-]
Γ	Dihedral angle [deg]
κ	Fuselage roundness exponent [-]
Λ	Quarter-chord sweep angle [deg]
$\Lambda_{C/4}$	Quarter-chord sweep angle [deg]
Λ_{LE}	Leading-edge sweep angle [deg]
ν	Curvature vertex position [-]
ψ	Normalized chordwise coordinate [-]
ρ	Air density [kg/m^3]
θ_{twist}	Wing twist angle [deg]
ζ	Streamwise coordinate [-]
a	Shape factor or Bernstein coefficient[-]
a_c	Chord shape factor [-]
a_i	Incidence shape factor [-]
a_t	Thickness shape factor [-]
a_x	x-position shape factor [-]
a_z	z-position shape factor [-]
b	Wingspan [m]
C	Class function [-]
c	Chord length [m]
c_{root}	Root chord length [m]
c_{tip}	Tip chord length [m]
C_D	Drag coefficient [-]
C_L	Lift coefficient [-]

C_M	Moment coefficient [-]
C_L/C_D	Aerodynamic efficiency [-]
$C_{M\alpha}$	Pitching moment derivative w.r.t. angle of attack [-]
$i(\eta)$	Spanwise incidence angle distribution [deg]
N	Class function exponent [-]
R_{nose}	Nose radius [m]
R_e	Reynolds number [-]
S	Wing reference area [m^2]
t/c	Thickness-to-chord ratio [-]
V	Velocity [m/s]
V_f	Fairing volume [m^3]
x_{LE}	Leading-edge x-position [m]
Y_i	Non-dimensional spanwise airfoil positions [-]
z	Vertical coordinate [m]
AC	Aerodynamic Center
BWB	Blended Wing Body
CAD	Computer-Aided Design
CFD	Computational Fluid Dynamics
CG	Center of Gravity
CST	Class-Shape Transformation
HBWB	Hybrid Blended Wing Body
MAC	Mean Aerodynamic Chord
NP	Neutral Point
NURBS	Non-Uniform Rational B-Splines
PARSEC	Parameterized Section Definition
TAW	Tube-and-Wing configuration

Chapter 1

Introduction

The aviation industry accounts for 2.4% of global carbon emissions. Emerging research is indicating that non-CO_2 effects, like NO_x and contrails, are also contributing to the effective radiative forcing and that these effects are contributing up to three times the warming effect of CO_2 emissions alone [1]. The large environmental impact of transport led to the launching of the European Green Deal in 2019, which aims to cut down transport emissions by 90% by 2050 [2]. This is a major challenge for aviation as it is still quite far from transitioning to completely sustainable fuels, like SAF and green hydrogen, for both financial and technological reasons [3][4]. This is the change needed to keep conventional aircraft designs flying; however, emissions can also be reduced through improved aerodynamic efficiency enabled by new design concepts [5]. This is because incremental improvements to the classical design are yielding smaller and smaller returns [6]. The question posed by NASA scientist Dennis Bushnell in 1988 remains as relevant today as it was then: "is there a renaissance for long-haul transport?" [6]. This question has sparked a renewed interest in unconventional aircraft configurations, particularly the Blended Wing Body (BWB), which is an aircraft that has its fuselage integrated within the structure of the wing. A Hybrid Blended Wing Body (HBWB) is similar to the BWB but has a clearer distinction between the fuselage and wing. The creation of these concepts was ignited by the idea of changing the fuselage geometry so that it can also provide lift. By doing so, BWB aircraft promise substantial improvements in aerodynamic efficiency, fuel economy, and internal volume [7]. The increased internal volume also facilitates the integration of hydrogen storage and propulsion systems [8]. Studies have demonstrated lift-to-drag ratio improvements of 20% or more compared to conventional configurations, along with significant reductions in fuel consumption and emissions [5]. These performance gains make BWB designs especially attractive for meeting future sustainability goals in aviation, like being net-zero by 2050.

However, these benefits were already being discovered as early as the 1990's and the first commercial blended wing body has yet to begin manufacturing [9]. Therefore, there are still barriers that are preventing its entrance to the market, especially for passenger applications. [10][5][11]. As we overcome these barriers, aerospace engineers need to ensure that the adequate design and optimization tools are ready to support future development. Current parametric models excel at representing conventional aircraft, which makes it easier to create multiple design iterations and optimizations [3]. When moving to unconventional configurations, there is no specific methodology that can design all the BWB or HBWB configurations that has been established in literature without being constrained to specific geometric features [12]. There is a wide variety of BWB/HBWB designs that have been evaluated in literature, but there are large differences from one another which means that most geometric features are tailored to the given design. Most efforts consist of evaluating or optimizing the aircraft based on their own specific planform and layout [13][14][15]. Current parametric frameworks are usually configuration-specific and cannot represent both conventional and blended configurations with a unified parameter set, greatly limiting design exploration. What is needed is a design tool that can harmonize all types of BWB and HBWB configurations, with the ability to also begin from a conventional geometry. This will enable designers to systematically explore how the integration of the fuselage and wing affects aerodynamic performance, stability and internal volume requirements. To do this, the design tool will need to be able to capture the features from a wide range of designs, namely the wing, fuselage and fairing.

This tool will generate an aircraft geometry and will be integrated with an aerodynamic analysis. It will not include structural or aeroelastic analysis as the focus at this stage is more specifically on the aerodynamics of the outer mold line.

1.1 Research Questions

This problem will be approached in the following work by defining the aircraft with a novel geometric parameter and using Class Shape Function Transformations to control the outer mold line (OML) of the fairing. The main research question motivating this work is defined as follows:

Research Question

What are the hypotheses and methods to parametrize the geometric representation of an aircraft digital model regardless of the degree of integration between fuselage and wing, ranging from the wing-body configuration to the blended wing-body?

This then invokes the following sub questions:

- Is it possible to define a unique hybridization factor that allows a parametric and coherent representation of the different levels of integration between fuselage and wing?
- What are the geometric features and associated parameters that cannot be directly related to the level of integration between fuselage and wing?
- What are the aerodynamic effects related to varying wing parameters for different levels of integration between wing and fuselage?
- What are the design parameters that may drive the selection of the most promising integration level?
- Is there any level of integration between the wing and fuselage that can be considered globally an optimum?

To answer these questions, this work develops a parametric modeling framework based on the Class-Shape Transformation (CST) method, enhanced with a new geometrical parameter called the hybridization factor to enable unified representation of aircraft ranging from conventional layouts to fully blended configurations. The framework is validated against existing aircraft, which includes the Embraer EMB-145, Airbus A320, MIT Aurora D8, and a TU Delft BWB concept, to demonstrate its capability to accurately reproduce diverse configurations with varying specific features whilst using a consistent parameterization.

Following validation, the framework is applied to a design optimization study focused on a hydrogen-powered cargo aircraft concept. By systematically varying the hybridization factor and utilizing the novel parameters, it opens up for the analysis of its effects on aerodynamic efficiency, volumetric capacity, and stability, this research identifies a few optimal configurations that balance performance with the necessary requirements.

1.2 Background of Blended Wing Body Aircraft

This section aims to review the historical proceedings as well as modern ideas that have led to an increase in popularity and interest in studying blended wing-body aircraft. It will also include the reasoning behind pursuing such a study as well as the drawbacks that are currently preventing it from being implemented as a commercial aircraft. A table summarizing the performance claims found in literature will also be presented.

1.2.1 Definition Of A Blended Wing Body

A description of the BWB as written by Daniel P. Raymer in his *Aircraft Design: A Conceptual Approach*[16]:

> The Blended Wing-Body is basically a flying wing with a delta-shaped wing/fuselage in the center, large enough for a passenger cabin [and] the center section is blended into the wing panels. This concept reduces the total wetted area (the area of the aircraft in contact with the external airflow) of the airplane and, with its deep center section, improves structural efficiency. The BWB has about half of the root-bending stresses of a conventional configuration. The wing-tip mounted vertical tails also act as winglets to reduce drag due to lift. BWB requires relaxed static stability and an automated flight control system to fly efficiently, optimize span loading, and avoid the need for a tail.

This definition is widely known and used, but it is slightly outdated due to the fact that it says a BWB is a "flying wing with a delta-shaped wing/fuselage". This is no longer completely true, as some new concepts are completely blended, like the Flying V, which means it does not have a distinct fuselage section as it is fully integrated in the wing. For the purpose of this project, a new, well-rounded definition of a BWB will be proposed:

> A Blended Wing-Body is an aircraft in which its lifting surface and fuselage are fused together so that they have similar aerodynamic behaviour and a reduction in overall drag. The degree of blending describes how much of the aircraft is fuselage and fairing and how much is purely wing, this is denoted as the *hybridization factor*. An aircraft with a hybridization factor and center thickness large enough to encapsulate its fuselage or pressure vessel is deemed a hybrid blended wing body. When the hybridization factor is equal to 1, then there is no distinction between the fuselage and wing.

The hybridization factor will be more carefully explained in the coming chapters.

1.2.2 Introduction of the concept

A blended wing-body (BWB) aircraft design is pursued primarily for its superior aerodynamic efficiency and fuel savings[9][5]. By seamlessly integrating the wings with the main body, the BWB configuration reduces drag and allows for more uniform lift distribution across the structure. This results in improved fuel economy and lower emissions compared to conventional tube-and-wing aircraft [17]. Additionally, the design offers greater internal volume, which can be used for increased passenger capacity or innovative cargo layouts, as well as a reduction in wing bending moment. These advantages make BWB designs particularly attractive for meeting future sustainability goals in aviation.

With these great advantages come significant disadvantages and limitations that still prevent the introduction of this concept. The structure required for BWB is very complex and demands advanced materials and manufacturing processes, which are still not viable for large productions [18]. The non-circular fuselage section also incurs weight penalties as it needs additional reinforcement to handle the pressure loads [5] [19]. BWB concepts are larger in wingspan to accommodate the pressure vessel and improve efficiency, this leads to issues with airport infrastructure as the aircraft will not meet the necessary apron constraints [5]. Another issue is the problem with emergency evacuations as the shape of the cabin makes it more complicated for certain passenger seats to reach the exit [10]. Passenger comfort is a major area of concern for BWB aircraft as window seats and natural light will be greatly limited. A survey performed by Wittman revealed that 33.1% of participants ranked the availability of external view as very important, which was the largest percentage compared to the other options [11]. Airport infrastructure, emergency exits and passenger comfort are generally more of an issue for passenger aircraft, which means the possibility of a cargo BWB is a more plausible option for the near future.

1.2.3 Evolution of the Blended Wing Body

The Dunne was built in 1910 and was essentially a swept-back bi-plane without tail surfaces, as seen in Figure 1.1. The intention of the sweep was to provide similar control and stability characteristics to that of a regular tailed aircraft. This line of aircraft, pioneered by J.W. Dunne, is regarded as being one of the first "fixed-wings". Some may claim that this was one of the first ideas that evolved into the blended-wing body aircraft that is known today.

Jack Northrop was one of the first to pioneer the "flying wing" concept. He began designing and testing flying-wings in the 1930's. He first started off with the N-1M, which was an all-wing twin engine bomber with drooped wingtips [20].The angle of these wingtips could be manually adjusted on the ground to test the stability of the aircraft. The outboard wing sections could also be adjusted to change the sweep angle. This can be seen in Figure 1.2, as there is a slightly different colour of paint where the inboard and outboard sections meet. Changing the shape of this connecting "wedge" would adjust the sweep. Having an aircraft with no tail meant that there had to be a solution for the directional stability and control. Most aircraft of the time featured a vertical tail with a rudder that allowed for yaw control and directional stability in crosswind conditions. The propeller fairings and drooped wing tips provided a some lateral force to keep the aircraft on its designated flight path. The drooped wing tips also allowed for directional control. This aircraft proved that the flying wing was a viable concept, which sparked the idea that there was more than one way to get a vehicle airborne and control it. The next aircraft built by Jack Northrop and his team was the N-9M which featured a more powerful engine allowing it to reach speeds of 257 mph at 7000 feet [20]. The drooped wing tips had been scrapped on this model and were replaced by clamshell split-flap rudders, depicted in Figure 1.3. During the flight testing of the N-9M in 1943, the aircraft experienced severe control reversal and crashed. This control reversal pushed the stick into test-pilot Max Constant's chest, obstructing him from ejecting out [20]. Crashes like these were unfortunately common during this time as flying was relatively new and unconventional concepts were even more risky. New concepts, like the flying wing, unveiled aerodynamic phenomena that had not been encountered before, making it extremely dangerous for test pilots. To this day, these aircraft show us that, although they may be able to fly, careful consideration must be taken with the design of the overall geometry and control surface geometry. Particularly, the placement of control surfaces plays a very important role with these aircraft as most of these surfaces will have more than one function. In 1941, he was designated to design the XB-35 (Figure 1.4), a large propeller-pushed flying wing that served as a heavy bomber. The lessons learnt from the N-1M and N9-M were reflected in the XB-35. The XB-35 could carry more weight, fly faster and fly farther than any other conventional configuration at the time [21]. The development of this giant 4-engine piston-powered aircraft was one of the only programs that drew the interest of the military, as it successfully flew. Soon after, Northrop came up with the YB-49 and YRB-49, which was an eight-engined and six-engined jet aircraft [22]. This aircraft greatly resembled the XB-35 but now featured vertical stabilizers. This is likely due to the fact that the jet engines were placed on the trailing edge of the wing so they had no vertical fairing. This shows one of the main drawbacks of a flying wing, which is directional stability and control. The eight-engined variant is shown in Figure 1.5. These aircraft were marvels in innovation but were deemed unsuitable for military applications, so most of these programs were canceled. The main issue was that these aircraft had a significant loss in performance when reaching compressible flow regimes [22]. This was mainly due to the divergent longitudinal pitching and roll-yaw coupling that resulted in directional instability.

It was not until digital electronic flight controls were developed that the flying wings began performing at practical levels [22]. The digital controls allowed pilots to fly through the transonic regime without having to deal with varying divergent motions and even control reversal. This was shown many years later through the Northrop B-2 Spirit stealth bomber (Figure 1.6) that made its first flight in 1989, almost 40 years after the YB-49. Although many flying wing designs have been made and tested, not many have lived past the experimental stage. The B-2 Spirit has seen many applications throughout the 2000's and is still being upgraded to this day. Since then the flying wing idea has developed greatly, which has led to many novel and promising designs. Some key examples of this are NASA's BWB, like the X-48, and TU Delft's Flying V, which have been internationally recognized as possible alternatives for the tube-and-wing.

Figure 1.1: The Burgess-Dunne was one of the first tailless aircraft and featured a swept-back wing [23]

Figure 1.2: The Northrop N-1M [20]

Figure 1.3: The Northrop N-9MB showcasing its clamshell split-flap rudders at the Chino Warbird Show on October 8, 2000 [24]

Figure 1.4: The XB-35 [21]

Figure 1.5: The Northrop YB-49A at Hawthorne, CA, December 23, 1948 [22]

Figure 1.6: Northrop B-2 Spirit stealth bomber [22]

In the current world of aviation, many people are pushing to redefine what the best way to fly is, but the classic tube-and-wing (TAW) is very difficult to beat. In the 1980's, NASA scientist Dennis Bushnell was strongly promoting researchers to think of fresh and revolutionary ideas to combat antiquated challenges. In 1988 he gathered with leaders of the aeronautical community and asked if there was a renaissance for long-haul transport [6]. He asked this question because he saw that improvements to aircraft performance were declining. The tube and wing was getting close to its best aerodynamic efficiency. This sparked Robert H. Liebeck's interest to investigate unconventional aircraft. Soon, him and his associates drafted up one of the first designs of a blended-wing body aircraft (BWB). Initially, they began by creating an aircraft that was composed of various cylindrical pressure vessels, stemming from the concept of a classic cylindrical fuselage. Because of this, the first design looked similar to a MD-12 with a very large wing-body fairing [9].

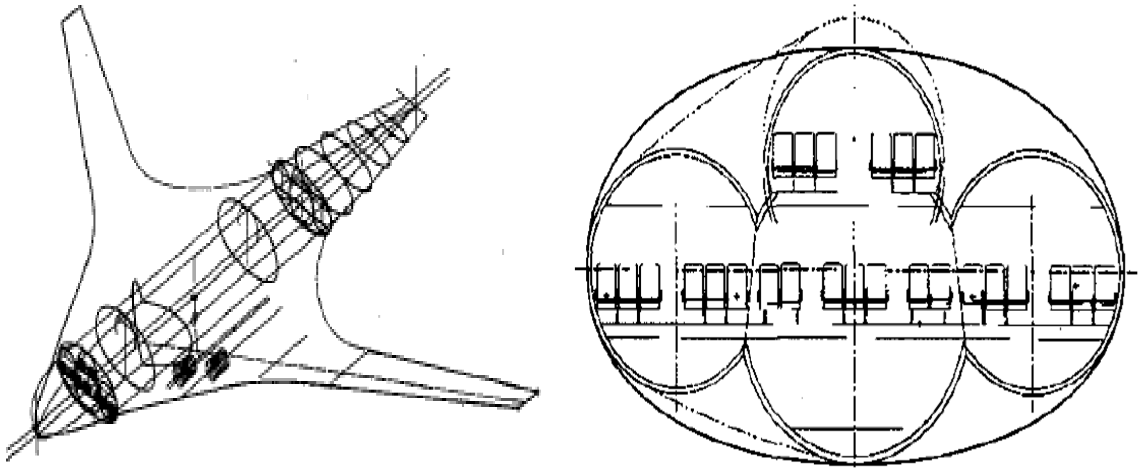

(a) (b)

Figure 1.7: Initial layout showcasing the pressure vessel arrangement [9]

As this seemed to be edging closer towards a conventional configuration, they decided to abandon the requirement of a cylindrical pressure vessel and neglected the structural limitations, assuming they would be addressed in the future [9]. This allowed Liebeck and his team to get creative and further enhance the aerodynamic viability of their concept. Now, the design could be thinner near the fuselage section, have a wider wing span and larger wing-body fillets.

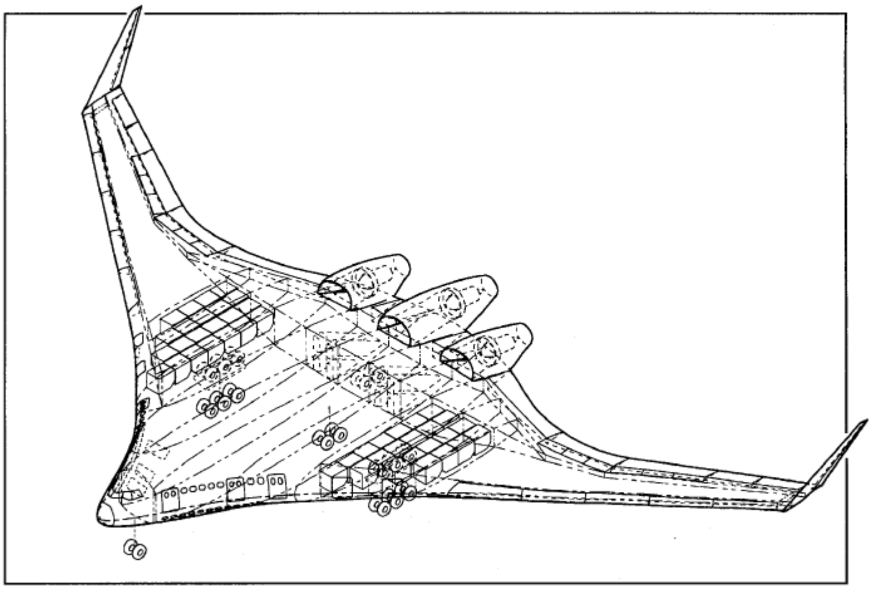

Figure 1.8: The Blended-Wing-Body design of Liebeck et al. [9]

This design has become one of the baseline designs when considering a blended wing body. Liebeck's BWB claimed they could reduce up to 27% fuel burn, increase the lift-to-drag ratio by 20% and reduce the operating empty weight by 12%. [9]. NASA has promoted this idea further and has created strategic goals known as the New Aviation Horizons (NAH), which focus on reducing emissions, fuel burn and noise levels. A company known as DZYNE Technologies Inc. has produced a study that highlights the BWB's capability of meeting these goals and its ability to enter the the regional jet and single-aisle jet markets [17]. They claim that the aerodynamic efficiency is 25% and 30% greater than the TAW configuration and that this can be amplified after optimizing the geometry for a reduced fuel weight.

A very important feature that is mentioned in this study is the "kink" region which is denoted as a "critical station" for achieving favourable aerodynamics since it is the area of highest stress. By design, this is a very important parameter for low-speed stall and transonic buffet. This is due to its ability to generate a leading-edge vortex that washes over the upper surface of the wing, which can be beneficial in postponing separation at high-angles of attack.

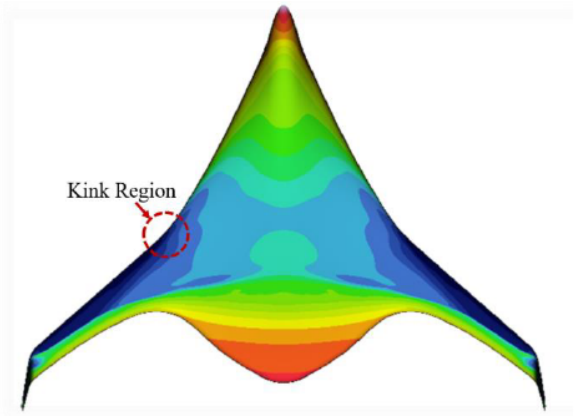

Figure 5: Ascent 1000 planform view of pressure coefficient contours at cruise.

Figure 1.9: DZYNE Ascent 1000 pressure contours [17]

This study also goes into some detail regarding the issues regarding control authority and stability. Their configuration has short-coupled controls compared to TAW. This means that there is a pitch-to-flightpath control lag, but this was addressed by the X-48 control system [17]. They also stated that elevons cause a significant loss in lift during take-off rotation, pivot-piston landing gear were implemented to remedy this issue.

Table 1.1 highlights the operational differences between the DZYNE Ascent 1000 and some of the best-in-class aircraft in previous years.

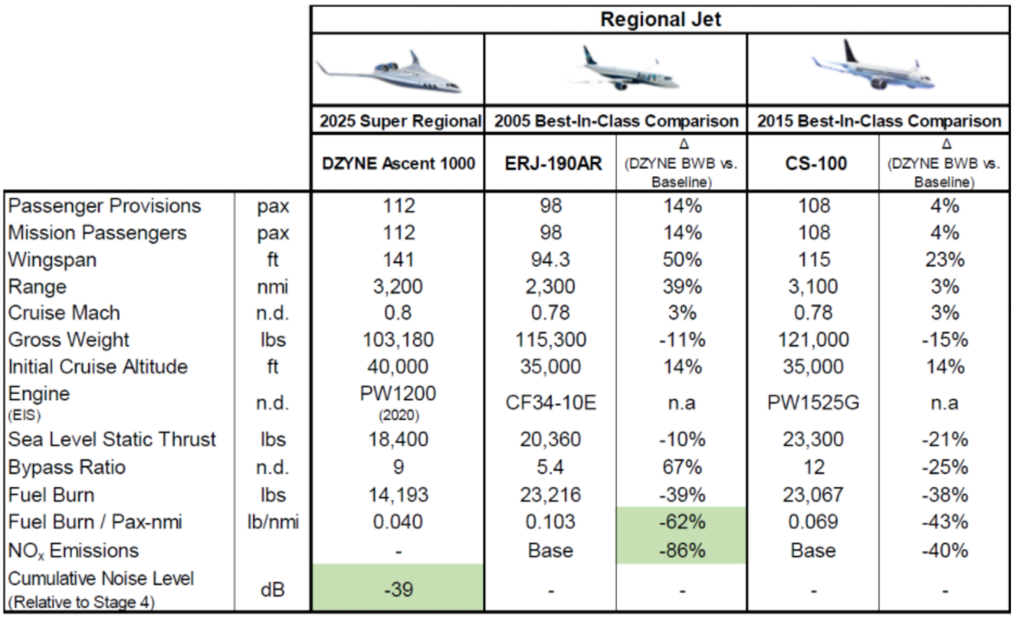

		Regional Jet				
		2025 Super Regional	2005 Best-In-Class Comparison		2015 Best-In-Class Comparison	
		DZYNE Ascent 1000	ERJ-190AR	Δ (DZYNE BWB vs. Baseline)	CS-100	Δ (DZYNE BWB vs. Baseline)
Passenger Provisions	pax	112	98	14%	108	4%
Mission Passengers	pax	112	98	14%	108	4%
Wingspan	ft	141	94.3	50%	115	23%
Range	nmi	3,200	2,300	39%	3,100	3%
Cruise Mach	n.d.	0.8	0.78	3%	0.78	3%
Gross Weight	lbs	103,180	115,300	-11%	121,000	-15%
Initial Cruise Altitude	ft	40,000	35,000	14%	35,000	14%
Engine (EIS)	n.d.	PW1200 (2020)	CF34-10E	n.a	PW1525G	n.a
Sea Level Static Thrust	lbs	18,400	20,360	-10%	23,300	-21%
Bypass Ratio	n.d.	9	5.4	67%	12	-25%
Fuel Burn	lbs	14,193	23,216	-39%	23,067	-38%
Fuel Burn / Pax-nmi	lb/nmi	0.040	0.103	-62%	0.069	-43%
NO_x Emissions		-	Base	-86%	Base	-40%
Cumulative Noise Level (Relative to Stage 4)	dB	-39	-	-	-	-

Table 1.1: BWB Ascent 1000 comparison to 2005 and 2015 best-in-class aircraft [17]

A study done at TU Delft [14] aimed to compare various models of the BWB to their TAW counterpart. This ranged from regional airliners with 156 passengers to larger long-haul airliners with 368 passengers.

This is an important area of research because it directly compares performance and planform of these aircraft, which helps identify the feasibility of such projects. A major concern for the implementation of BWB aircraft in commercial transport is that they may not fit in the same apron as the TAW at airports. But, from this study, it was found that the span of the BWB was only slightly larger than the corresponding TAW, as seen in Figure 1.10. The overall length of the aircraft had a larger difference, being that the BWB was much shorter, but this aspect is likely to be less of a problem compared to the span. They also concluded that a BWB design greatly reduces the overall mass and improved the fuel economy [14].

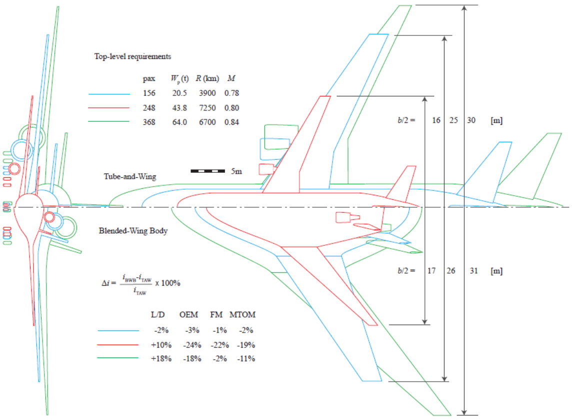

Figure 1.10: Comparison of various BWB and TAW designs with the same top-level requirements [14]

1.2.4 Aerodynamic Performance of Blended Wing Body Aircraft

The performance of BWB aircraft has been extensively analyzed with both experimental and computational methods.A study done by Pang Jung et al. [25] showed that the BWB configuration had a lift-to-drag (L/D) ratio 24% greater than that of a conventional tube and wing. This is very close to the initial prediction made by Liebeck et al., which was around 20% [9]. A handful of other studies have also come to similar figures [26] [27]. The study done by Brown et al. from TU Delft [14] produced some very meaningful results as they compared various sizes of BWB compared to their TAW counterpart. For an aircraft that holds 150 passengers, they concluded that the maximum L/D was greater for the TAW aircraft, around 2.2%. But, for the larger configurations of 250 and 400 passengers, the maximum L/D was greater for the BWB aircraft around 11.1% and 20.4% respectively. This provides very valuable insight into the adequate sizing of a BWB, as it shows that it is not superior for all configurations and must be carefully sized to reap its benefits.

Table 1.2: BWB concepts and their claimed aerodynamic efficiencies

Source	**Efficiency** , L/D
Liebeck et al. [9]	23
Dommelen et al. [28]	27.2
Brown et al. [14]	18
SAX-40 [29]	25
OREIO [30]	23

Chapter 2

Literature Review

This chapter will begin by explaining the geometric features that define a blended wing body. Similar to a conventional aircraft, these features include the wing, fuselage, fairing, as well as the cargo hold and tanks, which will be denoted as the internal volume. Then, a set of parameterization techniques found in literature that describe these objects will be examined. This will be done for both the two-dimensional (2D) and three-dimensional (3D) geometries.

2.1 Features Of A Blended Wing Body

2.1.1 Wing

The wing on a BWB or HBWB now serves as more than just a lifting surface. It needs to have sufficient volume in the center section to fit the pressure vessel and cargo bay. Early designs, like Liebeck et al.[7], already recognized this issue and made valuable insights into how the wing needs to be adjusted and constrained to account for the new design. As an increase in volume is required, the maximum thickness-to-chord ratio increases beyond that of a transonic or supercritical airfoil, around 17% [7]. This is a crucial discovery because supercritical airfoils are the most commonly used in subsonic commercial aviation as they increase lift, reduce drag and improve stability [31]. Another important insight made by Liebeck et al. is that, as the cabin is within the wing, it needs to maintain within a specific angle during cruise, which limits the angle for which the center airfoils can be placed [7]. This then means that the airfoil needs to generate more lift at a lower angle of attack, suggesting the use of positive aft camber [7]. However, Liebeck also states that a BWB configuration is considered trimmed only when the aerodynamic center of pressure coincides with the center of gravity and all control surfaces are neutral. This means that positive static stability requires a reduction in the nose-down pitching moment, which constrains how much positive aft camber can be used [7]. A culmination of these requirements and some others are shown through the second generation BWB presented by Liebeck, seen in Figure 2.1. These initial statements and design considerations served as the baseline for many future BWB designs [28][32][33].

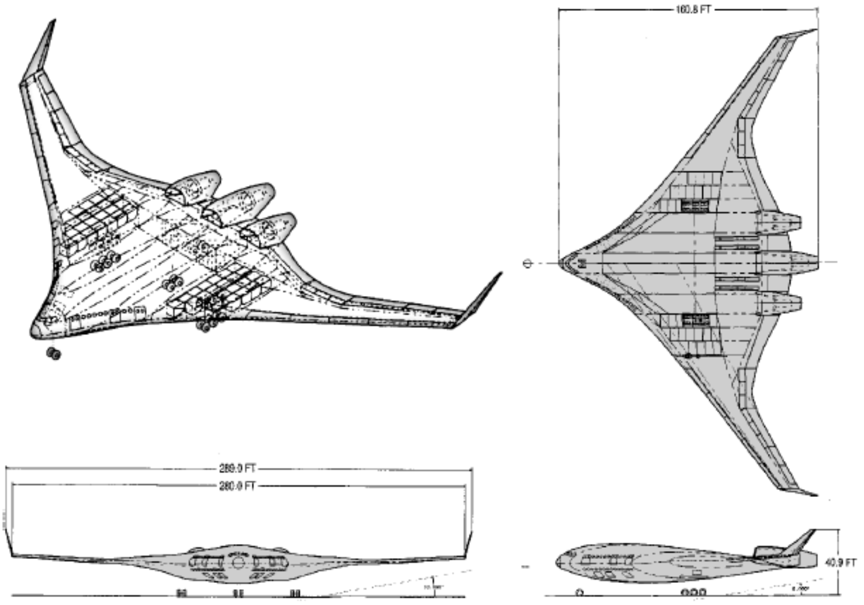

Figure 2.1: Second generation BWB design from Liebeck et al.[7]

2.1.2 Fuselage

The design of the fuselage on a BWB is crucial due to it no longer being cylindrical and becoming enclosed by a lifting surface. One of the main issues with BWB is that its complex shape is structurally problematic, creating a non-cylindrical pressure vessel is not an easy task. Another issue with a lifting fuselage is that it also has to withstand the bending stresses due to the lift. With the development of new structural concepts using composite materials, it could be possible to create such a fuselage. A common concept to tackle this issue is to create an outer and inner shell, the first handles the stresses due to lifting and the latter handles the stresses due to the pressure.

A few studies have been performed to tackle this issue, one done by NASA's LARC explored two shell concepts [34]. The first is the "flat shell" concept where the inner and outer shell follow the same profile, separated by a fixed distance throughout the fuselage. This gap is initially designed with a honeycomb structure in an attempt to reduce weight but maintain high strength. The second is the "vaulted shell" concept where the inner shell resembles more of a cylindrical shell, creating an arch-like shape with the outer shell. This means that there is a variation in the gap between the two shells, as seen below in Figure 2.2. This study concluded that neither concept offered any significant weight or strength advantage over the other, but as the flat-shell is easier to manufacture, it would be the better choice. Because of this, the author explored the possibility of making a double-skin ribbed shell concept, where the honeycomb structure is replaced by simple ribs. With this change, the vaulted concept offered a significant weight advantage over the flat concept. The only drawback being that there are still manufacturing barriers to create this structure, for both conventional and composite construction [34].

A more recent study explores the design of a Columned Multi-Bubble Fuselage (CMBF). This is similar to the previously introduced vaulted shell concept, but now there is the introduction of columns. These columns are in tensile stress to resist the pressurization of the bubbles. They concluded that this method demonstrated significant improvement on sectional weight when compared to a Multi-Bubble Fuselage without columns, but it was still not suitable for resisting bending loads as the deformations under load were too large [35].

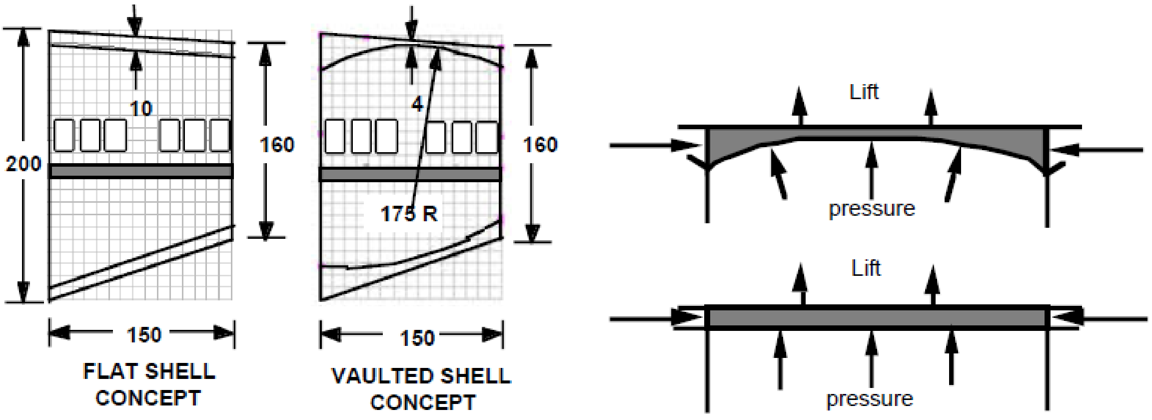

(a) (b)

Figure 2.2: a) Cross sections of the uniform-depth flat shell and the vaulted shell fuselage concept, and b) close up of the resultant forces on each concept [34]

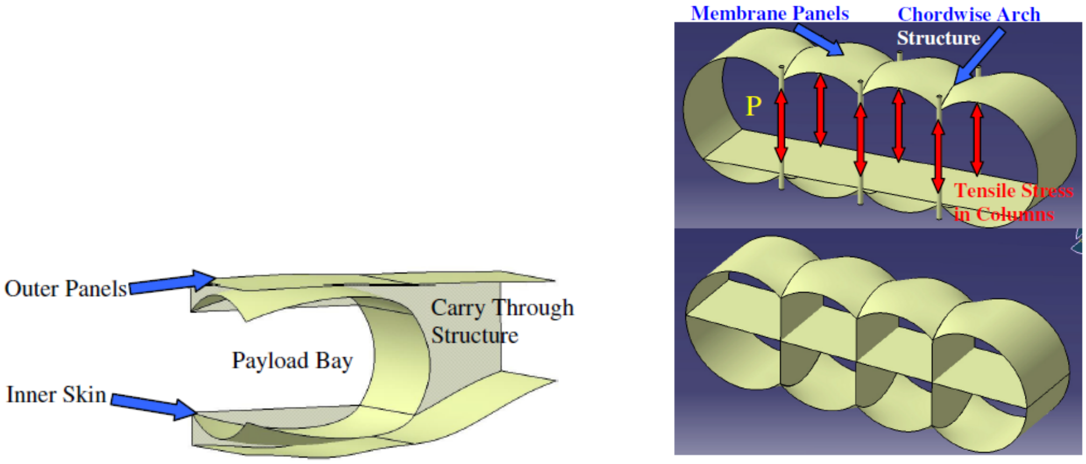

(a) (b)

Figure 2.3: a) Conceptual fuselage section of a BWB, and b) Columned Multi Bubble Fuselage under pressure [35]

A study done by TU Delft explored a new structural concept, which shifted away from the promising multi-bubble idea to a simpler oval configuration. This is done in part because adding vertical members will diminish the space and natural light of the cabin, making it less useful and enjoyable for passengers [19]. They concluded that this concept could be structurally efficient and can be tailored to meet cargo stowage requirements. An issue with this design, and others, is that the oval centerbody cross section does not allow for a smooth wing-body transition, thus requiring aerodynamic fairings [19]. The authors acknowledge the sizing of these fairings as an area that is yet to be investigated. Adequate sizing and shaping of these fairings are crucial to the design of BWB as they need to provide the necessary aerodynamic benefits of shock prevention and vortex generation, whilst still being light in weight.

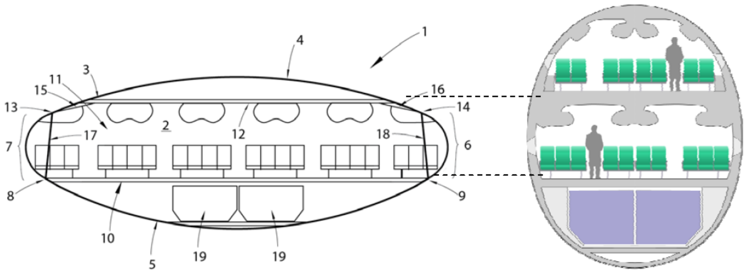

Figure 2.4: Cabin cross section proposed by Vos et al. compared to an A380 cross section [19]

The parametric design of this aircraft was based on first defining the internal cabin dimensions and then placing oval cross sections with a tangency constraint around the cabin, as shown in Figure 2.5[19]. This is a simple way and realistic way to design a structurally-viable fuselage for a BWB. However, it is highly dependent on the cabin dimensions and is only suitable for BWB designs. This can be remedied with the use of a hyper-ellipse distribution of profiles, which is a simple method in which both conventional and unconventional fuselages and cabins can be designed. This will be described in further detail in subsection 3.2.4.

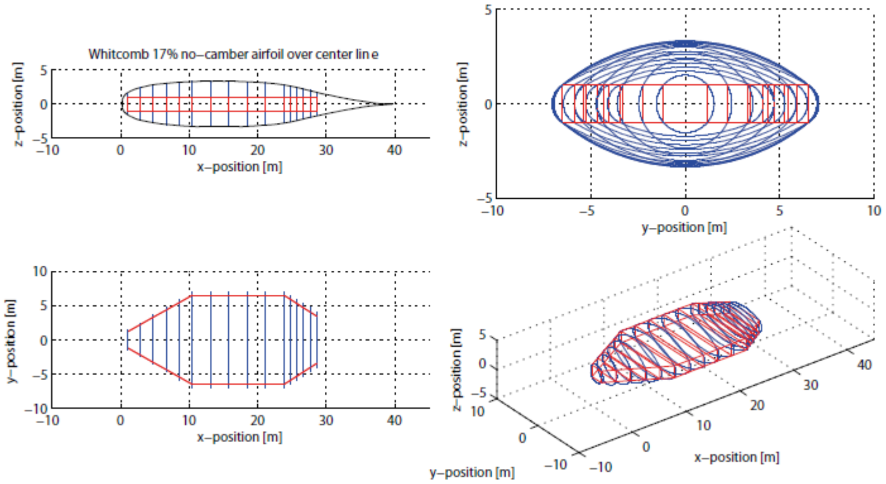

Figure 2.5: Oval BWB fuselage described in [19]

2.1.3 Fairing

Aerodynamic fairing is used on aircraft to blend two components to prevent supervelocities which causes interference drag and the earlier onset of shockwaves. These supervelocities are caused by the junction areas where the 3-D flow interferes with each other and creates an area of increased velocity. This increases the lift coefficient in this area, but this makes it much more prone to shock-induced separation, causing an increase in interference drag [36]. One of the most visible and important fairing on aircraft is the wing-body fairing or wing-root fairing, as seen in Figure 2.6. As the goal of the fairing is to improve the aerodynamics that occur by joining the wing and the body, fairing on the BWB can be considered to be the additional material that is added so that the fuselage can enclosed properly whilst maintaining aerodynamic performance.

Figure 2.6: Wing-body fairing of an Airbus A320 [37]

This area is particularly important because it experiences a large amount of 3-D flow and is very prone to separation if not treated correctly. Usually, the root section experiences lower velocity in the forward part and higher velocity in the rear part. This affects the isobar pattern, making it more prone to a pressure drop and thus likely to cause separation. To remedy this, more curvature is added to the forward part of the root airfoil section and less curvature towards the aft part [36], allowing for a more even velocity distribution. This is for the effects due to the thickness of the root section, but the lift generated in this area also affects the velocity distribution. This usually means less lift will be generated on the forward part of the section and more lift towards the aft part. For a more even lift distribution, a greater incidence angle is added to the leading edge of the section [36]. This means that careful choices need to be made for the shape of the root airfoil along with the additional material that will blend this airfoil to the fuselage, which we define as the fairing.

Xu et al. presented a method using B-splines to generate the aerodynamic fairing and then used an adjoint-based RANS method to analyze it [38]. They created a valuable link between CAD geometry and optimization. The main theory of B-splines was discussed earlier in subsection 2.2.1.

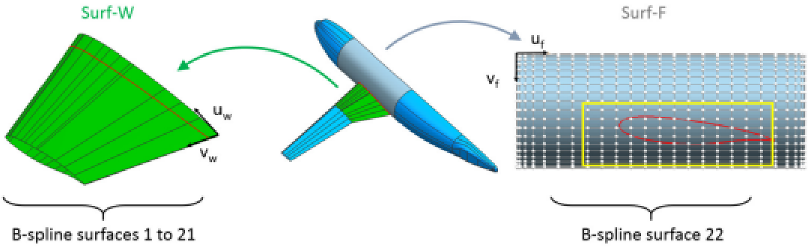

Figure 2.7: B-spline parameterization of a fairing intersecting a fuselage presented by Xu et al. [38]

However, fairing is something that is tailored to the specific aircraft, usually after performing CFD or experimental tests to determine its geometry. The B-spline method proposed by Xu et al. proved to be optimizable, but it required 208 control points [38]. This can be problematic if there is a significant change in design. A goal of this thesis is to parameterize the fairing so that it can be applied to a wider range of designs and provide more functionality, like representing either a fairing or a BWB fuselage. This parameterization will be revealed in subsection 3.2.3. This is a critical aspect in the design of a BWB because the fairing is what envelops the fuselage, making up a large percentage of the aircraft and thus having a significant impact on the overall aerodynamics.

2.1.4 Planform

Many studies have been done on the planform parameterization and optimization of a BWB. It is quite a crucial aspect as this planform dictates the entire aircraft, so it has to account for the required volume of the fuselage as well as the aerodynamics of the wing. This section will also cover the importance of the "kink" region of the aircraft. The work done by Brown et al. showcases some design consideration and selection when confronting the planform. Figure 2.8 shows three different methods on how the planform can be pieced together. In all three cases, they have kept the "kink" at a fixed location. This is defined as the region where the fuselage meets the wing and is usually characterized by a visible change in leading and trailing-edge sweep. This region is significantly important because it defines where the "fuselage" ends and where the "wing" begins.

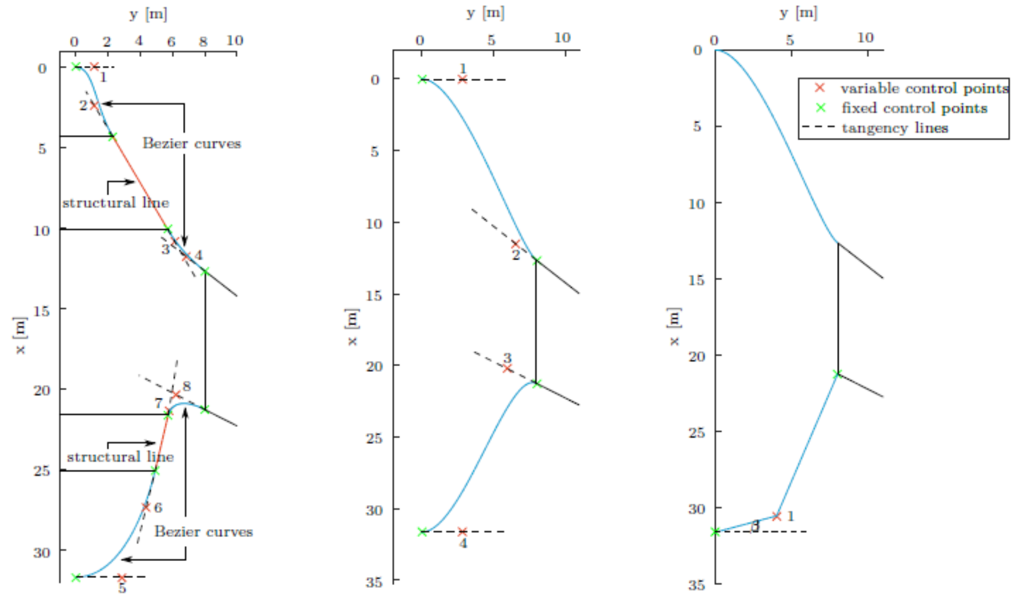

(a) *Structural* LE and *structural* TE type

(b) *Loose* LE and *loose* TE type

(c) *Straight* TE type

Figure 2.8: TU Delft conceptual BWB planform selection [14]

The kink also has a very important effect on the aerodynamic performance of the aircraft. It has the ability to generate a leading-edge vortex [39]. This vortex can greatly benefit the low-speed performance of the aircraft as the vortex can become more pronounced at high angles of attack and can therefore enable the wing to generate more lift. Therefore, for a highly-optimized BWB, it is crucial to design the planform considering the kink. The performance of this kink can vary based on the sweep of the outboard wing, its spanwise location and the fairing used around it. This is something that has not been explored thoroughly in literature and is another important driver for the work presented in this study.

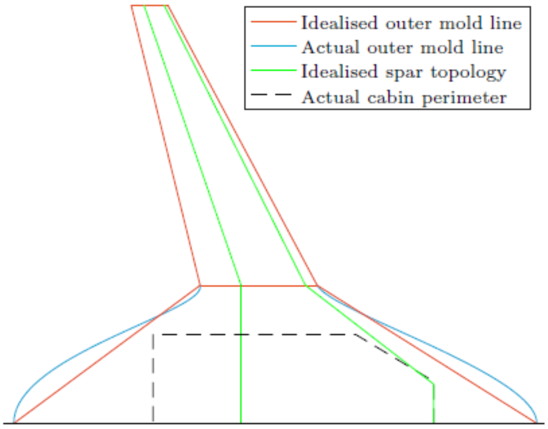

Figure 2.9: TU Delft conceptual BWB optimized planform

Although, Lyu et al. performed an aerodynamic optimization on a BWB and their design achieved a straight leading-edge without a kink [40]. They provided various degrees of freedom, allowing the outer wing sections to have their own sweep, span and chord to be modified by the optimizer. They also stated that their optimized planform was quite close to their baseline shape, which may point to the possibility that the optimizer may have found a local minima/maxima but not the absolute minima/maxima.

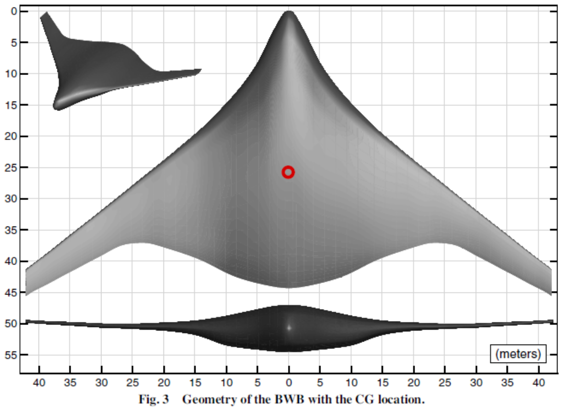

Figure 2.10: Planform of BWB optimized by Lyu et al. showing a straight leading-edge [40]

2.1.5 Internal Volume

The internal volume of a BWB consists of the cabin, cargo bay and fuel tanks. The integration of cargo bays and fuel tanks in Blended Wing Body (BWB) aircraft presents unique challenges due to the unconventional airframe layout and large internal volume requirements, especially when dealing with liquid hydrogen (LH2) as fuel. Even though there are clear potential advantages in using a BWB layout for a hydrogen-powered aircraft[8], this is still an area of research that needs to be carefully analyzed. The current literature reveals substantial advances in optimizing both structural layout and volumetric allocation for fuel and cargo in hydrogen-powered BWB configurations.

Karpuk et al.[41] developed a comprehensive methodology for hydrogen BWB aircraft sizing, introducing critical modifications over kerosene-powered layouts. The aircraft planform is divided into inner, outer, and transitional wing segments, with the hydrogen tank segment represented as an extended inner wing portion. The total planform area is defined as:

$$S_{\text{ref}} = S_{\text{cockpit}} + S_{\text{in}} + S_{\text{out}} \tag{2.1}$$

Karpuk et al. were also able to create some useful equations to size the aircraft depending on the fuel tank size and the number of fuel tanks. This makes it easier to define the geometry of a hydrogen BWB based on the mission parameters. This is important due to the inconvenient shape of hydrogen fuel tanks. Kerosene tanks can be tailored to fit certain sections of the aircraft. but hydrogen tanks have very limited flexibility in terms of shape variation.

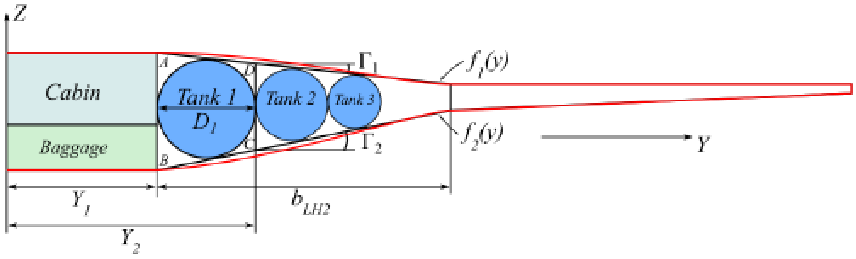

Figure 2.11: Hydrogen BWB front cross-section view [41]

The equation that describes the inscription of the circular tank into the trapezoid structure, shown in Figure 2.11, is given as follows:

$$AB + DC = AD + BC \tag{2.2}$$

To find the trapezoid side lengths, the diameter of the tank and dihedral angles can be used as follows:

$$AD = \frac{D_i}{\cos \Gamma_1} \tag{2.3}$$

$$BC = \frac{D_i}{\cos \Gamma_2} \tag{2.4}$$

Zhu et al.[18] approached the optimization problem from a structural layout perspective. They employed a two-loop strategy: an inner loop to optimize stiffened panel dimensions and an outer loop to determine optimal rib, spar, and stringer placements. Their optimization objective was to minimize structural mass while satisfying constraints on stress, strain, deformation, and buckling factors. Using a finite element model and equivalent panel theory, the optimized layout achieved a 9.28% mass reduction. This study was performed on a kerosene BWB, not a hydrogen one, but the nature of the cargo-hold optimization is still valuable to this research. Adler et al. [42] performed a comparative study on the difference in performance between a hydrogen TAW and hydrogen BWB. Specifically they measured the difference in energy consumption for each configuration when switching to hydrogen. They found that a hydrogen powered BWB consumes 3.1% more energy than its kerosene counterpart, whereas the hydrogen TAW consumed 5.1% more.

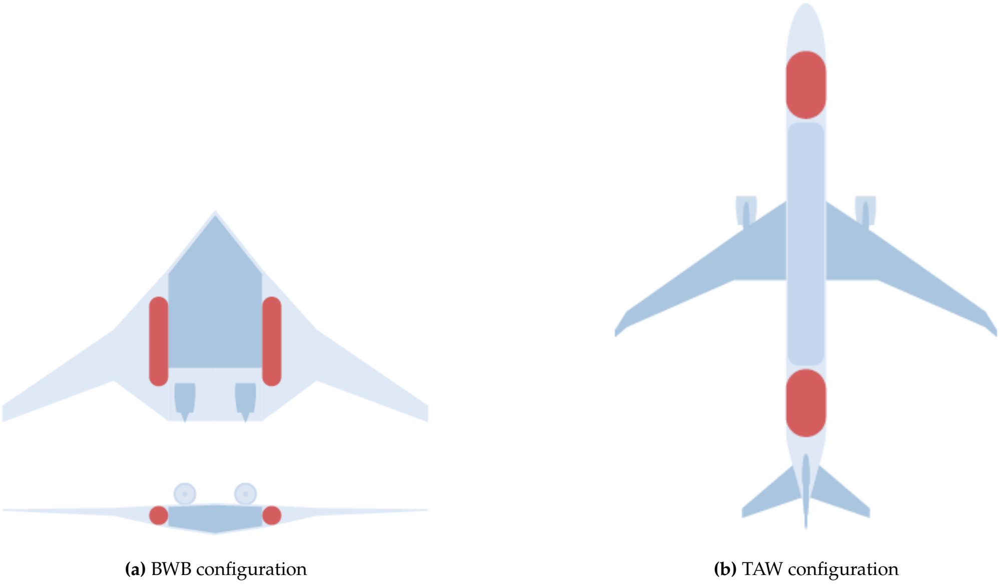

(a) BWB configuration **(b)** TAW configuration

Figure 2.12: Hydrogen tank layouts [42]

2.2 Parameterization Techniques For 2D Geometries

The advent of computer-aided design (CAD) has allowed for faster and more efficient design processes. This means that countless man hours of drawing geometries and by-hand calculations were replaced by software that would greatly reduce errors and effort required. Engineers could now re-direct their focus on making quick and innovative changes rather than restarting a design from the beginning. But, instead of drawing an airfoil by hand, engineers now have to decide *how* to represent an airfoil mathematically for the computer to interpret. The same goes for modeling wings and fuselage. The issue at hand is that there are many different ways to do this, each with their own advantages and disadvantages. There has yet to be one method that is significantly better than the rest. This section will explore the main techniques that are used to describe the cross-sections of aircraft, namely the airfoils and fuselage cross-sections.

2.2.1 Non-Uniform Rational B-Spline: NURBS

The design of aerodynamic shapes, particularly airfoils, requires a parameterization method that balances geometric accuracy, flexibility, and computational efficiency. Among several techniques, the *Non-Uniform Rational B-Splines* (NURBS) representation has emerged as a powerful tool in both traditional and AI-assisted aerodynamic optimization tasks. This chapter reviews the development, mathematical formulation, and recent applications of NURBS in airfoil optimization, particularly in the context of robust and generative design strategies.

NURBS are a generalization of B-splines and Bezier curves that allow for the representation of both analytic and free-form geometries. The parametric curve $\mathbf{C}(u)$ is defined as [43]:

$$\mathbf{C}(u) = \sum_{i=0}^{n} N_{i,p}(u) w_i \mathbf{P}_i, \quad u \in [0,1] \tag{2.5}$$

where $\mathbf{P}_i$ are the control points that define the shape of the curve, w_i are the corresponding weights assigned to each control point, $N_{i,p}(u)$ are the B-spline basis functions of degree p, and u is the parametric variable that defines the position along the curve.

The basis functions $N_{i,p}(u)$ are recursively defined using the Cox-de Boor recursion [43]:

$$N_{i,0}(u) = \begin{cases} 1, & u_i \leq u < u_{i+1} \\ 0, & \text{otherwise} \end{cases} \tag{2.6}$$

$$N_{i,p}(u) = \frac{u - u_i}{u_{i+p} - u_i} N_{i,p-1}(u) + \frac{u_{i+p+1} - u}{u_{i+p+1} - u_{i+1}} N_{i+1,p-1}(u) \tag{2.7}$$

To fit a NURBS curve to sampled points, a least-squares problem is solved:

$$\mathbf{NP} = \mathbf{X} \tag{2.8}$$

where **N** is the matrix of basis functions, **P** is the vector of control points, and **X** is the data.

NURBS have high geometric fidelity with relatively few design variables. They are also generally smooth and continuous across the entire geometry. Compared to other methods like PARSEC or Class-Shape Transformation (CST), NURBS demonstrate superior precision and control, especially for supercritical airfoils where small shape changes can significantly affect performance [31]. In recent research, NURBS were used as the shape representation framework in an evolutionary generative design (EvoGD) system aimed at creating high-performance supercritical airfoils [31]. By representing the airfoil geometry with 16 NURBS control variables, the design process was embedded into a multi-objective optimization framework considering lift-to-drag ratio, thickness, and buffet onset. The authors also showed that NURBS control points have a nearly linear and local influence on the final geometry, which improves model stability and avoids oscillatory behavior.

Another major application of NURBS is in multi-objective robust design, where performance consistency across variable flight conditions is critical. Liang et al. [44] used NURBS to parameterize airfoils for a six-sigma-based robust optimization framework. In this context, the NURBS control points and weights serve as the design variables in a genetic algorithm-based optimization (NSGA-II). Two objectives were optimized; the drag coefficient in transonic cruise conditions, and the lift coefficient in post-stall low-speed regimes. The NURBS-based models achieved representation errors of less than 0.0019 in geometric accuracy and facilitated the identification of Pareto-optimal solutions that balanced performance and robustness.

2.2.2 Parameterized Section: PARSEC

The PARSEC (Parameterized Section) method, developed by Helmut Sobieczky [45], offers a compact and interpretable approach to airfoil geometry definition. It represents the upper and lower surfaces of the airfoil using sixth-order polynomials. Each surface is expressed as:

$$Z_{\text{upper}}(X) = \sum_{n=1}^{6} a_n X^{(n-\frac{1}{2})} \tag{2.9a}$$

$$Z_{\text{lower}}(X) = \sum_{n=1}^{6} b_n X^{(n-\frac{1}{2})}. \tag{2.9b}$$

The coefficients a_n and b_n are uniquely determined by a set of eleven geometric constraints, shown in Figure 2.13. These constraints correspond to physically meaningful quantities, including the leading edge radius, the coordinates and curvatures of the upper and lower crest points, the trailing edge thickness, angle, and direction, as well as the vertical position of the trailing edge itself. This carefully chosen set of parameters ensures that essential aerodynamic features such as curvature, thickness distribution, and trailing edge geometry are directly controllable, while maintaining a smooth and feasible shape [45].

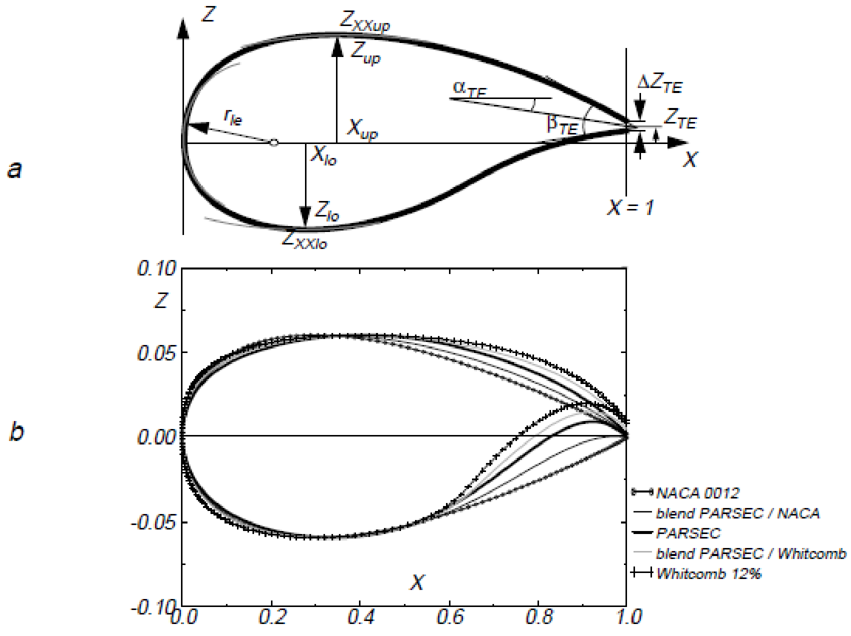

Figure 2.13: PARSEC Airfoil defined by 11 geometric parameters [45]

To enhance its flexibility, the PARSEC formulation also includes the ability to blend its geometry with standard airfoil families such as the NACA 4-digit and Whitcomb supercritical sections. This is achieved through a blending parameter p_{mix}, which continuously interpolates between the PARSEC-generated shape and a reference airfoil as follows:

$$Z_{\text{blend}} = (1 - p_{\text{mix}})Z_{\text{PARSEC}} + p_{\text{mix}}Z_{\text{ref}}, \tag{2.10}$$

where Z_{ref} represents the geometry of the target airfoil used for blending. This mechanism allows the designer to explore a broader space of aerodynamic shapes with minimal adjustments [46].

PARSEC enables fine-tuned surface modifications to meet aerodynamic performance goals, particularly in transonic regimes. For instance, the trailing edge geometry can be refined using a divergent angle parameter, which adjusts the curvature distribution near the trailing edge to reduce pressure losses and improve flow characteristics. Furthermore, local surface bumps can be incorporated into the upper surface geometry to control shock strength and position [45]. The PARSEC formulation also supports multi-component airfoil modeling, including slats and flaps. These are implemented through geometric carving of the base airfoil and described with kinematic parameters that enable combined translation and rotation. In cases involving variable camber or adaptive surfaces, analytic blending functions connect the modified geometry with the baseline shape, enabling smooth and physically realistic deformations during operation. In three-dimensional applications, PARSEC parameters can also be varied along the spanwise direction of a wing. Each parameter becomes a function of span Y, such that the full airfoil surface is expressed as $Z = Z(p(Y), X)$. This feature allows seamless modeling of full wings with continuously changing section shapes, thickness, twist, and camber, all controlled with a relatively small and interpretable set of variables [47].

The PARSEC method provides an elegant and practical approach to airfoil design by embedding aerodynamic and geometric insight into a set of analytic functions. Its ability to capture essential flow-oriented features, support shape blending and refinement, and extend naturally to 3D wing configurations makes it a powerful tool for both conventional and advanced aerodynamic applications.

2.2.3 Design-by-morphing

Design-by-Morphing integrates elements of traditional shape optimization with advanced morphing strategies, enabling smoother and more flexible airfoil transformations [48]. Unlike conventional optimization techniques that rely on a fixed set of shape parameters, DbM constructs airfoil geometries through a combination of baseline shapes, allowing it to be more adaptable. This method reduces the computational burden associated with high-dimensional design spaces while maintaining the ability to achieve high-performance aerodynamic shapes.

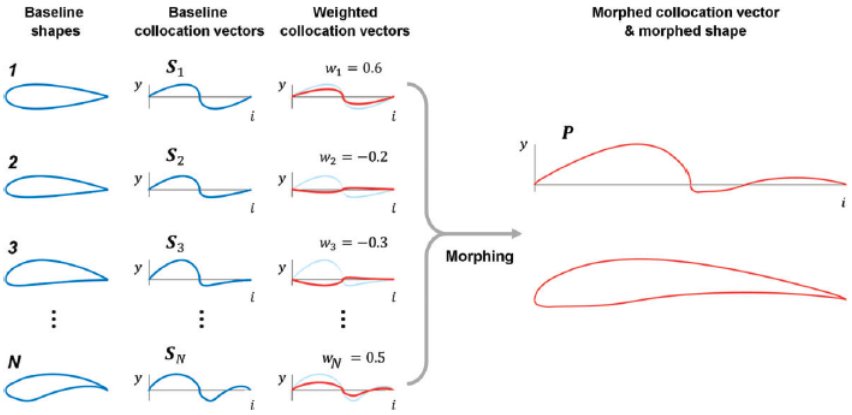

Figure 2.14: Shows the design philosophy of DbM [48]

Airfoil morphing works through the method of multiplying a given airfoil shape by a scalar weight, then the weighted vectors are summed and normalized. For a given number of N baseline shapes, morphing is denoted as[48]:

$$P(x) = \frac{1}{\sum_{m=1}^{N} w_m} \sum_{n=1}^{N} w_n S_n(x) \tag{2.11}$$

where $S_n(x)$ is the y-coordinate collocation vector of the n^{th} baseline shape and w_n is the weighting factor. $P(x)$ is the y-coordinate collocation vector of a morphed airfoil.

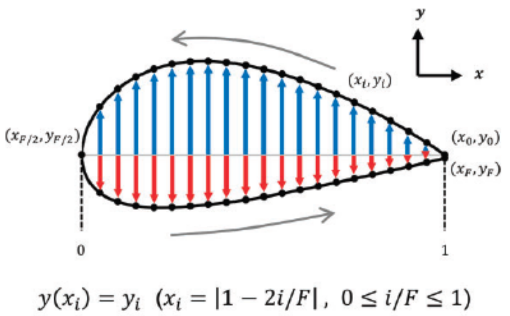

(a) n^{th} airfoil shape

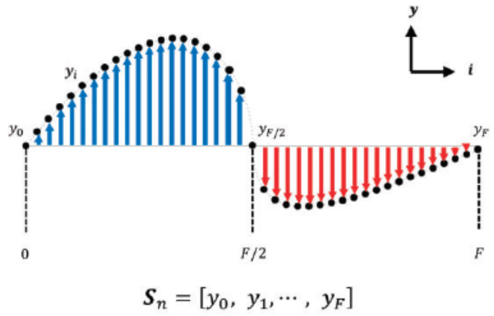

(b) y-coordinate collocation vector

Figure 2.15: Example of the DbM methodology [48]

A key advantage of DbM lies in its capacity to enhance aerodynamic efficiency by refining airfoil contours in a controlled and progressive manner. Studies have demonstrated that morphing-based optimization achieves improved lift-to-drag ratios, delayed stall characteristics, and increased aerodynamic efficiency compared to traditional methods. DbM presents challenges in implementation, particularly concerning computational complexity and model fidelity. Ensuring accurate morphing transformations without introducing unintended aerodynamic penalties requires robust mathematical models and high-resolution simulations.

2.2.4 Class-Shape Transformation Function method

The *Class-Shape Function Transformation* or CST method has become a very popular method to create aerodynamic shapes using a relatively small number of parameters. This method is derived from Bezier curves that are defined with a class and a shape function. The class function defines the type of object that will be generated and the shape function is in charge of modeling the specific features of that object. The simplicity of this representation allows for a more tailored and efficient optimization. This representation has the advantage of directly controlling key airfoil parameters; the leading edge radius, the boat-tail angle and the trailing edge thickness [49].

Kulfan and Bussoletti [50] represented the CST equation as a two-dimensional parameterization which consists of the product of the class function, $C(x/c)$, and the shape function, $S(x/c)$ along with the addition of a term to characterize the trailing edge thickness:

$$\frac{z}{c}(x/c) = C(x/c) \cdot S(x/c) + \frac{x}{c} \cdot \frac{\Delta z}{c} \tag{2.12}$$

The class function defines the "type" of object that is trying to be represented, like a wedge, sears-haack body, elliptical airfoil etc. The class function is defined as

$$C(x/c) = (\frac{x}{c})^{N_1} \cdot [1 - \frac{x}{c}]^{N_2} \text{ for } 0 \leq \frac{x}{c} \leq 1 \tag{2.13}$$

N_1 and N_2 are the defining factors of the class being represented, also ranging from 0 to 1. Figure 2.16 shows how N_1 and N_2 dictate the class of the geometry.

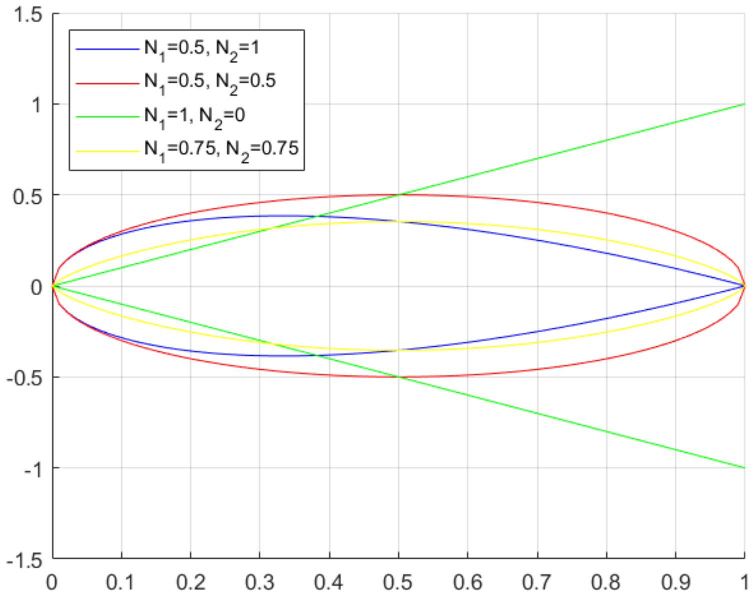

Figure 2.16: Figure showing the effects of varying the N parameters of the class function, $C(x/c)$

Then, once the class is established, the shape function will allow for the further modification of the geometry. The actual geometry parameterization is solely dependent on the shape function, thus it becomes the objective of the design optimization loop [49]. The simplest way to represent the shape function for an airfoil is as follows:

$$S(x/c) = \sum_{i=0}^{n} a_i \cdot K(\frac{x}{c})^i (1 - \frac{x}{c})^{n-i} \tag{2.14}$$

$$K \equiv \frac{n!}{i!(n-i)!} \tag{2.15}$$

Where a_i are commonly known as the Bernstein coefficients or shape factors, K is the binomial coefficient of order n and i is the number of points that will describe the Bezier curve. Any mathematical approximation can be used as the shape function, as long as it is a well behaved analytical function [50].

By modifying the Bernstein coefficients or shape factors, the shape function changes which then modifies the class function. When the shape factors are at unity, the class function is unchanged as shown in Figure 2.17. The summation of all of the Bernstein curves, shown in Figure 2.17b and Figure 2.18b, is what gives the final form of the shape function, that is the upper curve in Figure 2.17a and Figure 2.18a. This shape function is then multiplied by the class function to get the final shape. This is clearly seen in Figure 2.18 through the change of the first shape factor from 1 to 0.5.

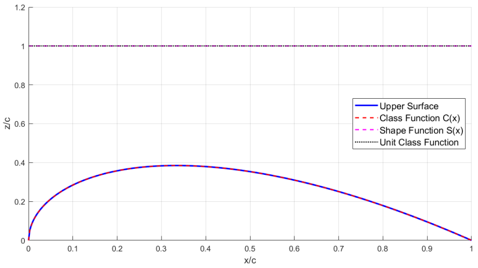

(a) Upper surface CST airfoil and its respective class and shape functions

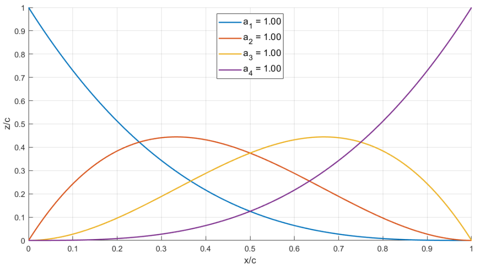

(b) Individual contributions of the shape factors to the shape function

Figure 2.17: CST airfoil with shape factors set to unity

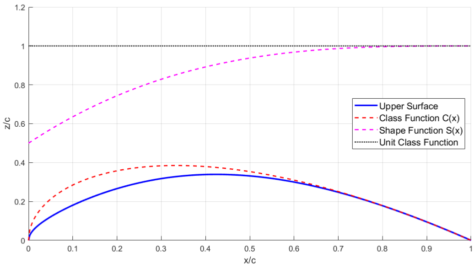

(a) Upper surface CST airfoil and its respective class and shape functions

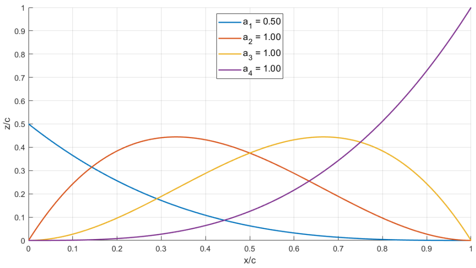

(b) Individual contributions of the shape factors to the shape function

Figure 2.18: CST airfoil with a modification to the first shape factor

The position of the control points is dependent on the number Bernstein coefficients, which are equally spread along the chord of the airfoil, or x/c axis. Selecting an appropriate number and magnitude of these coefficients is crucial to achieving the desired aerodynamic requirements of the airfoil as they will create important features like thickness-to-chord ratio, camber, front-loading, aft-loading etc. This method allows for the creation of almost any type of single-element airfoil. In the following examples, 4 Bernstein coefficients are used for the upper and lower surface. This means that once the class function is defined, only 8 values are needed to create a relatively malleable airfoil.

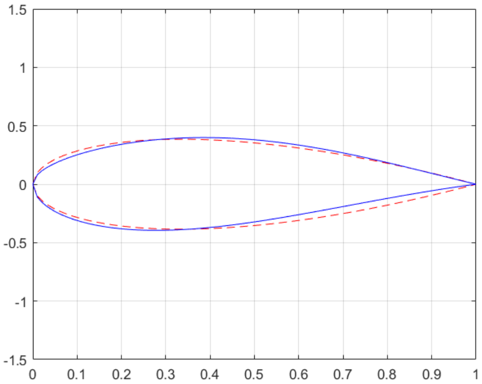

Figure 2.19: Example of a generic cambered airfoil compared to its class function

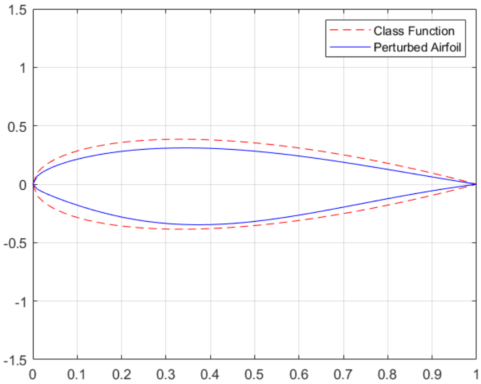

Figure 2.20: Example of a generic front-loaded airfoil compared to its class function

a_u	0.8	1.1	1.2	0.9
a_l	-1.1	-1.1	-0.8	-0.5

Table 2.1: Bernstein coefficients describing the airfoil in Figure 2.19

a_u	0.7	0.9	0.8	0.6
a_l	-0.4	-1.3	-0.8	-0.5

Table 2.2: Bernstein coefficients describing the airfoil in Figure 2.20

Using more values of the Bernstein coefficients can increase the precision, but reduce the convergence rate when performing optimizations, as shown in Figure 2.21. So, it is important to select an adequate number based on the design and optimization goals. For example, a BWB might require more flexibility to create a more complex root section airfoil, as it needs to fit the requirements of a wing and a fuselage.

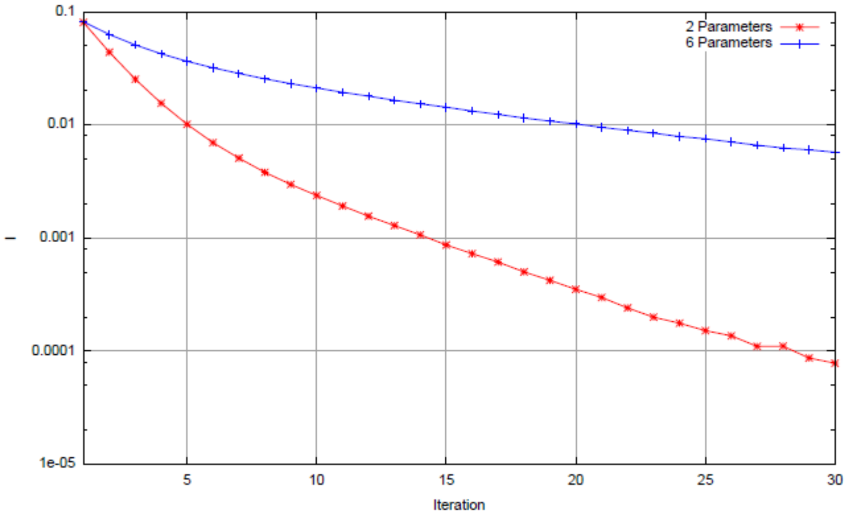

Figure 2.21: Comparison of convergence with a variation in parameters [49]

2.2.5 Hyperellipse

An alternative to elliptical fuselage sections is the use of *hyperellipse* or *superellipse* cross-sections. A hyperellipse provides a smooth, convex geometry that can vary continuously between a rectangle and an ellipse, offering increased design flexibility for internal volume and aerodynamic shaping. It is defined analytically by:

$$\left|\frac{x}{a}\right|^m + \left|\frac{y}{b}\right|^m = 1 \tag{2.16}$$

where a and b are the semi-axes, and m is the shape parameter controlling roundness. For $m = 2$, the shape reduces to a standard ellipse, while higher values produce more rectangular cross-sections with softened corners. This makes hyperellipses particularly useful in aircraft design, as they allow smooth transitions between different fuselage widths and heights while preserving structural and aerodynamic continuity [51].

Whilst methods like CST and NURBS can also be used to represent fuselage cross-sections of all shapes, hyperellipses excel by having a very simple formulation that can define any fuselage cross-section with the use of 3 parameters, something not possible with the other formulations. This capability will be showcased later on in subsection 3.2.4.

2.3 Parameterization Techniques For 3D Geometries

Now that that the parameterization of 2D geometries, specifically for airfoils and cross sections, has been explored, the next step is to review the 3D parameterizations that are commonly used in aerodynamic shape creation and optimization.

2.3.1 3D Class-Shape Transformation

The Class-Shape Transformation (CST) method introduced insubsection 2.2.4 provides an efficient and flexible way to represent airfoil geometries using a combination of a class function and a Bernstein polynomial-based shape function. While CST was originally formulated for two-dimensional sections, its compactness and analytic structure motivated its extension to full three-dimensional wings, where spanwise geometric variation is required.

To construct a CST-based wing, the fundamental idea is to treat each spanwise airfoil as a CST shape and then interpolate the CST parameters smoothly along the span. Olson [52] introduced a formulation that uses CST coefficients as functions of the spanwise coordinate. Instead of defining a full 3D shape at once, individual geometric quantities, such as chord length, thickness-to-chord ratio, or even airfoil coordinates, are expressed as CST-like functions of a normalized spanwise variable η, where $\eta = 0$ corresponds to the root and $\eta = 1$ to the tip.

This spanwise variation is captured by

$$\gamma(\eta) = C_{N_2}^{N_1}(\eta) \sum_{j=0}^{N} a_j b_j^N(\eta) + \eta\gamma_{\text{tip}} + (1-\eta)\gamma_{\text{root}} \tag{2.17}$$

Here, $\gamma(\eta)$ represents a geometric parameter that varies along the span, such as chord, thickness, sweep axis, or even an airfoil coordinate. The Bernstein polynomials $b_j^N(\eta)$ govern the distribution of the shape function whilst a_j serves as a weight to each of the shape functions, the effect of this variable is clearly depicted by the deviation from the class function seen in Figure 2.18a. The class function $C_{N_2}^{N_1}(\eta)$ describes how the parameters are distributed between the root and the tip, like a linear or elliptical distribution for example. The final linear term includes the tip and root values, these serve as the baseline magnitude for the function so that non-zero values can be selected for the root and tip of the geometry. This is introduced because the 2D representation assumes a closed shape. The wing surface is generated by creating a distribution of airfoils with all of its parameters defined by the 3D CST formulation. This includes the airfoil points, chord, thickness-to-chord ratio, dihedral, sweep etc. This means that inputting the spanwise location into the equations will return the points of the airfoil (including the twist, dihedral etc), given the chosen shape factors[52]. The entire wing can then be described in 3D points by repeating this for all of the spanwise stations, becoming more refined if the number of spanwise stations is increased. However, wings with sudden planform changes—such as box wings, kinked wings, or blended winglets—cannot be represented by a single continuous CST spanwise function. This means that a piecewise continuous formulation is required to represent these shapes[52].

2.3.2 NURBS-Based Wing Parameterization

As discussed in subsection 2.2.1, Non-Uniform Rational B-Splines (NURBS) offer a compact and mathematically robust means of representing aerodynamic geometries. Their extension from airfoils to full three-dimensional wings is natural next-step, as NURBS surfaces preserve the same advantages. Compared with polynomial or purely algebraic surface definitions, NURBS enable the construction of wings whose shape can be controlled precisely while remaining inherently smooth across both chordwise and spanwise directions [53].

A NURBS wing surface is defined by a set of weighted control points summed along the spanwise and chord directions through rational B-spline basis functions. The surface representation takes the form

$$\mathbf{S}(u,v) = \frac{\sum_{i,j} N_i(u)\, M_j(v)\, w_{ij}\, \mathbf{P}_{ij}}{\sum_{i,j} N_i(u)\, M_j(v)\, w_{ij}}, \tag{2.18}$$

in which the parameters u and v define the chordwise and spanwise directions, respectively. The control points $\mathbf{P}_{ij}$ and their weights w_{ij} determine the geometric behavior, while $N_i(u)$ and $M_j(v)$ are the B-spline basis functions that ensure continuity [54]. An important consequence of this formulation is that moving a single control point only influences a localized portion of the surface. This allows aerodynamic shape changes to be introduced with fine control while maintaining a well-behaved global geometry. Wing construction using NURBS typically begins with the definition of airfoil profiles at several spanwise stations, such as the root, kink, and tip. These profiles preserve key aerodynamic characteristics while reducing the size of the design space [53]. Interpolating these profiles using NURBS lofting then produces a complete surface that varies smoothly along the span. A clear strength of the NURBS framework is that it gives the designer control over the type of lofting required, whether its a straight, "ruled" loft or a higher-degree "curved" loft [53]. This is done through the selection of the quantity and location of the control points.

The NURBS formulation is critically important to 3D modelling because most lofting in CAD softwares is done using NURBS [55]. This allows for the creation of 3D surfaces using any of the 2D methods outlined above in section 2.2. This is why NURBS is seen in so many applications [55].

2.3.3 Free-Form Deformation for 3D Wing Optimization

Free-Form Deformation (FFD) provides a means of deforming that geometry using a deformation field over a given shape, which is defined as a lattice of points [56]. In this approach, the wing and its surrounding mesh are enclosed within a deformable lattice. As the lattice is perturbed, the enclosed geometry is updated accordingly. One of the principal advantages of this method is that the mesh connectivity remains fixed, allowing for smooth shape modification without the need for the geometric generation of surface or volume meshes [57]. This method provides direct control over the mesh of an object, making it particularly useful for CFD and optimization routines.

The position of a point inside the lattice is expressed using a trivariate blending of basis functions. The deformation field is written as

$$\Delta\mathbf{q} = \sum_{i,j,k} B_i(\xi)\, B_j(\eta)\, B_k(\zeta)\, \Delta\mathbf{P}_{ijk}, \tag{2.19}$$

where (ξ, η, ζ) are the local coordinates within the reference lattice, B_i are Bernstein or B-spline basis functions, and $\Delta\mathbf{P}_{ijk}$ are the control point displacements that form the design variables. The new geometry is obtained by adding this displacement to the original point location. Because the deformation acts directly on the mesh, the designer has more control of the exact geometry that is used in an aerodynamic solver. This makes FFD well suited to aerodynamic optimizations because it allows smooth shape variations to be introduced with a relatively small number of parameters, given a baseline shape has already been defined [57]. FFD and NURBS are frequently employed together, with NURBS providing an exact, constraint-preserving representation of the baseline geometry, and FFD enabling flexible mesh deformation during optimization. This method allows for improvements in computational efficiency, and ensures that optimized geometries remain feasible. However, it still needs a baseline shape to work from, which is usually created using other methods, like NURBS [57].

2.4 Review of Parameterization Methods

Several parameterization techniques have been developed for defining 2D aerodynamic geometries, each with distinct advantages and limitations. Non-Uniform Rational B-Splines (NURBS) offer excellent geometric fidelity and local control through weighted control points. Their mathematical smoothness and CAD compatibility make them highly attractive, but they typically require more parameters, and the control points lack direct aerodynamic meaning [44]. PARSEC, on the other hand, offers a compact and physically interpretable set of variables that directly represent aerodynamic features such as leading edge radius and crest curvature. This allows designers to prescribe meaningful geometry changes, but the polynomial framework is less flexible for highly nonstandard shapes [45]. Design-by-Morphing enables smooth transitions between baseline shapes while reducing dimensionality, yet its performance depends heavily on the chosen basis set and does not offer direct control over geometric features [48].

At the opposite end of the spectrum, data-driven approaches such as GAN-based models can generate novel shapes from learned latent spaces, but require large datasets and lack interpretability.

Among these methods, the Class-Shape Transformation (CST) approach provides an effective compromise. It defines the shape analytically through a combination of a class function and a Bernstein polynomial-based shape function, allowing control of thickness, camber, leading-edge behavior, and trailing-edge geometry. CST achieves this with relatively few parameters and remains computationally efficient, making it particularly well suited for automated optimization workflows [49, 50]. The main limitation with 2D CST arises when trying to make changes to an airfoil shape through the shape factors. As the thickness-to-chord is not an input, it can completely change the aerodynamics of that airfoil. The maximum thickness-to-chord can be extracted from 2D CST but cannot be input. This means that modelling existing airfoils requires an extra step to check this thickness-to-chord ratio. The hyperellipse also proved to be the simplest method to generate a plethora of 2D fuselage cross-sections and will thus be the preffered choice when doing so.

Extending 2D methods into 3D requires additional structure to handle the spanwise variation and surface smoothness. NURBS surfaces generalize the 2D spline concept into a fully parametric 3D lofted geometry. Their ability to produce smooth, curvature-continuous wing surfaces makes them highly compatible with CAD and structural modeling. However, they offer limited direct aerodynamic interpretation, and controlling aerodynamic twist, sweep, or thickness requires indirect manipulation of the control lattice [54]. FFD operates on an enclosing lattice rather than the geometry itself. It is well suited for optimization because it directly modifies the CFD mesh without remeshing. However, FFD requires a predefined baseline shape and does not inherently include aerodynamic parameters [57]. It is best used as a deformation tool rather than a primary shape generator. 3D CST, as described in [52], extends the CST framework by turning each geometric airfoil parameter into a function of span. Thickness, twist, chord, camber, and sweep can all be defined by the same compact function set. This maintains the low parameter count and aerodynamic interpretability of CST, while allowing continuous control across the span. 3D CST extends this capability to wings that have significant spanwise variation, making it especially suitable for BWB. For a BWB, the wing, fairing, and fuselage must merge seamlessly whilst having a large variation in shape, the smoothness and direct control over wing parameters with a low number of parameters makes CST the most attractive option. The downside to the smoothness of CST is that it struggles with directly modelling section breaks, so a piecewise derivation is needed for this. Using a piecewise 3D CST for the fairing surface definition and NURBS-based lofting can mitigate these issues and presents itself as a powerful and flexible modeling strategy, which is why it will be further explored in the coming chapters.

Chapter 3

Methodology

This chapter contains the main concepts and principles behind the development of the model. It will explain how the hybridization factor was implemented into a CST parameterization and how that was applied to create 3D aircraft models. The modelling of other parts of the aircraft like the fuselage nose, tail and landing gear will also be described, as these have to be adapted to the new parameterization. This section will also touch on the type of CFD software that was used and its working principles.

3.1 Introduction to methods

The basic idea of aircraft design generally consists of outlining a set of top-level aircraft requirements (TLAR) and then creating a geometry that successfully meets those requirements. However, many aspects of the aircraft's geometry are still calculated by hand in the conceptual design stage. At the conceptual stage, the aircraft is designed only considering its top-level aircraft requirements (TLAR) [58], which is done through the help of sizing methods, critical thinking and general aircraft know-how. This provides the general expectations of an aircraft, allowing for a rough yet viable design to be created. With the help of modern tools like ParaPy and Flightstream, some of the early-stage analyses and calculations can be integrated into a singular program and automated so the designer can get a rough idea on the performance of a design and perform multiple iterations in a shorter time-frame. This opens up the opportunity for the implementation of multi-disciplinary optimizations. To do this, one must have a numerical model that is described as simply as possible. The use of CST in airfoil and wing optimizations has proven to be a robust and efficient method to do this, without the need of very high-order shape functions [49][59]. Being able to integrate a flexible aircraft model with a CFD solver can greatly reduce time and computational effort. This is possible at the expense of the CFD solver's level of fidelity. Flightstream is regarded as a mid-fidelity solver as it is a panel method that has certain viscous effects integrated, like boundary layer modelling. As the model needs to be flexible, the meshing routine also needs to flexible. Making hand-tailored meshes for each configuration is therefore not possible, which is why using a low or mid-fidelity solver is suitable for this design task.

The overarching goal of this work is to find a novel and practical way to design aircraft such that it can account for both conventional and unconventional aircraft through the use of a new parameter, the hybridization factor. This will not only reduce the amount of inputs required to design aircraft, but it will also present a new way to link the aerodynamic shape of an aircraft to its performance.

The ability to create a wide number of models with large variations in parameters is made relatively easy thanks to ParaPy's geometry library and lazy-evaluation. ParaPy was created to make knowledge-based engineering platforms easier to use and manage. ParaPy is based on object-oriented programming (OOP) which allows data and behaviours to be stored within objects. The data is stored as an "attribute" to the object, which can either describe physical characteristics of the object based on inputs, or contain functions that calculate certain behaviours of the object. Within a ParaPy class, it will usually consist of attributes and parts. Parts are the physical geometry that is output into the graphical user interface

(GUI). Parts can be a directly shown, ie. a box, or they serve as an intermediate geometry for another part, like the profiles of a loft. Lazy-evaluation is when a value or creation of an object is not computed unless there is an actual need for it, opposed to the classical programming where everything is re-evaluated when a program is re-run. This comes in handy for object-oriented programming because it greatly saves memory, allowing for the efficient creation and modification of complex geometries ParaPy allows users to define components or systems as classes, with parts and attributes that can define sub-components and desired behaviours. These sub-components are denoted as children of the class. For example, a Wing class might contain Spar and Rib objects as children, and updating an input in the Wing automatically recalculates all dependent parts. Generic elements like airfoils, fuselage and landing gear can be reused across projects, and new classes can inherit from base components without rewriting code. OOP also makes complex systems easier to organize and maintain, as each part of a model is encapsulated, and changes in one component propagate naturally to others. Using OOP in ParaPy allows engineers to build modular, parametric, and maintainable CAD models efficiently, making it particularly suited for designing complex systems. Although there is a significant learning curve before a designer can get to the same level of proficiency as they would be with commercial CAD software, once this knowledge is established making a hand-tailored, parametric and analysis-integrated model becomes very manageable. The main idea motivating the development of the ParaPy platform is to reduce the repetitive work that comes with engineering, so that more time can be devoted to the creativity and innovation.

3.2 Modelling

This section outlines the main methods and equations that were chosen to model the aircraft. It begins with the mathematical definition of the hybridization factor and then moves on to the aircraft components.

3.2.1 Hybridization Factor

The hybridization factor, denoted as χ, serves as the main innovation of this parametric approach. It quantifies the semi-spanwise extent of the blended fuselage-wing region, or fairing, relative to the total semi-span. An aircraft with $\chi \approx 0$ can represent a conventional tube-and-wing configuration with no significant fairing beyond the fuselage junction. As χ increases, the blended region extends further outboard, gradually increasing the span and size of the fairing. The fuselage width increases and its height decreases. Around $\chi \approx 0.3$, the aircraft approaches a BWB configuration. When χ approaches unity, the aircraft's wing becomes a fully enveloped within the fairing. With the right parameters, this represents a fully blended wing body with no distinct separation between fuselage and wing. This parametric definition offers several key advantages:

1. Design Space Exploration: Rather than designing conventional and BWB aircraft with fundamentally different tools and methodologies, designers can now explore the broad spectrum between these configurations.
2. Comparative Analysis: This parameter enables a direct analysis and insight into how different hybridization levels affect aerodynamic performance, structural requirements, and operational characteristics.
3. Optimization Flexibility: By treating the degree of "blending" as a design variable rather than a discrete choice, it opens up new possibilities for optimization algorithms to identify configurations that best balance competing objectives such as efficiency, stability, and internal volume.

The introduction of the hybridization factor thus represents a fundamental shift in how the design space is analyzed for transport and cargo aircraft. Rather than viewing conventional and BWB configurations as completely separate ideas, this approach treats them as part of a gradual scale instead of distinct categories, opening new possibilities for innovation in aircraft design.

To begin mathematically defining the hybridization factor, the manner in which a wing can morph into the fuselage needs to be explored. To do this, the spanwise coordinate system of the wing needs to be adjusted. Typically, the position along a wing is defined using the non-dimensional spanwise location, η, but now this needs to be able to distinguish between fairing, fuselage and wing. For the purpose of this project, the fairing is defined simply as an increase in size or volume of the inboard wing, not limited to the wing-body juncture. Therefore, the fairing will be the conduit for this process.

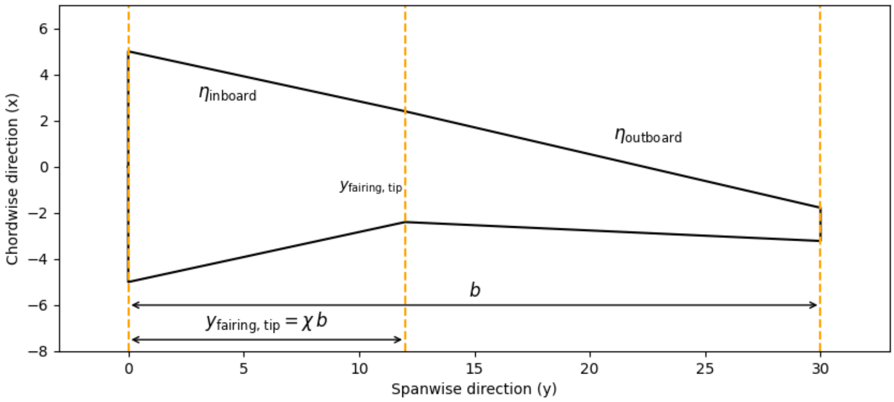

Figure 3.1: Planform showing initial parameterization

To do so, the classical definition of the non-dimensional spanwise location will be divided into two sections, the "fairing" and the wing section. When looking at a BWB the "fairing" is essentially the region where the cabin would be, thus it can be described as the fuselage or center-body. The "kink" region, usually marked by a sharp change in angle at either the leading or trailing edge of the wing, is a key element in defining the transition point between the fuselage and wing of a BWB. But this parameterization is not limited to a BWB, as many conventional aircraft also have a kink region, as they usually have a larger inboard wing section to accommodate the landing gear. This opens up the possibility to model the wing of a BWB and a conventional aircraft using the same parameters.

$$y_{\text{fairing ,tip}} = b_{\text{fairing}} = \chi \cdot b \tag{3.1}$$

$$\eta_{\text{inb}} = \frac{y}{b_{\text{fairing}}} = \frac{\eta \cdot b}{\chi \cdot b} = \frac{\eta}{\chi} \tag{3.2}$$

$$\eta_{\text{out}} = \frac{y - y_{\text{fairing, tip}}}{b - b_{\text{fairing}}} = \frac{y - y_{\text{fairing, tip}}}{b - \chi \cdot b} = \frac{\eta \cdot b - \chi \cdot b}{b \cdot (1 - \chi)} = \frac{\eta - \chi}{1 - \chi} \tag{3.3}$$

where χ is the hybridization factor, b is the half-span and η is the non-dimensional spanwise position. Now that the wing has been parameterized into two sections, inboard and outboard or fairing and wing, this can now be substituted into the CST Wing equations that were described earlier in subsection 2.3.1, using piece-wise methodology. These equations will be described in subsection 3.2.3.

Before proceeding with the modelling, it is necessary to clarify which geometric inputs are directly governed by the hybridization factor, since χ controls the degree to which the fuselage is integrated into the wing. As the aircraft transitions from a conventional layout toward a fully blended configuration, several center-body and fairing-related parameters must deform accordingly to maintain a coherent outer mold line. These parameters therefore depend explicitly on χ. In contrast, planform-level wing parameters such as sweep, taper, and dihedral are intentionally kept independent of the hybridization factor, ensuring that the effects of χ and the shape factors on the geometry can be isolated and compared more directly.

Table 3.1: Dependency of main geometric parameters on the hybridization factor χ.

χ-dependent parameters	**χ-independent parameters**
Fairing thickness distribution	Wing sweep angle Λ
Fairing chord distribution	Taper ratio, λ
Fairing positioning	Dihedral angle Γ
Fairing incidence distribution	Shape factors, a
Fairing curvature	Center and outboard wing airfoils
Fairing volume	
Fuselage height and width	
Total wing area	

3.2.2 Airfoil design

The creation of airfoils is also done using the CST method, as it is an intuitive method that provides great flexibility with a modest number of inputs [50]. Once the CST formulation is established within a code, only 8 values are needed; 4 upper and 4 lower to have a well-defined airfoil. More values allow for a more precise representation, but 8 values is enough to create transonic or supercritical airfoils, the more commonly used ones in the industry. Another important advantage of using a CST airfoil is that it is always mathematically smooth, meaning it is continuous and differentiable everywhere, even at the trailing edge. This is particularly useful when it comes to 3D modelling and optimization because it can provide smooth surfaces with a low computational effort. As it is a polynomial-based method with a low number of design variables, it also makes it well-suited for gradient-based optimization. The low number of design variables also greatly reduces the design space which in turn produces faster convergence rates. Designers can greatly benefit from using CST airfoils on complex wing designs. For example, if there are two different airfoils defining a section and a section is needed in between them, then only their shape values need to be interpolated to get the fully defined airfoil at that section, greatly saving time and computational cost.

The formulation of the CST airfoil is primarily based on the paper presented by Kulfan and Bussoletti [50], which is described in detail in subsection 2.2.4. The coordinates of the airfoil are defined as follows

$$\frac{z_U}{c}(\psi) = t_c\, C(\psi)\, S_U(\psi), \quad \frac{z_L}{c}(\psi) = t_c\, C(\psi)\, S_L(\psi) \tag{3.4}$$

where C is the class function, S_U and S_L are the shape functions defined by the shape factors, a, for the upper and lower surfaces, respectively. ψ is the non-dimensional chordwise coordinate defined as $\psi = x/c$. Additionally, a thickness value t_c is multiplied to scale the chord thickness. This thickness will be defined using the hybridization factor, explained later on in this chapter.

To be able to have a fully defined airfoil, twist and translational position also needs to be applied. This is done as follows:

$$\begin{bmatrix} x' \\ z' \end{bmatrix} = \begin{bmatrix} \cos\theta & \sin\theta \\ -\sin\theta & \cos\theta \end{bmatrix} \begin{bmatrix} x \\ z \end{bmatrix}, \qquad \theta = \text{twist} \tag{3.5}$$

$$x_U(\psi) = x(\psi)\cos\theta + z_U(\psi)\sin\theta, \quad z_U(\psi) = -x(\psi)\sin\theta + z_U(\psi)\cos\theta \tag{3.6}$$

$$x_L(\psi) = x(\psi)\cos\theta + z_L(\psi)\sin\theta, \quad z_L(\psi) = -x(\psi)\sin\theta + z_L(\psi)\cos\theta \tag{3.7}$$

$$\mathbf{P}_U(\psi) = \Big(x_U(\psi) + x_0, \;\; y_0, \;\; z_U(\psi) + z_0\Big) \tag{3.8}$$

$$\mathbf{P}_L(\psi) = \Big(x_L(\psi) + x_0,\ \ y_0,\ \ z_L(\psi) + z_0\Big) \tag{3.9}$$

where θ is the twist or rotation angle of the airfoil and x_0, y_0 and z_0 are the translational factors, all of which will be a defined with the CST distribution described in the next chapter. This formulation was created into the AirfoilCurve class, shown in Appendix B, so that it can be easily called whenever needed. This greatly improves the coding efficiency as translation, rotation and quantification can all be done by calling the class, highlighting one of the practicalities of using ParaPy for object-oriented programming.

3.2.3 Wing design

The design of the wing is based on the 3-D CST wing formulation outlined in subsection 2.3.1 with the inclusion of the hybridization factor. This defines the chord, thickness, incidence angle, streamwise position and z-position, allowing for an endless variety of wing shapes and sizes with a moderate amount of inputs. The goal is to use this CST formulation to modify the fairing section of the wing, which is now defined as being inboard of the hybridization factor, denoted as $0 \leq \eta \leq \chi$. The outboard section, $\chi < \eta \leq 1$, simply represents a straight wing based on the the wing parameters at the χ and tip location. Based on this, the chord, incidence and thickness-to-chord distribution were derived as follows:

$$c(\eta) = \begin{cases} C_{N_2}^{N_1} \displaystyle\sum_{j=0}^{N_c} a_{c,j} \binom{N_c}{j} \left(\frac{\eta}{\chi}\right)^{j} \left(1 - \frac{\eta}{\chi}\right)^{N_c - j} + \left(1 - \frac{\eta}{\chi}\right) c_{\text{root}} + \frac{\eta}{\chi} c_{\text{tip}}, & 0 \leq \eta \leq \chi \\ \left(1 - \dfrac{\eta - \chi}{1 - \chi}\right) c(\chi) + \dfrac{\eta - \chi}{1 - \chi} c_{\text{tip}}, & \chi < \eta \leq 1 \end{cases} \tag{3.10}$$

$$i(\eta) = \begin{cases} C_{N_2}^{N_1} \displaystyle\sum_{j=0}^{N_i} a_{i,j} \binom{N_i}{j} \left(\frac{\eta}{\chi}\right)^{j} \left(1 - \frac{\eta}{\chi}\right)^{N_i - j} + \left(1 - \frac{\eta}{\chi}\right) i_{\text{root}} + \frac{\eta}{\chi} i_{\text{tip}}, & 0 \leq \eta \leq \chi \\ \left(1 - \dfrac{\eta - \chi}{1 - \chi}\right) i(\chi) + \dfrac{\eta - \chi}{1 - \chi} i_{\text{tip}}, & \chi < \eta \leq 1 \end{cases} \tag{3.11}$$

$$t_c(\eta) = \begin{cases} C_{N_2}^{N_1} \displaystyle\sum_{j=0}^{N_t} a_{t,j} \binom{N_t}{j} \left(\frac{\eta}{\chi}\right)^{j} \left(1 - \frac{\eta}{\chi}\right)^{N_t - j} + \left(1 - \frac{\eta}{\chi}\right) t_{c,\text{root}} + \frac{\eta}{\chi} t_{c,\text{tip}}, & 0 \leq \eta \leq \chi \\ \left(1 - \dfrac{\eta - \chi}{1 - \chi}\right) t_c(\chi) + \dfrac{\eta - \chi}{1 - \chi} t_{c,\text{tip}}, & \chi < \eta \leq 1 \end{cases} \tag{3.12}$$

The x and z coordinates are also modelled in the same fashion, but instead of having direct x and y values for the root and tip inputs, these values are derived from the sweep and dihedral to make it more intuitive for the designer. The y coordinate distribution does not need to be included in this way because the it is defined by the hybridization factor, χ. In other words, the spanwise location of the selected airfoil profiles is dependent on the hybridization factor, this is explained in section 3.4. Although these equations are seemingly quite cumbersome, once established, they only need 4 inputs to work. The shape factors, the Bernstein order coefficients and the values at the root and tip of of the wing or section. Most of these inputs also remain constant, the shape factors and root and tip values are the main ones that are modified. The rest of the inputs are just dependent on the spanwise position and hybridization factor. This allows the for the complete description of these parameters along the entire wing, with very few inputs. The shape factors control the geometry of the fairing, with respect to the inputs at the root and tip. For the unhybridized wing, when $\chi = 0$, these equations return a simple straight wing lofted from root to tip. An important goal of this parameterization is to be able to scale the root and tip values and get the same wing shape if the shape coefficients stay constant. For example, if the root and tip chord are increased, it will not just increase the chord at these sections, but it will output the same distribution, just scaled by the increase in chord. As each wing parameter (airfoil, chord, incidence, thickness, fairing curvature) is governed by independent CST coefficients and only linked together by the hybridization factor, the framework does not rely on any fixed planform assumptions. As a result, this formulation can take a conventional model and morph it a hybrid or fully blended configuration simply by altering a few parameters. This flexibility is a fundamental difference from previous BWB modelling approaches, which generally require specific planforms and geometric constraints.

Figure 3.2 and Figure 3.3 show how the theory from the 2D CST section is also applied to the 3D geometry. In Figure 3.2a, the contributions of each shape factor are shown, the summation of them being the blue line in the subsequent figure Figure 3.2b. This z-distribution can be visualized through the trailing edge of the fairing section shown in Figure 3.2c.

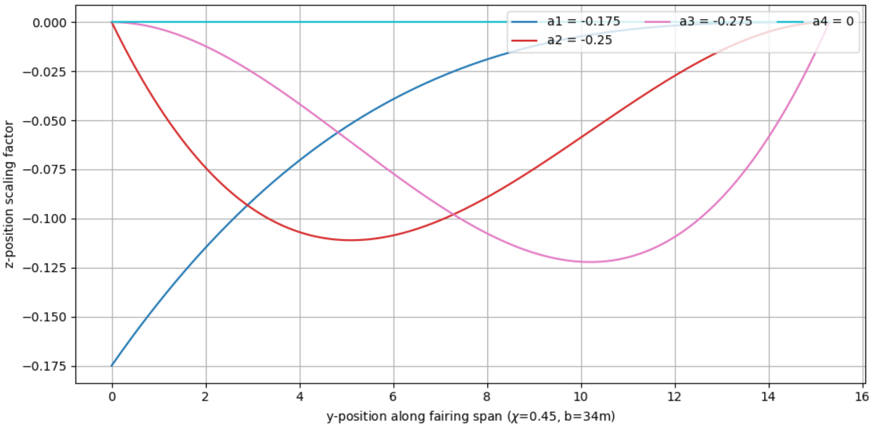

(a) Bernstein polynomial contributions to the CST z-position shape factor.

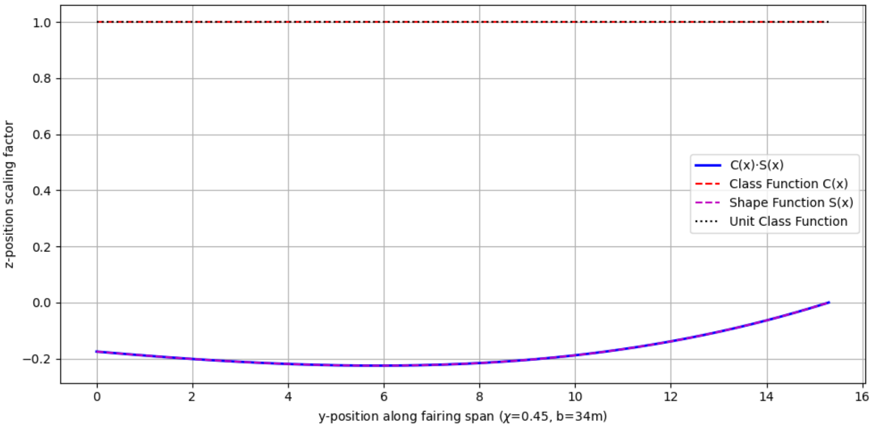

(b) Resulting CST chord scaling factor $C(\eta)S(\eta)$ with class and shape functions.

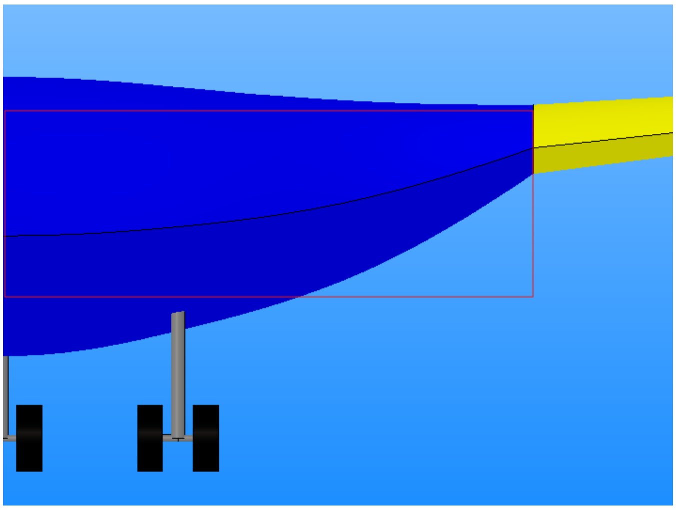

(c) Resulting wing–fairing planform region showing applied z-position distribution.

Figure 3.2: Spanwise effect of z-position shape factors

The same behaviour can be seen with the CST chord distribution, in Figure 3.3c. However the top-view of the trailing edge curvature does not exactly match the curve shown in Figure 3.3b. This is due to two reasons. The first being the fact that the root chord is an input to the geometry and is chosen to be fixed, so the scaling factor is 0 at this position. The other reason is that the top planform is influenced by another distribution, which is the x-positioning CST factors. For a given span and taper ratio, the top-view leading edge and trailing edge curvature is controlled solely by the chord and x-position shape factors. This same coupling occurs with the thickness-to-chord and z-positioning distribution on the front-view curvature of the fairing.

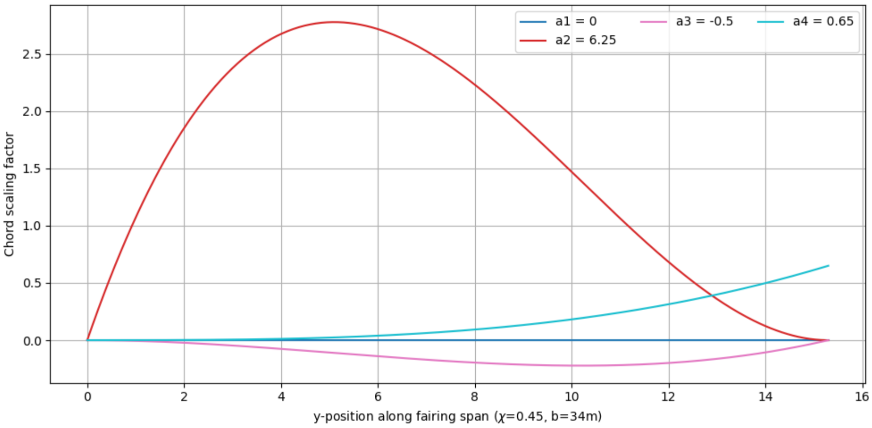

(a) Bernstein polynomial contributions to the CST chord shape factor.

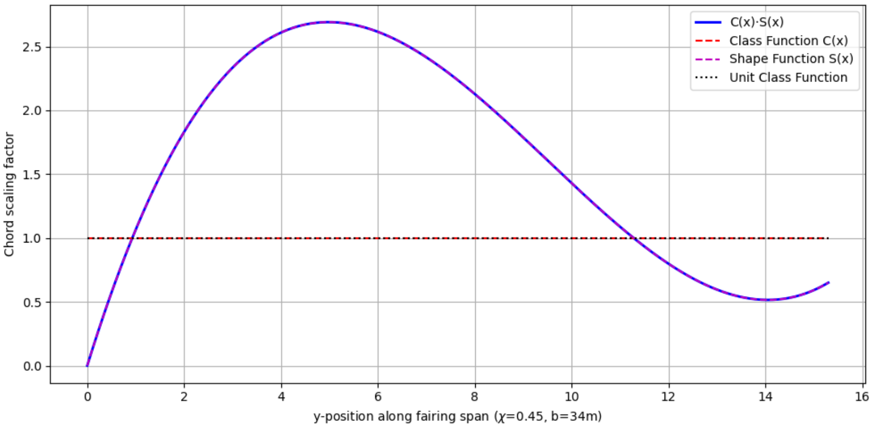

(b) Resulting CST chord scaling factor $C(\eta)S(\eta)$ with class and shape functions.

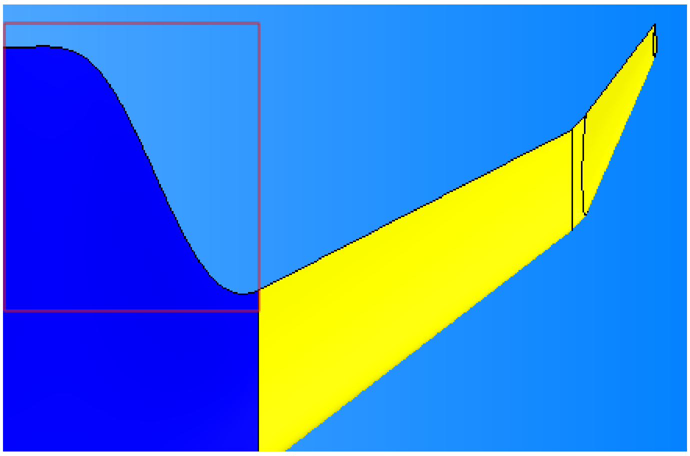

(c) Resulting wing–fairing planform region showing applied chord distribution.

Figure 3.3: Spanwise effect of chord shape factors

This then leads to the discussion of how the distribution of parameters are distributed smoothly along the fairing. As they are derived from the CST formulation, they are controlled by the shape function. This is shown in the equation above as,

$$S(\eta) = \sum_{j=0}^{N_i} a_j \binom{N}{j} \left(\frac{\eta}{\chi}\right)^j \left(1 - \frac{\eta}{\chi}\right)^{N-j}, \qquad 0 \leq \eta \leq \chi \tag{3.13}$$

The distribution along the span or chord-wise direction will always be of the order N, controlled by a number of $N + 1$ shape coefficients. This in turn ensures that the these parameters vary smoothly between one another. In practice, this is seen when there is a change in the a coefficients, as changing one of them affects the distribution of the whole wing, not just at a specific location. This means that for a single-section wing, as shown in Equation 2.17, the wing is geometrically continuous for all of its derivatives, C_0, C_1 and C_2 [52]. Now that more than 1 section is introduced, the equation is represented as a piecewise, as shown in Equation 3.10, Equation 3.11 and Equation 3.12. As this introduces a section break in the wing, it is no longer continuous by nature, thus a linear interpolation is needed to ensure that the transition between fairing and wing, at $\eta = \chi$, is at least continuous in the first order, C_0. This is done automatically by introducing the previously derived factors, η_{inb} and η_{out}, along with their respective bounds, $0 \leq \eta \leq \chi$ and $\chi < \eta \leq 1$.

When a function is "smooth" it is likely also denoted as being continuous, thus it is important to understand how this is quantified. C_0 indicates *zero-order* continuity, which means the function is continuous at that point, there are no gaps or jumps. *first-order* continuity or C_1 means that the first derivative is constant across a given point and lastly C_2 represents *second-order* continuity, so the second derivative is equal across a given point.

With the model at hand, 6 span-wise locations are selected to control the wing shape. This number of locations was selected after successfully modelling a handful of TAW and BWB aircraft, thus it was deemed sufficient for this level of analysis. The designer can easily add or remove airfoil sections by creating another instance of the AirfoilCurve class and inputting their respective spanwise-dependent parameters. It is important to note that Equation 3.10, Equation 3.11 and Equation 3.12 describe a wing with 2 sections or 3 airfoil profiles, at the location of the root, kink and tip. But to get a more refined fairing or BWB fuselage, one may need to add more sections to get their desired shape. Thus, more linear interpolations can be added to these equations to define more profiles, as long as they are still χ dependent. Then, a BSpline lofting procedure using ParaPy's LoftedSolid is carried out. This allows the type of continuity to be selected or it can also do a ruled loft, which follows each curve exactly. The option to do so is provided as an input in the application. This gives the designer a great deal of flexibility as they can decide whether they want a smooth transition or a kink at a profile location. This is an important feature of this application, because directly enforcing C_1 and C_2 continuity constraints between all the sections would significantly hinder the range of wings that can be modelled.

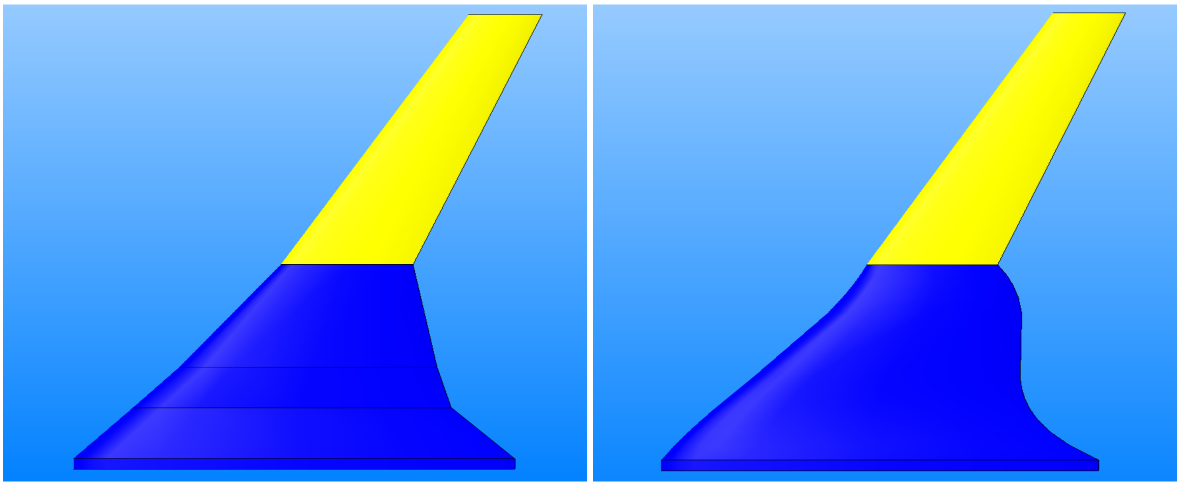

(a) Hybrid wing (χ = 0.45) with ruled lofting

(b) Hybrid wing (χ = 0.45) with C_2 continuity lofting

Figure 3.4: Different loftings on a hybrid wing with identical shape factors

An important observation from Figure 3.4a and Figure 3.4b is that the choice of lofting method interacts strongly with how the shape coefficients a_i define the spanwise distributions. Because the wing geometry is expressed as a polynomial of order N, changing a single a_i influences the curve globally, as shown by Equation 3.13. This ensures smoothness but also means that large disparities between coefficients can produce steep changes in chord or thickness between sections. When these strongly different sections are interpolated with a ruled loft, the surface is simply

$$S(u,v) = (1-v)\,C_i(u) + v\,C_{i+1}(u) \tag{3.14}$$

where $S(u,v)$ is the wing surface, u is the chordwise coordinate, v is the parametric coordinate, and $C_i(u)$ are the section curves. Each point interpolates linearly between two consecutive curves, so no instability occurs. By contrast, the B-spline loft, or NURBS surface, fits a smooth surface through all sections,

$$S(u,v) = \sum_{i=1}^{k}\sum_{j=1}^{l} R_{i,j}(u,v)\mathbf{P}_{i,j} \tag{3.15}$$

where $R_{i,j}$ contains the rational basis functions that include the weights, and $\mathbf{P}_{i,j}$ are the control points defining the geometry [54]. This formulation enforces C_1 and C_2 continuity across the surface. However, if a_0 is much smaller than a_1, the control points are pulled in opposite directions. This global coupling can bend the surface so strongly that parts of it fold backwards, which can reverse its direction. Mathematically, this is described when the Jacobian determinant is negative,

$$\det\left(\frac{\partial S}{\partial u} \times \frac{\partial S}{\partial v}\right) < 0 \tag{3.16}$$

where $\frac{\partial S}{\partial u}$ and $\frac{\partial S}{\partial v}$ are the tangent vectors. Their cross product gives the local surface normal, and a negative determinant indicates that the surface orientation has flipped [60]. In practice, this explains why ruled lofts almost always remain valid, while smooth lofts can fail for extreme combinations of a coefficients. As the shape factors are constrained by the requirements of a NURBS surface, there is a very large range where the shape factors are valid, which makes it difficult to find specific bounds that are universally valid.

Although this method allows for a very flexible wing design, there still needs to be direct constraints in place to ensure the design is valid both geometrically and aerodynamically. Most of these constraints are based on typical aircraft geometry. Using ParaPy, attributes can be created that ensure the constraints are respected, preventing the user from creating an unfeasible model. Also, ParaPy has a warning feature that returns a message to indicate if the constraint has been violated and returns a viable input to the geometry.

Table 3.2: Geometric Constraints and CST Shape Factor Bounds for the Wing Modelling

Parameter	Constraint	Notes
Chord at hybridization station	$c(\chi) > c_{\text{tip}}$	Ensures taper ratio < 1
Thickness-to-chord ratio	$0 < t/c < 0.5$	Prevents inverted or overly thick sections
Sweep angle Λ	$-60^\circ \leq \Lambda \leq 60^\circ$	Limits forward/backward sweep
Dihedral angle Γ	$-15^\circ \leq \Gamma \leq 15^\circ$	Avoids extreme vertical wing angles
Twist angle θ	$-10^\circ \leq \theta \leq 10^\circ$	Limits washout/washin

3.2.4 Fuselage and cabin design

The fuselage design is a key aspect to this modelling problem as it has to be able to morph between the fuselage of a typical tube-and-wing to the cabin of a blended wing body. Modern airlines no-longer have a perfectly cylindrical fuselage as they have been slightly more optimized. Some fuselage profiles indicate that he height is a bit greater than the width, usually to accommodate passengers and cargo more effectively. This means that a circular profile is not good enough to account for these changes. When the hybridization factor increases, the fuselage needs to gradually integrate within the main wing, until it is fully engulfed in the fairing, where it essentially becomes the cabin. Although they are not the same concept structurally, the shape and volume requirements are similar enough such that they can be modelled in a similar way. As it becomes more like the shape of a BWB cabin, the shape becomes more oval shaped. But this isn't sufficient to account for the ever-changing BWB cabin designs, as it can be deduced from the examples show earlier in subsection 2.1.2. The solution for this is to use a hyper-ellipse, also known as a superellipse. This is essentially an ellipse that can model any type of shape between a rectangle and an ellipse, by changing its exponential parameter, n. The equation for a full hyper-ellipse is as follows:

$$\left|\frac{x}{a}\right|^n + \left|\frac{y}{b}\right|^n = 1 \tag{3.17}$$

where a is the semi-axis length in the x-direction and b is the semi-axis length in the y-direction. This can also be written in its parametric equation form so that the x and y values can be handled separately:

$$x(\theta) = a\ \cos^{\frac{2}{n}}(\theta), \qquad y(\theta) = b\ \sin^{\frac{2}{n}}(\theta) \tag{3.18}$$

where $0 \leq \theta \leq \pi/2$.

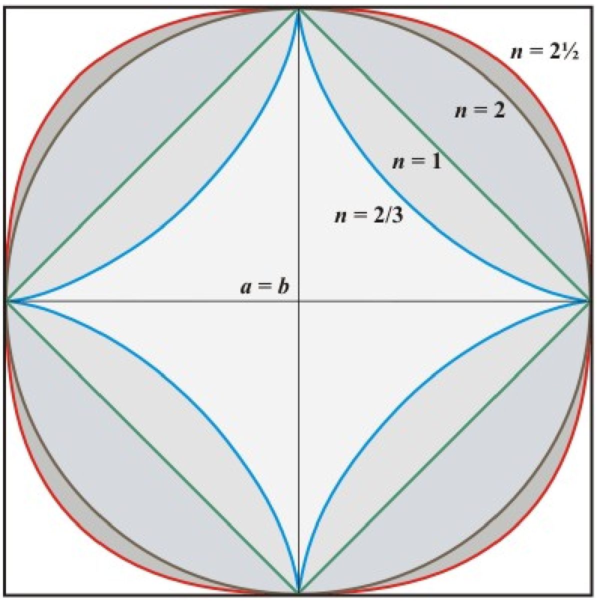

Figure 3.5: Graph of a super ellipse with a varying n parameter on all four quadrants [61]

In the hybridization model a modified hyper-ellipse is used, so that the top and bottom halves can have a different n values so that it can cover a wider range of shapes. This was also created as its own class so that it can be manipulated and reproduced easily.

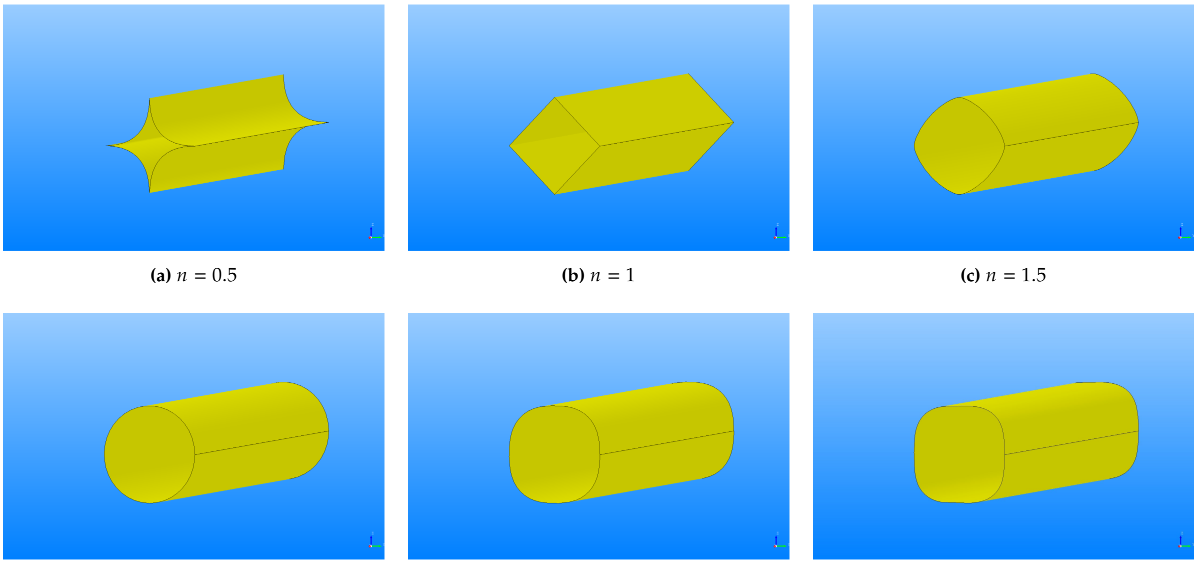
(a) $n = 0.5$ **(b)** $n = 1$ **(c)** $n = 1.5$

(d) $n = 2$ **(e)** $n = 2.5$ **(f)** $n = 3$

Figure 3.6: Variation of fuselage cross-section shapes for different roundness exponents n.

Now that the "morphing" requirements of the fuselage have been established, the hybridization factor needs to be related to its physical parameters. To ensure that the fuselage dimensions can be accurately modelled on a TAW but also transition rapidly to a BWB, a new parameter needs to be defined, the slender factor, τ. The hybridization factor χ is first scaled to a defined location where the TAW-BWB transition occurs, which is $\chi = 0.3$. This is done by using a minimum function, which returns 1 whenever $\chi > 0.3$,

$$u = \min\left(1, \frac{\chi}{0.3}\right) \tag{3.19}$$

The effective slenderness factor is obtained by implementing a decreasing cubic equation, which keeps the geometry nearly unchanged for low values of χ while enforcing a faster shrinking of the fuselage as χ increases.

$$\tau_{\text{eff}} = (1 - u^3)\,\tau - 2u^3 \tag{3.20}$$

where τ is the introduced *slender factor*. This parameter controls the evolution of the fuselage dimensions, and is mainly important when designing TAW. The fuselage height and width can then be correlated to χ and τ_{eff} by

$$h_{\text{raw}} = h_{\text{min}} + \tau_{\text{eff}}\,(1 - \chi) \tag{3.21}$$

$$w_{\text{fuse}} = h_{\text{min}} + (1 - \tau_{\text{eff}})\;(1 + \chi) \tag{3.22}$$

$$h_{\text{fuse}} = \max(h_{\text{min}},\; h_{\text{raw}}) \tag{3.23}$$

with a constraint ensuring that the height does not fall below the minimum allowable value. This approach was introduced to ensure that a wide range of wing and fuselage combinations can be represented. For example, an A320 and EMB-145 have a similar amount of fairing with respect to the length of the wing, but their fuselage profile is slightly different; the A320's fuselage is slightly taller than it is wider. This allows for new geometric coupling to be explored, the hybridization factor with the slender factor. By changing theses two variables, one can achieve a plethora of different aircraft shapes. When $\tau = 0.5$ it resembles a cylindrical fuselage, a greater value than this makes the height larger than the width and a smaller value makes the width larger than the height.

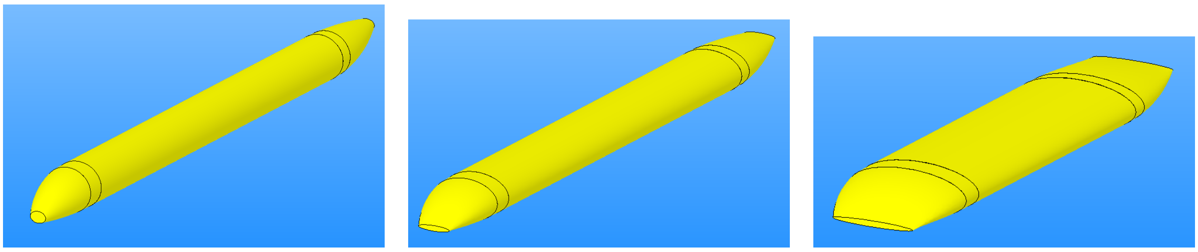

(a) Hybridization factor, $\chi = 0.1$ **(b)** Hybridization factor, $\chi = 0.2$ **(c)** Hybridization factor, $\chi = 0.3$

Figure 3.7: Variation in fuselage dimensions with respect to the hybridization factor, χ, for a slender factor $\tau = 0.5$

Another important requirement of the fuselage is that it is constrained at a constant volume, so the length is derived from it. As the shape of the super-ellipse is subject to great change, the cross-sectional area calculation requires specific attention. The following attribute is derived using the gamma function:

$$A_{\text{hyper}} = 4ab\frac{(\Gamma(1 + \frac{1}{n}))^2}{\Gamma(1 + \frac{2}{n})} \tag{3.24}$$

$$\Gamma(z) = \int_0^{\infty} t^{z-1}e^{-t}\,dt \tag{3.25}$$

where n is the shape parameter or "roundness" coefficient. Once this is obtained, the hyper-ellipse area is used to find the length of the fuselage.

$$L_{\text{fuse}} = \frac{V_{\text{fuse}}}{A_{\text{hyper}}} \tag{3.26}$$

where n is the shape parameter or "roundness" coefficient. The python implementation of these attributes and the HyperEllipse class is shown in section B.3. The goal of using this parameterization is to accommodate as many possible fuselage designs as possible, with as little parameters as possible.

The y-positioning of the fuselage is always assumed to be centered over the center airfoil, and the x and z positioning, as well as the rotation about the y-axis, is an input for the designer. This was selected to be an input to allow for more flexibility when designing aircraft. Automating the position is possible, however, deciding one specific location for the fuselage with respect to the fairing geometry is difficult due to its configuration-specific nature.

3.2.5 Fuselage Nose and Tail

For more conventional configurations, a simple yet parametric nose and tail cone needs to be modelled. The nose and tail of the fuselage makes use of the HyperEllipse class to create the distribution of profiles. This way it can maintain the same level of flexibility as the fuselage. The height and width of the nose ellipses begins as the same width as the fuselage and then decrease depending on the desired curvature

$$w_{\text{nose},i} = w_{\text{fuse}} - s_{\text{nose}}\, i \tag{3.27}$$

$$h_{\text{nose},i} = h_{\text{fuse}} - s_{\text{nose}}\, i \tag{3.28}$$

where s_{nose} is the nose scaling factor and i is the index of the profiles. To get the desired length and droop of the nose, the x a z translations of the profiles need to be addressed.

$$x_{\text{nose},i} = x_{\text{fuse}} - d_{\text{nose}} \sqrt{\frac{i}{N_{\text{nose}}}} \tag{3.29}$$

$$z_{\text{nose},i} = z_{\text{fuse}} - h_{\text{nose}}\, s_{\text{nose}}\, i \tag{3.30}$$

x_{fuse} and z_{fuse} are the x and z translation of the fuselage, d_{nose} is denoted as the nose spacing factor, h_{nose} is the height of the tip of the nose and N_{nose} is the number of nose profiles. Equation 3.29 uses a square-root spacing law in order to get the desired curvature of the nose. It is important to note that the tail cap is parameterized in the same way.

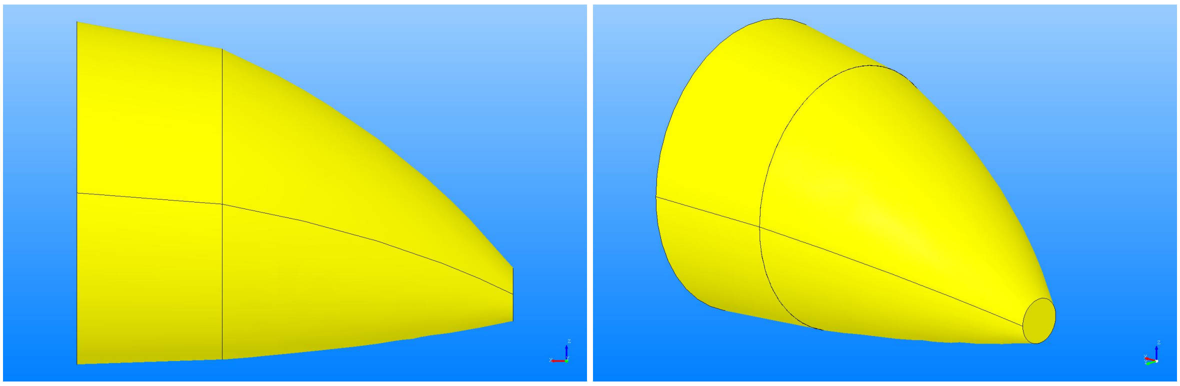

Figure 3.8: Geometry of the hyperellipse nose

Using this parameterization, the user can then implement a simple over-nose angle constraint using the tip height and nose spacing factor

$$\theta_{\text{over-nose}} = \arctan \frac{h_{\text{tip}}}{d_{\text{nose}}} \tag{3.31}$$

this can be rearranged and substituted for the h_{tip} in Equation 3.30 to get

$$z_{\text{nose},i} = z_{\text{fuse}} - d_{\text{nose}} \tan \theta_{\text{over-nose}} \cdot s_{\text{nose}}\, i \tag{3.32}$$

This provided a simple formulation to generate a nose and tail for a plethora of aircraft. The hybridization factor is still respected, as the width and height of the nose relies on the width and height of the fuselage. Nevertheless, it still required a moderate amount of inputs for a relatively simple design. The fuselage nose and tail raised issues when transitioning from a conventional design to a BWB design, as the stretching of the nose tip causes it to become very thin causing the geometry to break. Integrating the classical cockpit shape into a highly-blended BWB was not straightforward as the circular cross-section of the cockpit has to fuse with the leading edge of the airfoil shaped fuselage, requiring additional fairing to be modelled such that it had a smooth transition. This was chosen to be ignored for this study, as many conceptual BWB designs just keep the same center-body leading-edge airfoil shape [14] [28].

3.2.6 Winglet and Tail Design

As the intention of this application is to be able to model a wide range of configurations, the tails and control surfaces must also be easily interchangeable. Most BWB designs do not use the conventional cross-tail or T- Tail configuration, they usually opt for a winglet or V-Tail design. The design of these surfaces uses the CST AirfoilCurve class to create a root and tip airfoil, then they are simply lofted to generate a basic wing section. The initial idea was to automatically size the tail based on the sizing of the aircraft, but as the model can have large changes in the geometry, the aerodynamics also change greatly. Therefore, it was decided to use the classical inputs for the tail, such as chord, span, sweep, and so on.

3.2.7 Landing Gear

The design of the landing gear is done in a simple fashion, cylinders are used for the struts, axles and wheels. This is put together in a LandingGear class Appendix B so that they can easily be instantiated and multiplied. This way the designer can easily switch from a tricycle to a bogey configuration.

The important aspect of the landing gear is how it is positioned with respect to the aircraft. The positioning of the landing gear on a TAW changes greatly to that of a BWB. But, what doesn't change are the conditions for the landing gear. Aside from maintaining a balanced aircraft on the ground, the most basic conditions for the landing gear are[62]:

1. They should allow the aircraft to have sufficient take-off roll without striking the tail or fuselage
2. They should be tall enough such that the wings of the aircraft do not touch the ground when landing due to flex or a banked landing.
3. They should be able to withstand the impact forces from landing and aerodynamic forces when taking off.

To ensure the first two requirements are met, the landing gear was sized to meet the banked landing requirement and a warning was introduced to make sure the aircraft had the desired take-off roll without striking the tail. Therefore, the length of the struts was calculated using the span of the aircraft and the minimum lateral clearance angle.

$$L_{strut} = b\tan(\theta_{\text{lat, min}}) \tag{3.33}$$

Once the strut length was constrained, the following procedure was carried out to verify the tail clearance angle:

$$L_{\text{gear}} = L_{\text{strut}} + r_{\text{wheel}} \tag{3.34}$$

$$d_{\text{tail}} = \left(L_{\text{fuselage}} + x_{\text{fuse}}\right) - x_{\text{gear}} \tag{3.35}$$

where x_{fuse} and x_{gear} are the fuselage and landing gear x-positions and d_{tail} is the complete distance from landing gear to tail. Next, the actual clearance angle of the model was calculated and compared to the minimum allowed clearance angle

$$\theta_{\text{tail, actual}} = \arctan\left(\frac{L_{\text{gear}}}{d_{\text{tail}}}\right) \tag{3.36}$$

Then the condition was placed that if $\theta_{\text{tail,actual}} < \theta_{\text{min,clearance}}$, a warning is raised to inform the user that the model is at risk of tail-striking. The minimum clearance angle is also known as the "scrape angle". This outlines a simple way that landing gear can be sized on an aircraft, regardless of configuration. However, many more requirements for the landing gear could be implemented into the application, like automatic positioning depending on the CG and automatic FEM analysis to ensure the struts can withstand the necessary loads.

3.3 Calculation of Attributes

To help with general analysis and CFD, several attributes were integrated into the application, allowing for automated calculations when the geometry is changed. The CG, aerodynamic center and neutral point are very useful for the application as the designer can get a rough idea of the aircraft's flight behaviour.

3.3.1 Center of gravity

The calculation of the center of gravity is found through a weighted sum of the individual components, which are the fuselage, wing, tail and tanks. As this model does not take into account any structural considerations like ribs and spars, the center of gravity of each component is found using ParaPy's COG attribute. The x,y,z coordinates are found as follows:

$$x = \frac{w_f \cdot x_{cg,f} + w_w \cdot x_{cg,w} + w_e \cdot x_{cg,e} + w_t \cdot x_{cg,t}}{w_{\text{total}}} \tag{3.37}$$

where w is the weight, x_{cg} is the x-coordinate of the components CG and the subscripts f, w, e and t are the fuselage, wing, empennage and tail, respectively. The y and z coordinates are found in the same manner. As the structure and weight estimation is not included in this study, the weights of the components will be inputs to the application.

3.3.2 Aerodynamic Center

To calculate the aerodynamic center of the wing, the location of the aerodynamic center for each airfoil section needs to be found. This is done as follows,

$$x_{AC,i} = x_{LE,i} + h_{ac} \cdot c_i \tag{3.38}$$

where x_{LE} is the leading edge position, c_i is the chord of the specific section and h_{ac} is the fractional position of the aerodynamic center, which is taken to be at the quarter-chord, $h_{ac} = 0.25$, as a simplification. This assumption is acceptable for near-symmetrical airfoils. The coordinates of each airfoil section are very easily obtained using the AirfoilCurve class again.

Then, the average of this x-position is calculated and substituted into the equation below to get the aerodynamic center as a fraction of the root chord.

$$AC_{\text{frac}} = \frac{\bar{x}_{AC} - x_{LE,\text{root}}}{c_{\text{root}}} \tag{3.39}$$

3.3.3 Neutral point

The neutral point describes the location measured from the leading edge of the mean aerodynamic chord for which the center of gravity would have no change in moment with respect to a change in angle of attack, $\frac{\partial C_{M,cg}}{\partial \alpha} = 0$, this is calculated using [63],

$$h_n = h_{\text{ac, wing-body}} + V_H \frac{a_t}{a} \left(1 - \frac{\partial \epsilon}{\partial \alpha} \right) \tag{3.40}$$

where $h_{\text{ac, wing-body}}$ is the chordwise location of the aerodynamic center of the main wing on the mean aerodynamic chord, a and a_t are the lift curve slopes of the wing and tail respectively and $\frac{\partial \epsilon}{\partial \alpha}$ is the change in downwash with a change in angle of attack. The horizontal tail volume coefficient is given as,

$$V_H = \frac{l_t S_t}{c S} \tag{3.41}$$

where l_t is the distance from the aircraft CG to the aerodynamic center of the tail, S_t is the area of the tail, c and S are the mean aerodynamic chord and area of the wing. For tail-less BWB configurations, the horizontal area contribution of the winglet was used instead and were assumed to have $\frac{\partial \epsilon}{\partial \alpha} = 0$.

3.4 Overview of inputs

Due to the CST formulation, the fuselage and wing can be modelled with a modest amount of parameters. These parameters are shown below in Table 3.3, and do not include the inputs for the tail and landing gear, as they are not the main focus of the validation. Most of these inputs have already been defined earlier in the chapter, but there are a few positional arguments that require description.

Table 3.3: Main geometry inputs with units and descriptions

Input	Unit	Description
χ	[-]	Hybridization factor
τ	[-]	Slender factor
b	m	Wing span
Λ	°	Leading edge sweep angle
c_{root}	m	Root chord length
c_{tip}	m	Tip chord length
t_{root}	[-]	Root thickness
t_{tip}	[-]	Tip thickness
i_{root}	°	Root incidence angle
θ_{twist}	°	Wing twist angle
Γ	°	Wing dihedral angle
z_{wing}	m	Vertical placement of wing
Y_i	[-]	Spanwise station coordinate (Equation 3.42)
a_c	[-]	Chord shape factor
a_t	[-]	Thickness shape factor
a_i	[-]	Incidence shape factor
a_x	[-]	x-position shape factor
a_z	[-]	z-position shape factor
$a_{U,\text{root}}$	[-]	Upper surface root airfoil shape parameter
$a_{L,\text{root}}$	[-]	Lower surface root airfoil shape parameter
a_U	[-]	Upper surface tip airfoil shape parameter
a_L	[-]	Lower surface tip airfoil shape parameter
h_{min}	m	Minimum fuselage height (Equation 3.23, Equation 3.22)
x_{fuse}	m	Longitudinal location of fuselage
θ_{fuse}	°	Pitch rotation of fuselage
z_{fuse}	m	Vertical offset of fuselage
n	[-]	Fuselage cross-section roundness ratio (Equation 3.17)
V_{fuse}	m	Fuselage volume
d_{nose}	m	Nose displacement factor (Equation 3.29)
h_{nose}	m	Nose tip height (Equation 3.28)
N_{nose}	[-]	Number of nose profile sections (Equation 3.29)
s_{nose}	[-]	Nose width and height scaling factor (Equation 3.27, Equation 3.28, Equation 3.30)
$n_{\text{nose-tail}}$	[-]	Roundness factor for nose and tail
d_{tail}	m	Tail displacement factor (Equation 3.29)
h_{tail}	m	Tail tip height (Equation 3.28)
N_{tail}	[-]	Number of tail profile sections (Equation 3.29)
s_{tail}	[-]	Tail width and height scaling factor (Equation 3.27, Equation 3.28

For the wing, 2 profiles were added on the inboard section of the aircraft to better represent the fairing. This number was selected so that the fairing would be described with 4 profiles and 4 shape factors to make the variation of the shape factors more intuitive. However, these two inputs are independent from one another and do not have to be equal to each other. These profiles take the spanwise-specific inputs from the 3D CST functions, which are inputted to the CST airfoil curve. To do this, these profiles also had to be parameterized with the hybridization factor.

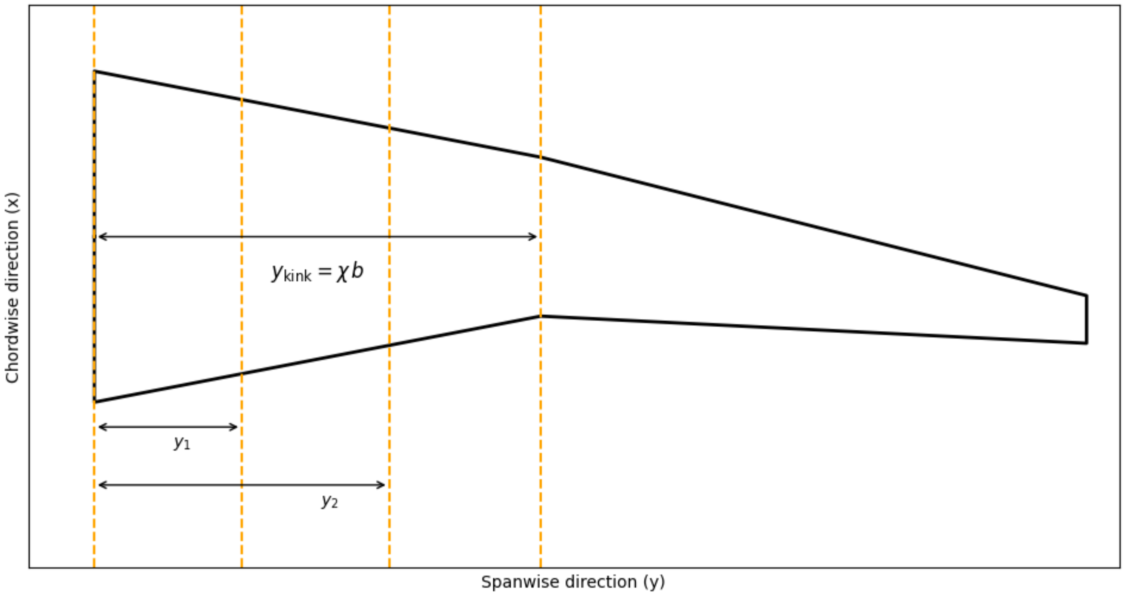

Figure 3.9: Diagram showing spanwise wing inputs

where,

$$y_1 = Y_1 \cdot \chi \cdot b \tag{3.42}$$
$$y_2 = Y_2 \cdot \chi \cdot b \tag{3.43}$$
$$Y_2 > Y_1 \tag{3.44}$$

From these equations it can be seen that the position of the inserted airfoils is still dependent on the hybridization factor, meaning they will shift accordingly. The amount they shift is dependent on the Y_i values. These profiles will be equally spaced and remain this way for most configurations, these only need to be adjusted when very specific curvature is required at a given location. The other option instead of doing this would be to add many more profiles and increase the number of a factors to get a closer representation. This will be further explained in section 4.4.

To get the fuselage to fit within the fairing in BWB configurations, its position must be modifiable. That is why its horizontal, vertical and rotation are included as inputs. Due to the nature of an airfoil shape, to maximize the height of the fuselage/cabin, it sometimes needs to be rotated. Figure 3.10 illustrates this clearly. Another important input for the fuselage is the fuselage position which dictates where the fuselage is placed in the x-direction or streamwise direction. The reference axis begins at the leading edge of the center airfoil, with the positive x-direction pointing towards the tail of the aircraft and the positive y-direction pointing towards the starboard wing.

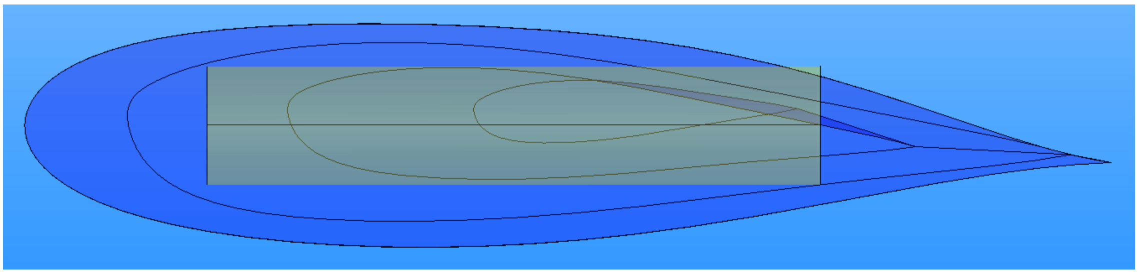

(a) Fuselage Rotation = 0°

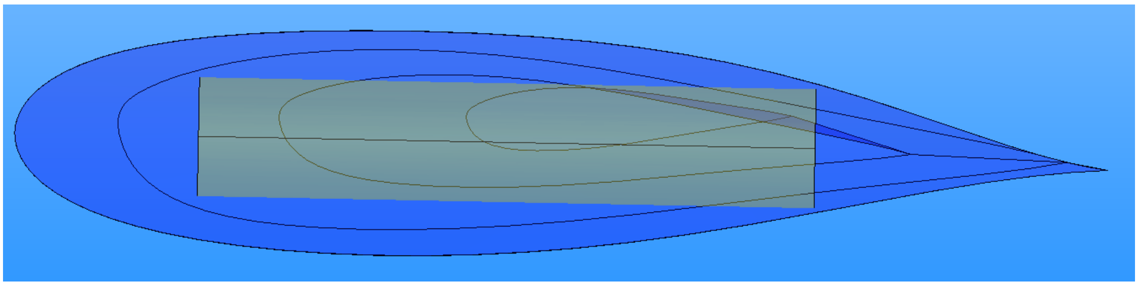

(b) Fuselage Rotation = 1.125°

Figure 3.10: Unrotated and rotated fuselages within a BWB

3.5 Order of Operations

As the model is desired to be able to model all possible aircraft between a TAW and a BWB, it requires a certain degree of flexibility. This means that simply changing the hybridization factor is not enough to model the BWB-equivalent of a tube and wing configuration. However, with a modest amount of steps, it is possible to accurately model both a fairing on a TAW and also transition that TAW configuration to a BWB. Getting the right set of shape factors can take some time initially, but the key innovation is that once they are set up, it makes it much easier to explore the different curvatures and distributions that are possible for a given configuration. The main objective for most of the steps for adjusting the shape factors is to achieve a convex-concave curvature distribution for the fairing with a smooth transition to the outboard wing, as shown in Step 4 and Step 5 in subsection 3.5.2. This smooth transition to the outboard wing causes the outboard centerbody fairing to be concave, which requires the rest of the fairing to be convex in order to remain smooth. This is done to reduce supervelocities in this area to prevent interference drag and wave drag at high-subsonic mach numbers [19] and also to prevent the generation of unwanted vortices.

An important aspect that can be seen from the modelling workflow is the continuity between the fairing and the outboard wing, which only complies with C_0 continuity, meaning there the first and second derivatives do not have to be equal at the intersection. This is done to allow for a larger flexibility when making design choices, like having a sharp kink at the leading edge.

3.5.1 Conventional Model Creation

Step 1

Create the TAW geometry by inputting the typical wing parameters (chords, thickness ratios) and the fuselage parameters (minimum height and volume), as shown in Table 3.3. The CST airfoil coefficients for the wing, kink and root should also be inputted here.

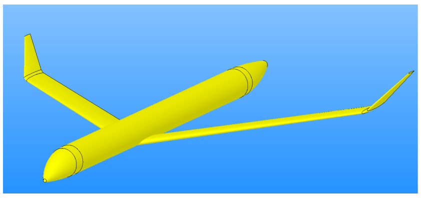

Step 2

Increase the hybridization factor to $\chi = 0.1$, as this was found to represent the size of the TAW fairing accurately. Set all shape factors to zero. Modify the slender factor, τ, so get the desired fuselage cross-section. Here it was set to $\tau = 0.5$ to get an almost circular cross-section.

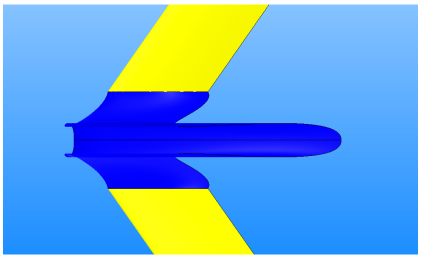

Step 3

Increase the chord shape factors (a_c), working from the first value to the last (from inboard to outboard). In the shown example, the second chord shape factor a_{c2} was increased to approximately 4. The last chord shape factor a_{c4} must be increased until the desired outboard wing chord length is achieved. The third chord shape factor must be adjusted to achieve a convex–concave distribution on the trailing edge.

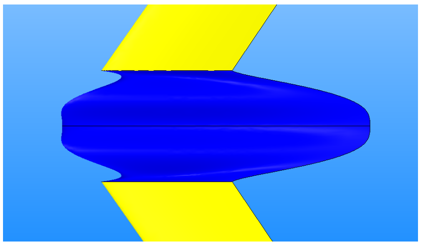

Step 4

Adjust the x-positioning shape factors (a_x) to obtain the same convex–concave curvature on the leading edge of the fairing. Begin by keeping the first x-position factor a_{x1} at 0. The second factor a_{x2} should be small and slightly positive to create the convex portion, and the third factor a_{x3} should be slightly negative to generate the concave portion.

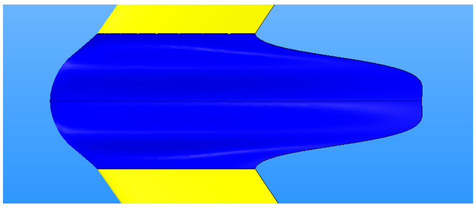

Step 5

Adjust the intermediate thickness shape factors a_{t2} and a_{t3} to achieve the desired curvature on the upper surface. A suitable range for these values is between 0.5 and 2. To obtain a rapid thickness decrease between the inboard and outboard portions of the fairing, ensure $a_{t2} \leq a_{t3}$. This encourages concavity near the wing root. a_{t1} should remain 0 unless modification of the t_c of the center airfoil is required. a_{t4} should be adjusted until the t_c of the outboard wing root airfoil is obtained.

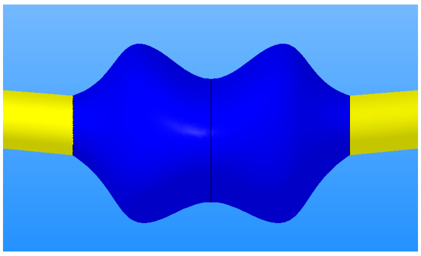

Step 6

Adjust the z-positioning shape factors (a_z) to achieve the ideal convex-concave curvature on the lower surface of the fairing. A useful range for these values is approximately ±0.1. In this example, the first z-positioning shape factor (a_{z1}) is decreased, while the second and third (a_{z2} and a_{z3}) are increased. This lowers the centre section and raises the outboard portion. Here the incidence angle distribution, a_i, can also be tweaked for a recommended range of ±1, leaving the values equal to 0 will maintain the baseline twist distribution, which was done for this example.

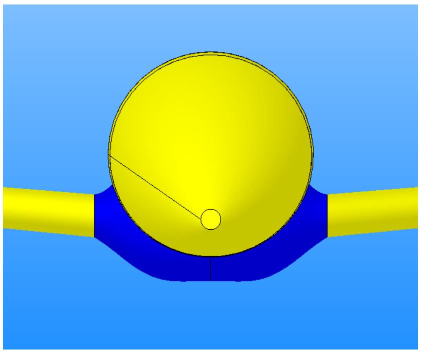

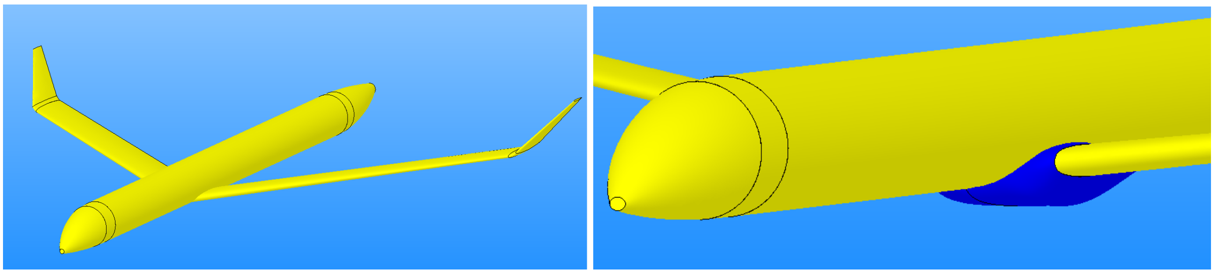

(a) Baseline tube-and-wing geometry

(b) Fairing created with hybridization factor, $\chi = 0.085$

Figure 3.11: Creation of fairing on a conventional aircraft

Table 3.4: Key inputs for the TAW creation

Input	Value	Unit
χ	0.1	[-]
τ	0.75	[-]
c_{root}	6.07	m
c_{tip}	1.64	m
h_{min}	3.7	m
x_{fuse}	-10	m
z_{fuse}	1	m
a_c	[0, 4, 0.15, 0.15]	[-]
a_t	[0, 0.85, 2, 0.325]	[-]
a_i	[0, 0, 0, 0]	[-]
a_x	[0, 0.1, -0.2, 0]	[-]
a_z	[-0.075, 0.025, 0.025, 0]	[-]

3.5.2 Creating a Blended Wing-Body From a Conventional Model

Step 6

Using the TAW baseline geometry, begin increasing the hybridization factor to a value between 0.3 and 0.6, as this is a typical range for a BWB planform. In this case, it was increased to $\chi = 0.4$.

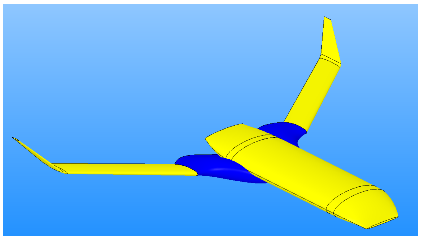

Step 7

Position the fuselage in both the streamwise and vertical directions so that its center is in line with the trailing edge of the outboard wing. This can be adjusted to the specific static-margin requirements of the aircraft.

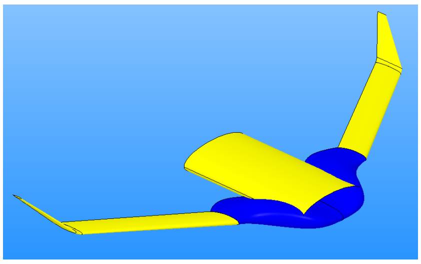

Step 8

Increase the root chord until the edges of the fuselage are just tangent to the centre airfoil surface. Increase the second and third chord-shape factors (a_{c2} and a_{c3}) in increments of 0.1 until the fuselage is fully enclosed and the trailing-edge convex–concave curvature is restored. The last shape factor (a_{c4}) should stay the same to keep the outboard wing root chord constant.

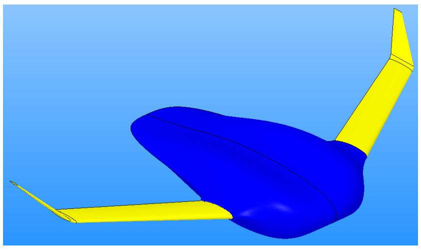

Step 9

Adjust the thickness-to-chord shape factors, a_t, and the z-positioning factors, a_z, to control the volumetric distribution and maintain the convex-concave curvature, ensuring that the fuselage does not become visible through the outer surface. For a BWB, a_t typically varies between 0 and 1, while a_z ranges from 0.5 to -0.5.

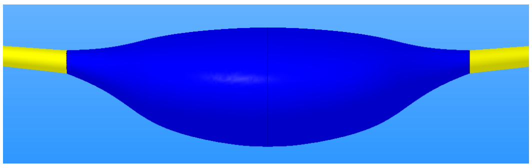

Step 10

Adjust the x-positioning shape factors, particularly the fourth (a_{x4}), to set the desired relative position of the outboard wing compared with the center-body, ensuring the aircraft's center of gravity remains slightly ahead of the neutral point. The second and third factors (a_{x2} and a_{x3}) may also be tuned by approximately ±0.1 if the convex–concave curvature of the leading edge has been affected, but they typically require little modification if the earlier steps are followed correctly. It is normal for there to be extra space in the aft portion of the centerbody due to the greater thickness of the airfoil. This is so that the fuselage can fit, whilst maintaining the thickness-ratio of the airfoil.

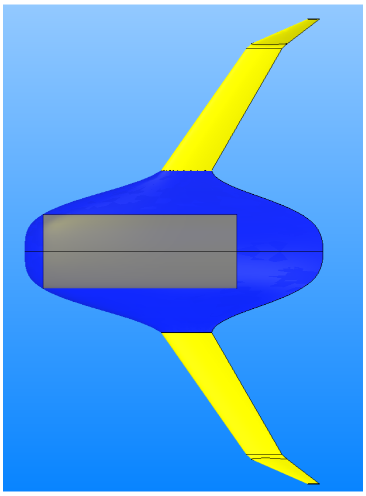

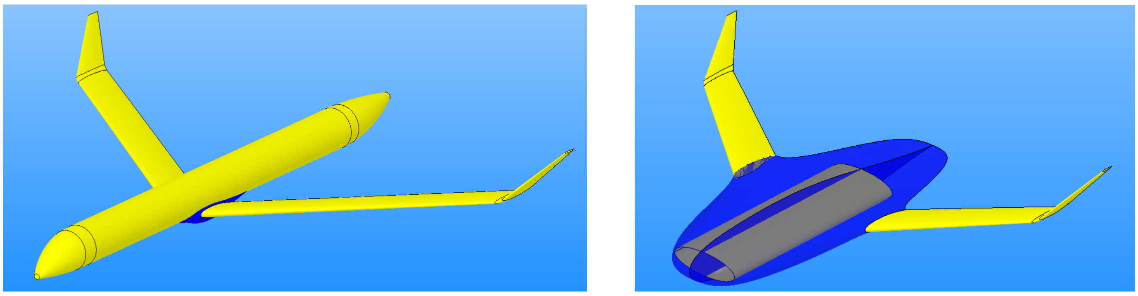

(a) Basic tube-and-wing geometry with fairing

(b) BWB created with hybridization factor $\chi = 0.4$

Figure 3.12: Creation of BWB from a conventional aircraft

Table 3.5: Key inputs for the BWB creation

Input	Value	Unit
χ	0.4	[-]
τ	0.75	[-]
c_{root}	25	m
c_{tip}	1.64	m
h_{min}	3.7	m
x_{fuse}	1.25	m
z_{fuse}	0.1	m
a_c	[0, 5.5, 0.25, 0.15]	[-]
a_t	[0, 0.85, 0.75, 0.325]	[-]
a_i	[0, 0, 0, 0]	[-]
a_x	[0, 0.1, -0.2, 2]	[-]
a_z	[-0.075, -0.15, -0.15, 0]	[-]

3.6 Limitations

When looking at the application itself, one main limitation is the fact that the hybridization factor and shape factors are uncoupled. Changing the hybridization will change the size and curvature of the fairing, but not the specific shape factors. This means that it is not yet possible to have a single slider that completely converts a TAW to a BWB, rather it requires a modest amount of steps. This also means that the curvature requirements and constraints need to be manually selected and checked. Because of this, creating a baseline design can be initially slow. However, once the design is established, making changes to its external geometry becomes very quick due to the shape factors from the CST formulation. Table 3.6 outlines the important aspects of the application that are calculated and generated automatically, as well as what needs to be done manually.

Table 3.6: Manual and automated capabilities of the application

Automated	Manual
Geometry Generation	Initial Geometry Inputs
Aerodynamic and Mass Calculations	Fairing Curvature Constraints
Mesh Creation	Fuselage Positioning
FlightStream Script Creation	Tank Positioning

In terms of the type of aircraft that can be modelled, most monoplane wings can be modelled. A strut-braced wing for example is not a common design for aircraft of this caliber, so this will not be something considered in the application. This means that other wing layouts like a box-wing or bi-plane will also not be modeled. As this is focused on commercial and cargo applications, there will be a constraint on the minimum volume and minimum height of the fuselage, so that there is sufficient space for cargo and/or passengers. That being said, the cross-section of the pressure vessel will also be limited to the possible shapes of a super-ellipse, but mainly focusing on oval and quasi-rectangular sections extruded in a tubular manner. This also means that concepts like the double-bubble pressure vessel wont be modelled. Pressure vessels found in gliders, for example, have a significant lengthwise variation in profile and will not be modelled. This is also the case for smaller aircraft like a Cessna 152, as the fuselage cross-section also varies greatly. Aircraft with unconventional control surface configurations like canards will also not be modelled. The application is also limited to aircraft that have externally mounted engines. Boundary layer ingestion (BLI) concepts require that the external geometry is tailored so that the engine inlet receives the adequate airflow. This study is not focused on engine integration, so it will also not be considered in the model. The landing gear will be modelled simply as struts and wheels. The configuration will mainly be either bogey or tricycle. Tail draggers have been excluded from this research as they are mainly considered for smaller or medium-sized aircraft.

3.7 CFD Analysis: Altair Flightstream

Flighstream poses itself as a medium-fidelity CFD tool that is highly effective for conceptual and preliminary design testing due to its fast convergence. Flightstream modernizes traditional panel methods by incorporating several enhancements to provide more accurate and efficient analyses. Traditional panel methods discretize the aircraft surface into panels and solve for the flow field using singularity distributions. While efficient, these methods often neglect viscous effects and compressibility, limiting their accuracy in certain flight regimes. Classical vortex panel methods, being based on inviscid and irrotational potential flow, cannot predict pressure drag because the solution contains no flow separation or wake formation. Flightstream addresses these limitations by integrating compressibility models, allowing for simulations across a wide range of Mach numbers. It uses an integral boundary layer model to account for viscous effects, providing more realistic predictions of aerodynamic loads and allowing for the evaluation of pressure drag. Additionally, Flightstream introduces viscous-coupling equations that model the thickening and decambering effects of boundary layers, enhancing the accuracy of aerodynamic predictions. These features make Flightstream a versatile and powerful tool for aerodynamic analysis, bridging the gap between traditional panel methods and more computationally intensive CFD approaches.

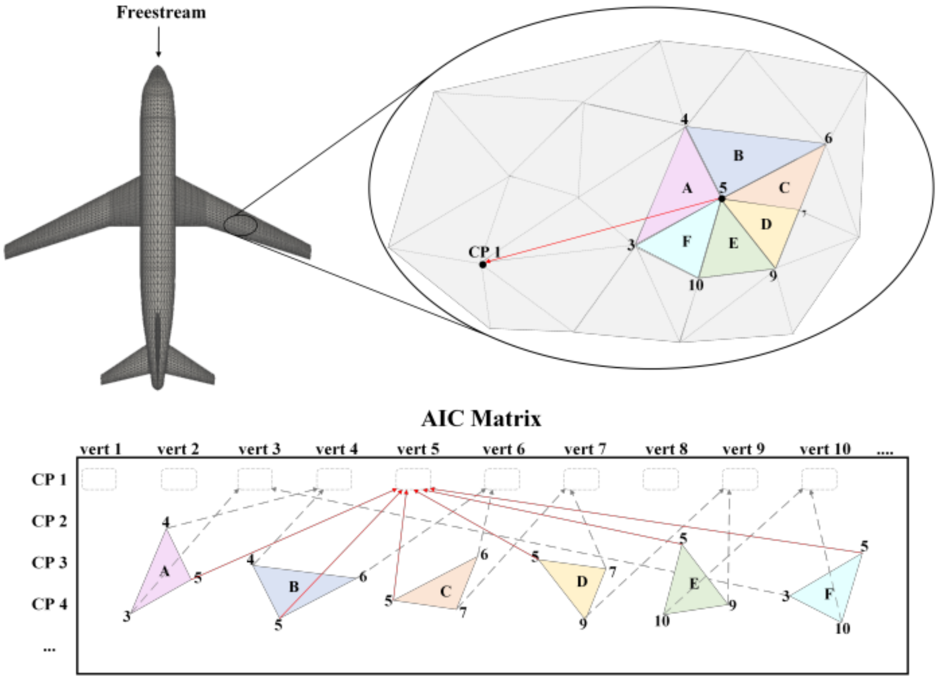

Figure 3.13: Figure showing how the AIC matrix is created from an element [64]

Another reason why Flightstream was selected for this analysis is its fast mesh creation using its unique Component Cross Section (CCS) based meshing. This allows the user to input the 3D coordinates of components, like airfoils or fuselage profiles, in a comma-separated file and it automatically creates a mesh between them. Many parameters can be included in this input file such as the spanwise and chordwise mesh density, TE conditions and continuity constraints. This allows the designer to make many changes to the design, without needing to spend a lot of effort meshing, which is very important if a wide range of designs need to be analyzed. This, of course, has its drawbacks, as a detailed and configuration-specfic mesh will always yield more accurate results. The CCS meshing also allows for various components to be united using OpenVSP's boolean unite feature. Extra care has to be placed whenever two meshes are united because if the mesh density between the two components is not similar, it can lead to highly skewed cells in the junction region of the mesh.

An interface between ParaPy and FlightStream was created so that the model could be iterated quickly. To do this, two scripts had to be created. One to create the CCS mesh and another to set up and run FlighStream directly from the ParaPy GUI. Thankfully, the main functions to create the FlightStream script had already been established in the ParaPy library, but as this is a new feature they are implementing, it did not include all of the scripting functions, which had to written by the authors.

Chapter 4

Validation

To assess the capabilities of this model, it must be tested against known aircraft. To do so, the planforms of a selection of conventional and unconventional aircraft are used to compare how accurate the hybridization model is, both visually and numerically. The main idea is to see how easy it is to match the geometry of a variety of aircraft using this new approach. The conventional aircraft selected for this validation was the Embraer EMB-145 and the Airbus A320, as information on these aircraft is readily available. For the unconventional aircraft, the Aurora D8 and a BWB concept introduced by Dommelen and Vos [28] were selected. The D8 is a key aircraft for this validation because it highlights a "grey-area" between a conventional and unconventional configuration.

4.1 Methodology for validation

The goal of the validation is to use the hybridization model to generate aircraft geometries that matching existing reference aircraft planforms within ±3% planform area deviation. If the front, side and top planform areas are within this deviation range, then the *means of compliance* of the aircraft can be roughly evaluated. In aircraft design, the means of compliance refers to the methods, analyses, and tests used to show that the aircraft meets all applicable airworthiness requirements. Essentially, it defines how the designer proves the aircraft is compliant with certification standards. If an already existing aircraft has met these standards, then the means of compliance of the model aircraft can be judged by how close it represents the reference.

Aside from areas, the volume of the aircraft is also evaluated. The volume of the wing is estimated based on a trapezoidal formula and using a shape factor of 0.5 for the airfoil area approximation. This way it is consistent for all the aircraft, as they have large variations in planform and lofting. As the volume will have larger discrepancies, the acceptable threshold will be set to ±5%. The fairing curvature is also examined, which is defined as the curvature of the lower surface of the fairing when viewed from the front. The fuselage accuracy is judged through its geometrical parameters along with some non-dimensional parameters like eccentricity and fineness ratio. The fairing curvature is defined as the 2-D curvature from the front view of the aircraft, this is automatically calculated for the model using a curvature formula attribute. The planform area, volume and curvature will be the key performance indicators for the validation. They will be validated numerically and also qualitatively, as the planforms will be created and overlayed on top of the model. The reference planform will be shown as the red outline as shown, for example, in Figure 4.3.

4.2 Embraer EMB-145

The EMB-145 is a classic T-tailed, medium-sized airliner that has been around since the 1990s, and has had signifcant success in the industry due to its reliable and efficient design. It has been one of the main actors for regional routes and continues to do so to this day.

The results from the validation show that the application can quickly and easily represent a medium-sized T-tail aircraft. The inboard section or fairing of the wing is sized using a hybridization factor of $\chi = 0.1$, which perfectly matches the spanwise position of the kink. The fuselage is represented accurately by using a slender factor of $\tau = 0.6$. The wing dimensions match the reference metrics exactly as seen in Table 4.1. An interesting characteristic of this new parameterization is shown through the third value of the a_c shape factors, which is negative. This shows how the shape factors serve as weights to the overall distribution. Changing one of them affects the entire wing, not just the value at a specific location. If there is a sudden change in chord, from large to small, the first factor, e.g. a_{c2} may be large and positive, and the second one, e.g. a_{c3}, would be negative. Because of this, it is good practice to begin shaping the wing from the root and work towards the tip. The fuselage also shows strong agreement with the reference, its width, length and height are all within a few centimeters difference. The eccentricity is ever so slightly different due to the fact that the fuselage width and height are based on the hybridization factor and the slender factor, which do not use the exact inputs of width and height. The fairing curvature is slightly different, indicating that the model fairing is slightly tighter, which could be alleviated by adding more profiles. This curvature is achieved by having mostly negative values for the z-positioning shape factors, a_z. To ensures that the center of the fairing is moved down, the second and third a_z values are more negative than the first and last, as seen from Table 4.2. The comparison of projected areas further supports these findings, as shown in Table 4.1. The top view area is very close, whilst the side and front areas vary slightly. This is mainly due to small differences in how the nose and tail are modelled, which were designed to be very flexible and not aircraft specific. The root airfoil, seen clearly in Figure 4.4 was matched very closely using the $a_{\mathrm{U,root}}$ and $a_{\mathrm{L,root}}$ coefficients. For example, the first value for the $a_{\mathrm{L,root}}$ is less negative in comparison to the rest, which represents the front loading of the airfoil.

As this was the first aircraft to be validated, it served as the "test dummy", allowing for improvements to be made to the model. Initially, the idea was to just define the wings z-positioning using the wing vertical position and dihedral, Λ, but this greatly limited how the fairing could be modelled, which is why the a_z shape factors were introduced. Later on, this addition would also prove to be very useful when modelling unconventional aircraft.

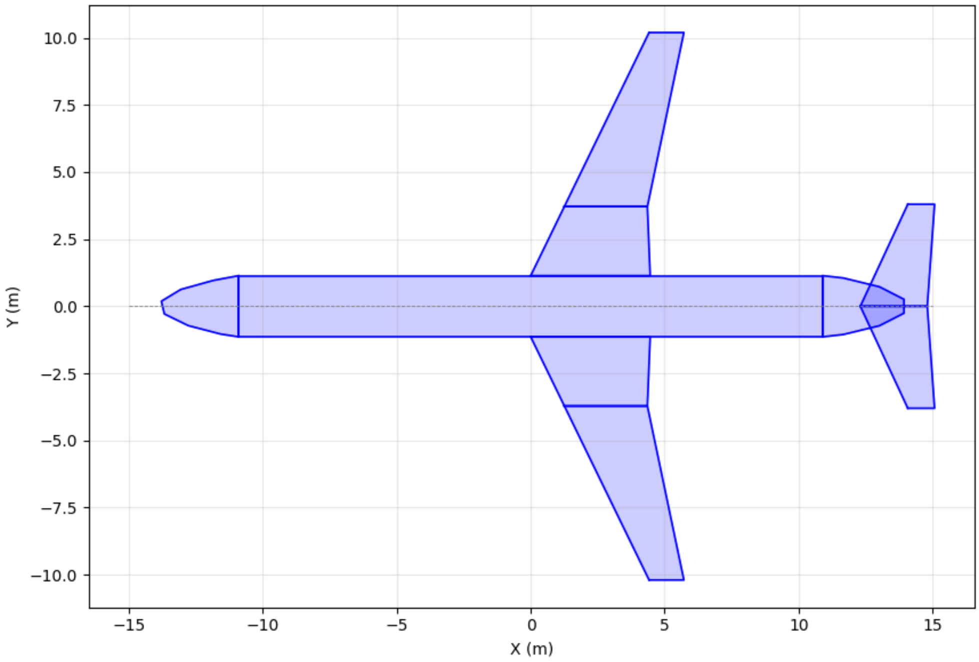

Figure 4.1: EMB-145: Reference top planform

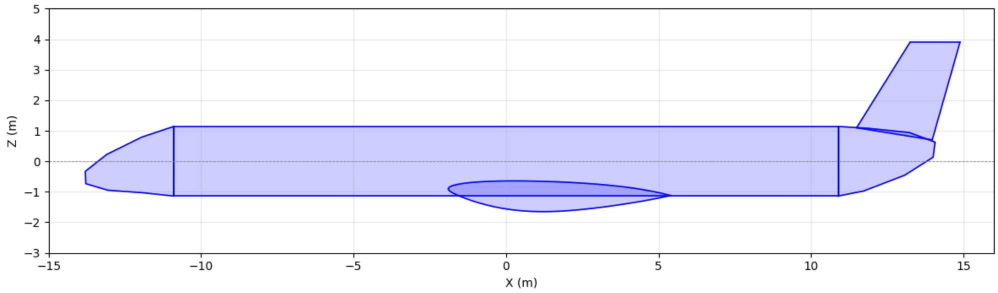

Figure 4.2: EMB-145: Reference side planform

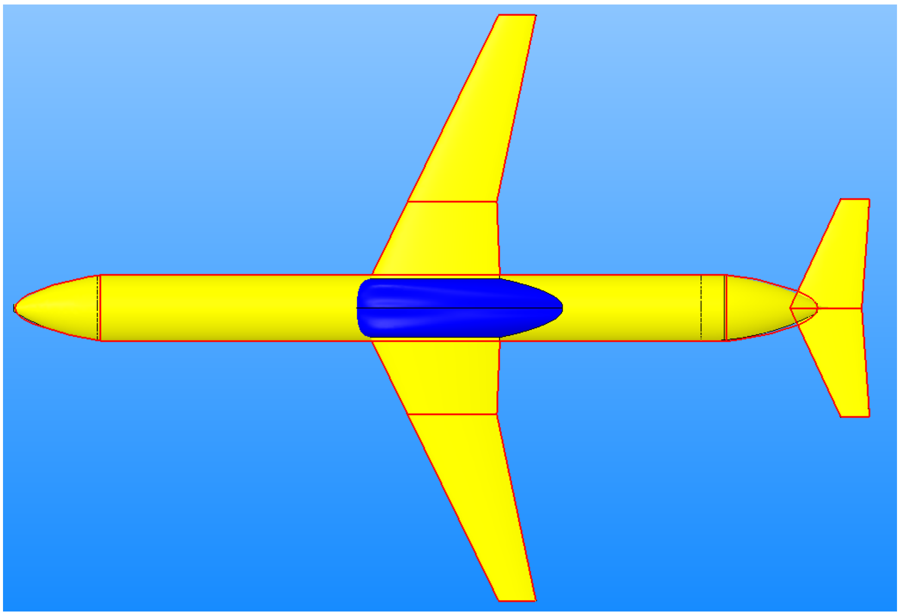

Figure 4.3: EMB-145: Bottom planform validation

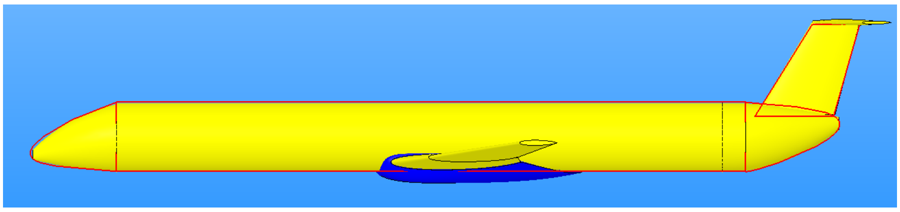

Figure 4.4: EMB-145: Side planform validation

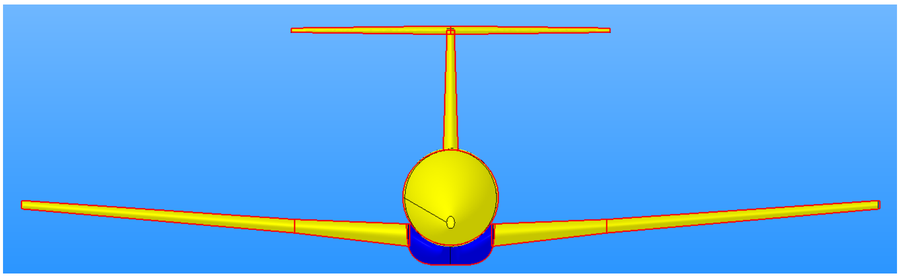

Figure 4.5: EMB-145: Front planform validation

Table 4.1: EMB-145 metrics comparison

Wing	*Reference*	*Model*	*Units*	% *Error*
Root chord	4.86	4.86	m	0.00
Kink chord	3.10	3.10	m	0.00
Tip chord	1.30	1.30	m	0.00
Root thickness	0.95	0.95	m	0.00
Kink thickness	0.32	0.32	m	0.00
Tip thickness	0.30	0.30	m	0.00
Span	20.04	20.04	m	0.00
Sweep	26.00	26.00	deg	0.00
Dihedral	4.45	4.45	deg	0.00
Twist	0.00	0.00	deg	0.00
Total wing area	53.61	53.55	m^2	0.11
Wing volume estimation	12.65	12.95	m^3	2.39
Fuselage				
Width Fuselage	2.28	2.29	m	0.30
Height Fuselage	2.28	2.28	m	0.08
Length Fuselage	27.93	27.96	m	0.10
Eccentricity	0.00	0.07	n/a	0.00
Fineness ratio	12.25	12.25	n/a	0.02
Fairing mean curvature	1.09	1.25	m^{-1}	14.80
Areas				
Top Planform	120.55	120.50	m^2	0.04
Side Planform	64.55	63.78	m^2	1.19
Front Planform	18.46	18.17	m^2	1.58

Table 4.2: Key inputs of the EMB145 validator

Input	Value	Unit
χ	0.1	[-]
τ	0.6	[-]
c_{root}	6.07	m
c_{tip}	1.64	m
h_{min}	1.85	m
Y_i	[0.33, 0.66]	[-]
a_c	[0, 2.65, -0.1, 0.58]	[-]
a_t	[0.25, 1.5, 1, -0.15]	[-]
a_i	[0.0, 0, 0, 0.1]	[-]
a_x	[0, 0.0125, 0.025, 0.25]	[-]
a_z	[-0.565, -0.6125, -0.625, -0.425]	[-]
$a_{U,\text{root}}$	[0.2, 0.18, 0.15, 0.35]	[-]
$a_{L,\text{root}}$	[-0.175, -0.65, -0.35, -0.45]	[-]
a_U	[0.25, 0.25, 0.25, 0.45]	[-]
a_L	[-0.25, -0.25, -0.25, -0.45]	[-]

4.3 A320-200

The Airbus A320-200 is a slightly larger aircraft than the EMB-145, but it has a similar shape in terms of planform. The main difference is that this aircraft has a conventional tail, not a T-tail, and the engines are mounted below the wing.

To achieve the desired fairing size on the A320-200, a hybridization factor of $\chi = 0.11$ was selected based on the front planform. For the fuselage profile, a minimum height of $h_{min} = 3.7m$ and slender factor of $\tau = 0.85$ was used. In reality, the A320-200 has a fuselage height of 4.14m which shows the effect of using the parameterization described through Equation 3.23 and Equation 3.22. This is due to the nature of the hybridization factor linking the fuselage geometry to the wing geometry. The h_{min} input only serves as the absolute minimum height required for the fuselage, the actual height and width are controlled by χ and τ. The designer can easily check the height and width in the ParaPy GUI. The root airfoil of the A320 is significantly thicker at the leading edge than it is on the trailing edge, thus the first value of $a_{\text{U, root}}$ and $a_{\text{L, root}}$ is larger in magnitude in comparison to the subsequent values. The outboard airfoil for both the EMB-145 and A320-200 was selected to be a simple symmetrical airfoil, as this information was not readily available and did not have an affect on the validation results. The chord distribution shape factors, a_c, were selected in the same fashion as the EMB-145 as they have very similar wing shapes. To achieve the vertical position of the fairing, the second value of the a_z factors was set to -0.6, which lowered it the right amount to fit the reference planform, shown in Figure 4.9. To match the shape of the fairing, the second and third shape factors, a_{z2} and a_{z3}, were decreased more than the first and fourth.

The results of the A320-200 metrics comparison show a good agreement between the reference data and the model geometry. Planform characteristics such as span, sweep, and twist reproduce the reference values precisely. The dihedral angle shows only a 1.11% difference, which is likely due to the difference in definition of the root chord location between the model and the reference. The model root chord is slightly lower because it models the fairing, whereas the on the reference it is likely measured from the start of the outboard wing. The wing metrics also align well, with the total wing area within 0.3% of the reference and the estimated wing volume showing a slightly larger deviation of 4.89%. For the fuselage, the width and height are within less than 0.5% error, while the length differs by about 1.62%. The derived geometric properties, such as eccentricity and fineness ratio, remain close to the reference values, with errors below 1.5%. The largest deviation appears in the fairing mean curvature, where the model underestimates the reference by approximately 11.8%. The difference in curvature could be due to a difference in calculation; the references is based from a single curve and the model interpolates specific points from the airfoil profiles. In terms of area comparisons, the model captures the overall planform representations very closely. The top area differs by only 0.14%, the side area by 0.49%, and the front area by 0.73%. These results indicate that the model replicates the A320-200 geometry with high fidelity, only minor discrepancies concentrated in local features such as kink thickness and fairing curvature.

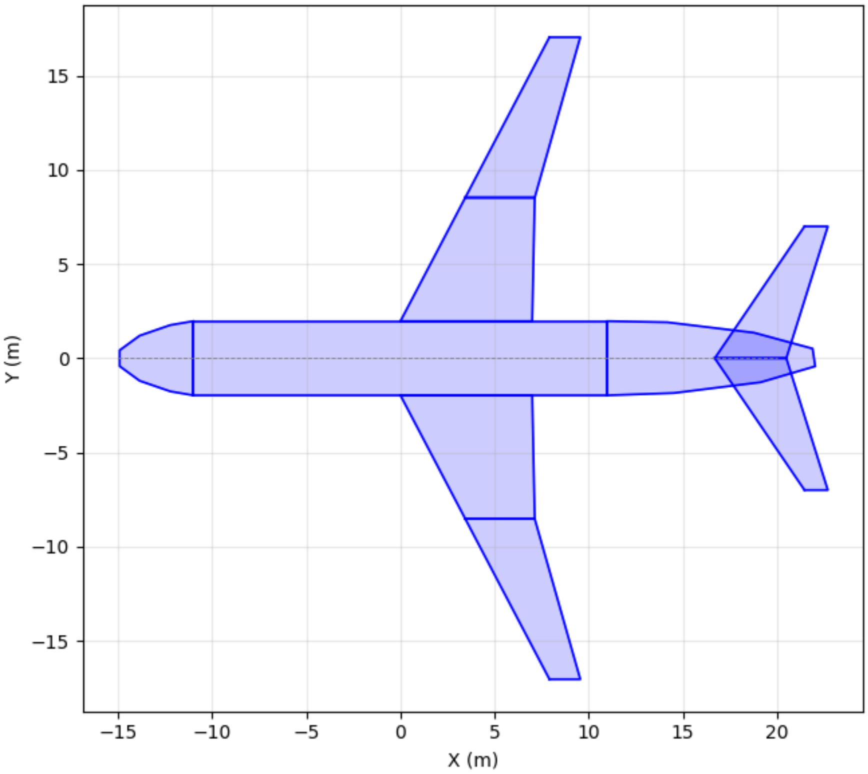

Figure 4.6: A320-200: Reference top planform

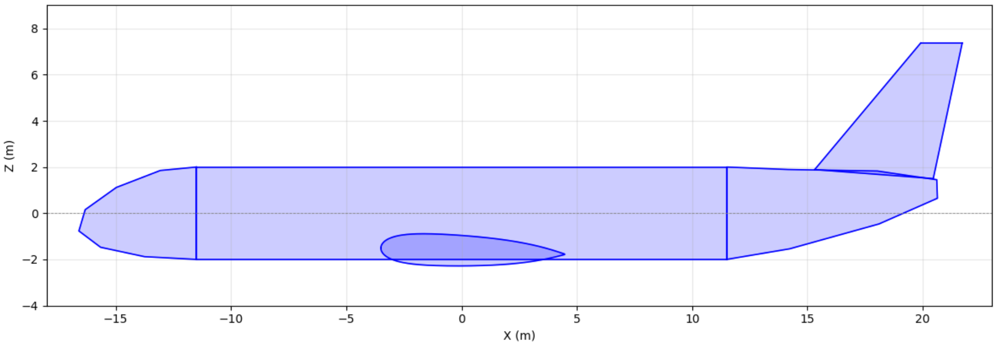

Figure 4.7: A320-200: Reference side planform

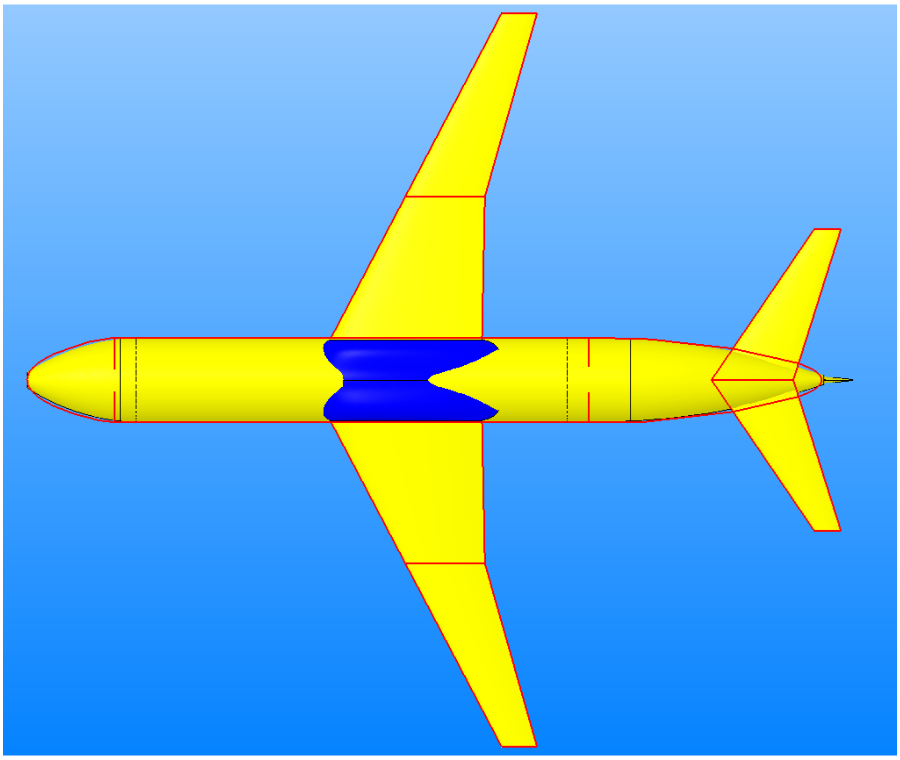

Figure 4.8: A320-200: Bottom planform validation

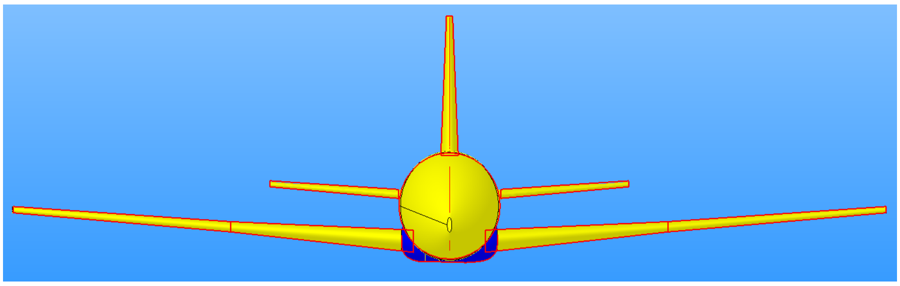

Figure 4.9: A320-200: Front planform validation

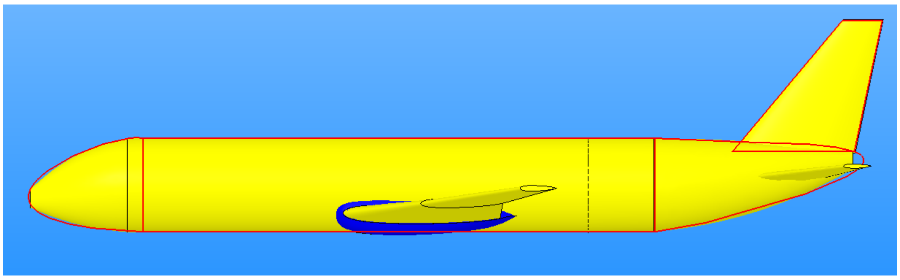

Figure 4.10: A320-200: Side planform validation

Table 4.3: A320-200 metrics comparison

Wing	*Reference*	*Model*	*Units*	% *Error*
Root chord	6.07	6.07	m	0.00
Kink chord	3.69	3.69	m	0.00
Tip chord	1.64	1.64	m	0.00
Root thickness	0.87	0.87	m	0.00
Kink thickness	0.40	0.40	m	0.00
Tip thickness	0.25	0.25	m	0.00
Span	34.09	34.09	m	0.00
Sweep	26.00	26.00	deg	0.00
Dihedral	4.50	4.55	deg	1.11
Twist	0.00	0.00	deg	0.00
Total wing area	90.85	91.13	m^2	0.30
Wing volume estimation	15.86	16.64	m^3	4.89
Fuselage				
Width Fuselage	3.94	3.93	m	-0.38
Height Fuselage	4.14	4.13	m	-0.36
Length Fuselage	37.57	36.96	m	-1.62
Eccentricity	0.31	0.31	n/a	0.18
Fineness ratio	9.07	8.96	n/a	-1.26
Fairing mean curvature	0.94	0.83	m^{-1}	-11.77
Areas				
Top Planform	297.53	297.96	m^2	0.14
Side Planform	150.83	150.09	m^2	0.49
Front Planform	44.92	44.60	m^2	0.73

Table 4.4: Key inputs of the A320-200 validator

Input	Value	Unit
χ	0.11	[-]
τ	0.75	[-]
c_{root}	6.07	m
c_{tip}	1.64	m
h_{min}	3.7	m
Y_i	[0.33, 0.66]	[-]
a_c	[0, 3.25, -0.3, 0.99]	[-]
a_t	[1, 1.65, 2.5, -0.325]	[-]
a_i	[0.0, 0, 0, 0.1]	[-]
a_x	[0, 0.15, 0.25, 0.49]	[-]
a_z	[-0.6, -0.695, -0.6275, -0.625]	[-]
$a_{U,\text{root}}$	[0.33, 0.25, 0.25, 0.45]	[-]
$a_{L,\text{root}}$	[-0.33, -0.25, -0.25, -0.395]	[-]
a_U	[0.25, 0.25, 0.25, 0.45]	[-]
a_L	[-0.25, -0.25, -0.25, -0.45]	[-]

4.4 MIT Aurora D8

The MIT Aurora D8 was selected because it served as a good transition between conventional and BWB configurations. Its fuselage is the shape of an airfoil, but has similar dimensions to that of a classic tube fuselage and the wing is clearly distinguishable from the fuselage. The idea of this aircraft is to be able to increase the aerodynamic efficiency as much as possible, whilst still maintaining the same apron or airport constraints as the current commercial aircraft.

During the validation of this aircraft, there was difficulty in modelling the fuselage. This is because of the unique nature of the fuselage. Initially, the profiles in between the root and the kink section where equally spaced out, which worked well to describe a BWB, but was not sufficient for modelling the D8. So the Y_2 and Y_3 inputs had to be added to adjust this spacing. By doing so, it allowed for the side of the fuselage to be as flat as possible with a very sharp fairing curvature, which represented the wing-body junction more precisely. Due to the nature of the lofting of the fairing, this was not exactly perfect, but it was close enough to match the planform. The most complicated aspect of replicating the D8 was the thickness distribution, as it had to transition from the full thickness of the fuselage to the smaller thickness of the wing, as seen in Figure 4.14. This was achieved by making the third thickness shape factor a_{t3} very large and the second factor a_{t2} had to be made negative to "counteract" this increase and maintain smooth curvature. When coupled with the z-positioning shape factors, this resulted in an almost exact representation of the D8 fuselage. To recreate the correct width of the D8, a hybridization factor of $\chi = 0.1485$ was used. To create the cabin, the minimum height was set to $h_{\text{min}} = 2.8$ with a slender factor of $\tau = -0.5$, so that the fuselage could fit within the fairing.

When looking at the quantitative results, the wing parameters are reproduced exactly, while minor deviations are observed in root and tip thicknesses and wing volume estimation. Fuselage dimensions also agree closely with the reference, with errors under 1% for width, height, and length, and slightly larger differences for eccentricity which was 4.43%. The highest of these errors was the fairing curvature difference of 7.65%. Both the eccentricity and curvature errors are likely due to the fact of the model still having slight issues at the wing-body junction, which can be clearly seen in Figure 4.16. This mainly arises due to the radical change in airfoil size between the fuselage and wing as well as the difference in shape for the upper and lower fuselage surface. To alleviate this, one could add another profile in between this section with new airfoil shape parameters, a_U and a_L, which would allow for much more control. This was not done with the validation at hand because it was important to keep the model the same for all the aircraft, with the only real difference from model to model being the tail plane generation. Planform areas show very small discrepancies, all within 2%, showing that this model is quite robust even with a difficult configurations.

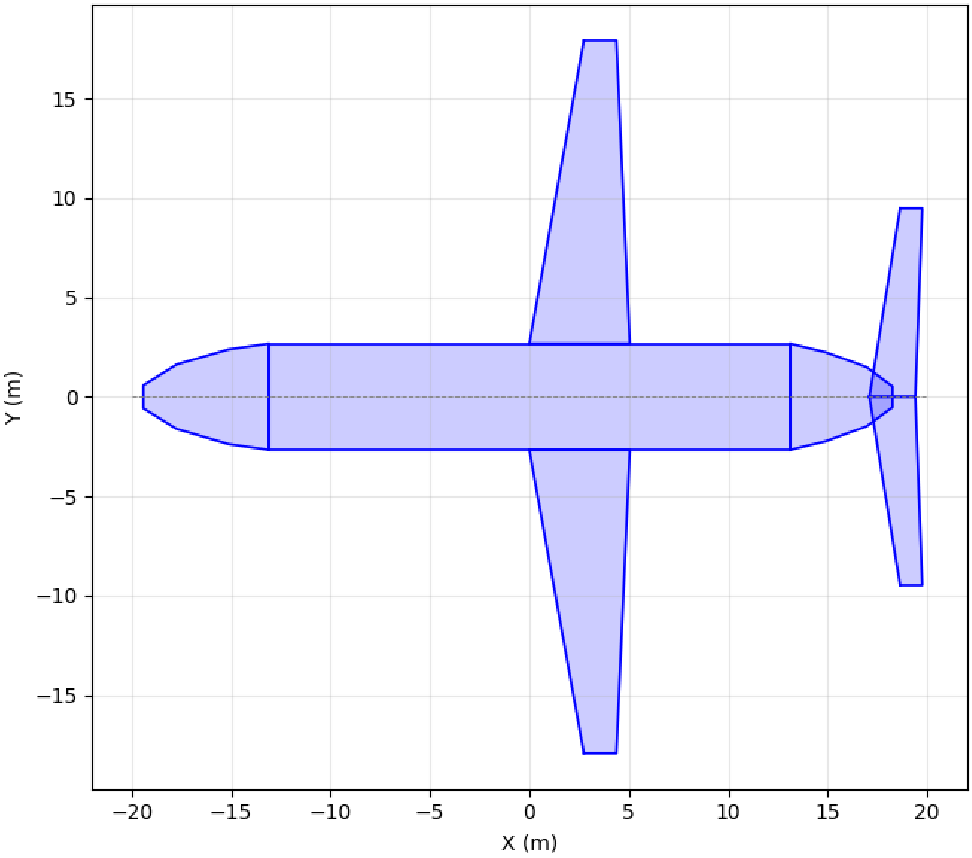

Figure 4.11: D8: Reference top planform

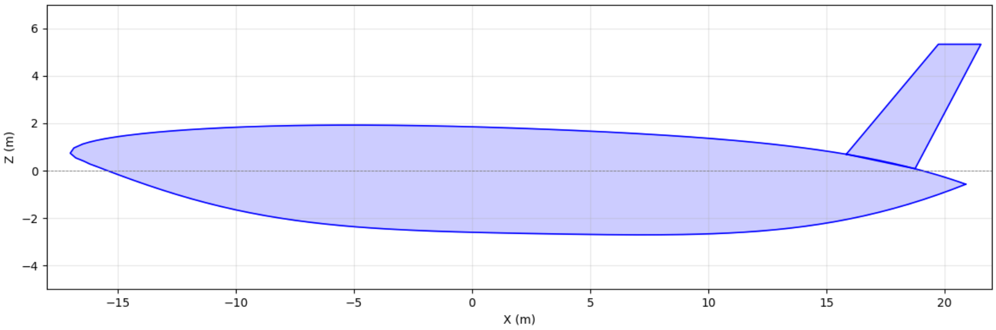

Figure 4.12: D8: Reference side planform

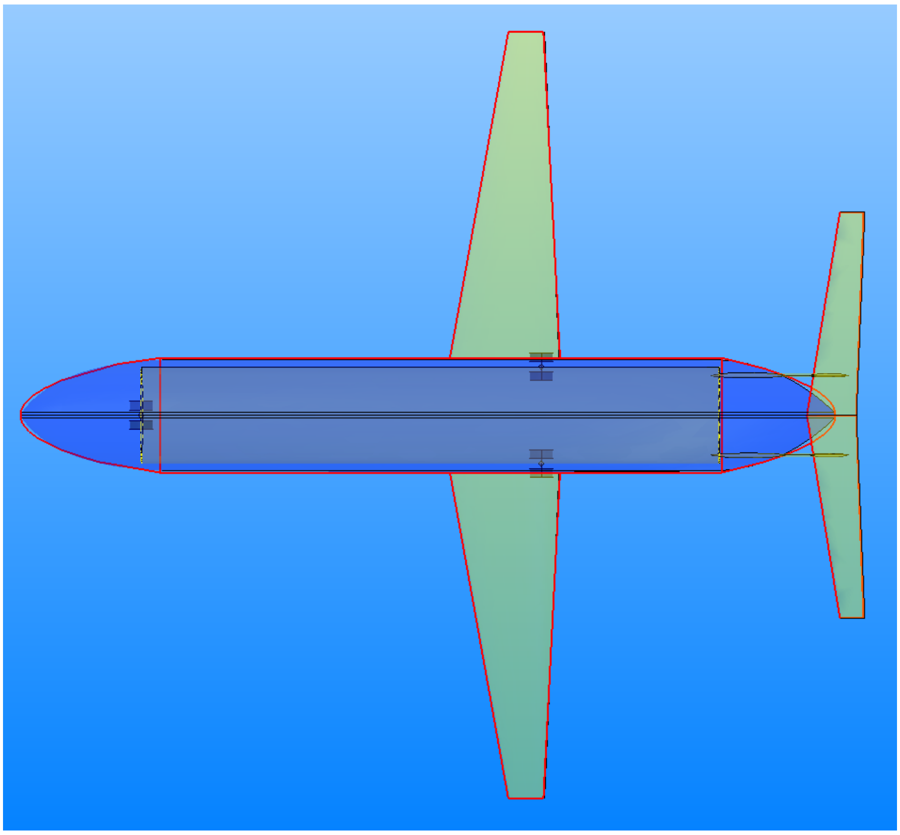

Figure 4.13: D8: Top planform validation

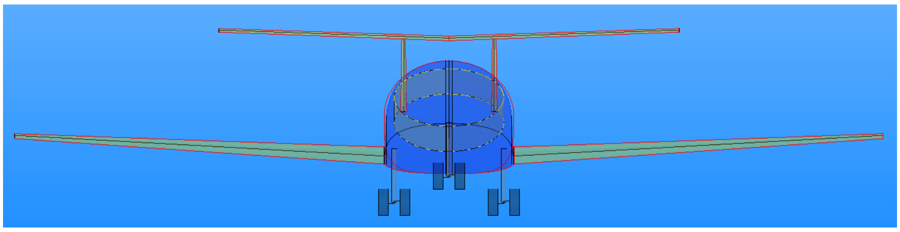

Figure 4.14: D8: Front planform validation

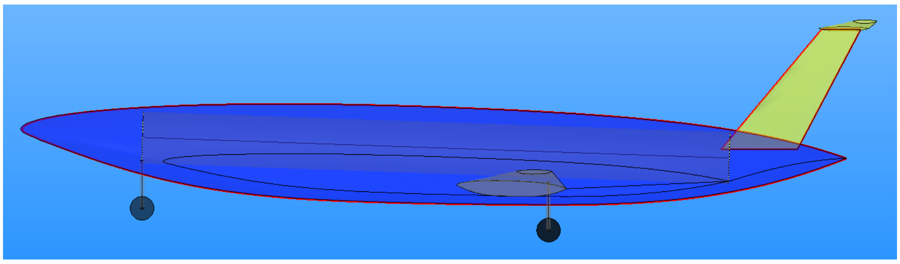

Figure 4.15: D8: Side planform validation

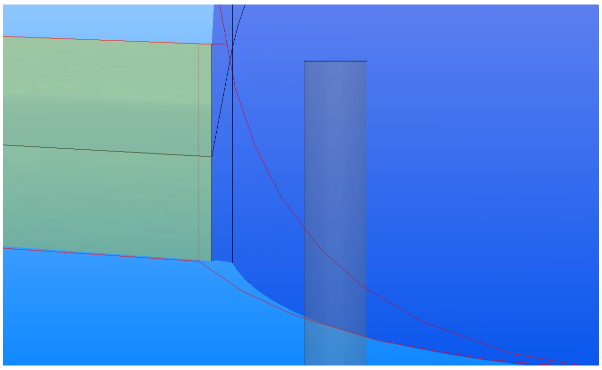

Figure 4.16: D8: Fairing curvature error

Table 4.5: D8 metrics comparison

Wing	*Reference*	*Model*	*Units*	% *Error*
Root chord	5.04	5.04	m	0.00
Kink chord	-	-	m	0.00
Tip chord	1.64	1.64	m	0.00
Root thickness	0.70	0.71	m	1.22
Kink thickness	-	-	m	0.00
Tip thickness	0.19	0.19	m	0.00
Span	35.81	35.81	m	0.00
Sweep	10.15	10.15	deg	0.00
Dihedral	3.00	3.00	deg	0.00
Twist	0.00	0.00	deg	0.00
Total wing area	239.24	239.24	m^2	0.00
Wing volume estimation	68.76	69.50	m^3	1.09
Fuselage				
Width Fuselage	5.35	5.32	m	0.59
Height Fuselage	4.40	4.44	m	0.83
Length Fuselage	38.07	37.98	m	0.25
Eccentricity	0.69	0.66	n/a	4.43
Fineness ratio	8.65	8.56	n/a	1.07
Fairing mean curvature	0.40	0.36	m^{-1}	7.65
Areas				
Top Planform	320.73	320.44	m^2	-0.1
Side Planform	138.54	137.96	m^2	0.42
Front Planform	34.72	35.36	m^2	1.82

Table 4.6: Key inputs of the D8 validator

Input	Value	Unit
χ	0.1485	[-]
τ	-0.5	[-]
c_{root}	37.98	m
c_{tip}	1.64	m
h_{min}	2.8	m
Y_i	[0.33, 0.66]	[-]
a_c	[0, -9, 13, 0.215]	[-]
a_t	[0.455, -7.45, 11.5, 0.15]	[-]
a_i	[2, 2, 2, 2]	[-]
a_x	[-0.29, -0.85, 5.15, 0]	[-]
a_z	[1.68, 1.565, 1.675, 0.3]	[-]
$a_{U,\text{root}}$	[0.1125, 0.125, 0.15, 0.15, 0.2, 0.4]	[-]
$a_{L,\text{root}}$	[-0.075, -0.3, -0.25, -0.15, -0.425, -0.55]	[-]
a_U	[0.1125, 0.125, 0.15, 0.15, 0.2, 0.4]	[-]
a_L	[-0.075, -0.3, -0.25, -0.15, -0.425, -0.55]	[-]

4.5 Delft BWB Concept

The BWB concept presented by Van Dommelen and Vos, is defined by the authors as a "conventional" Blended Wing Body [28]. It is essentially a large wing with winglets, where the center section has increased thickness to have sufficient volume for cargo and passengers. This aircraft will be denoted as the "Delft BWB". The idea for this aircraft is for it to have as "clean" of a wing as possible, so the idea is for the winglets to take care of the directional control and stability, which makes the sizing of them on BWB a key research area.

The airfoils are similar to the Whitcomb supercritical airfoil, which was matched visually using the a_U and a_L coefficients shown in Table 4.8. To get the desired concave shape of the fairing, both on the TE and the LE, one must tweak the a_x and a_c inputs to do so. The wing sweep input dictates the general position of the outboard wing, but to get a more refined shape, the specific sections have to be transformed, which is why these inputs were introduced. To match the size of the fuselage, a hybridization factor of $\chi = \mathbf{0.4565}$ was used. This perfectly aligned the kink location with the reference planform. To fit the cabin inside the aircraft, a slender factor of $\tau = \mathbf{-3}$ was used to get the right shape for the given minimum height of $\mathbf{h_{min}} = \mathbf{6m}$. One significant issue with this validation was the fact that the planform had straight edges and clear kinks, making it difficult to get an exact representation. The curvature was approximated by setting the second chord shape factor, a_{c2}, to be very positive and the third chord shape factor, a_{c3}, to be negative, to get a sharper nose and faster reduction in curvature on the trailing edge Figure 4.19.

When comparing the metrics of the Delft BWB, the largest deviations are observed in the root thickness at 3.44% and wing volume at 2.98% percent. Fuselage parameters also match closely, with deviations below 1.2% for width, height, length, eccentricity, and fineness ratio. The fairing mean curvature shows a slightly higher discrepancy of 7.38%, which could be due to the same reasons as presented for the D8; a limited amount of profiles. Another reason arises from the fact that the reference front planform essentially uses straight lines which means the reference curvature had to be approximated. The planform areas in Table 4.7 exhibit very small differences, all below 1 percent, confirming that the model accurately captures the reference geometry.

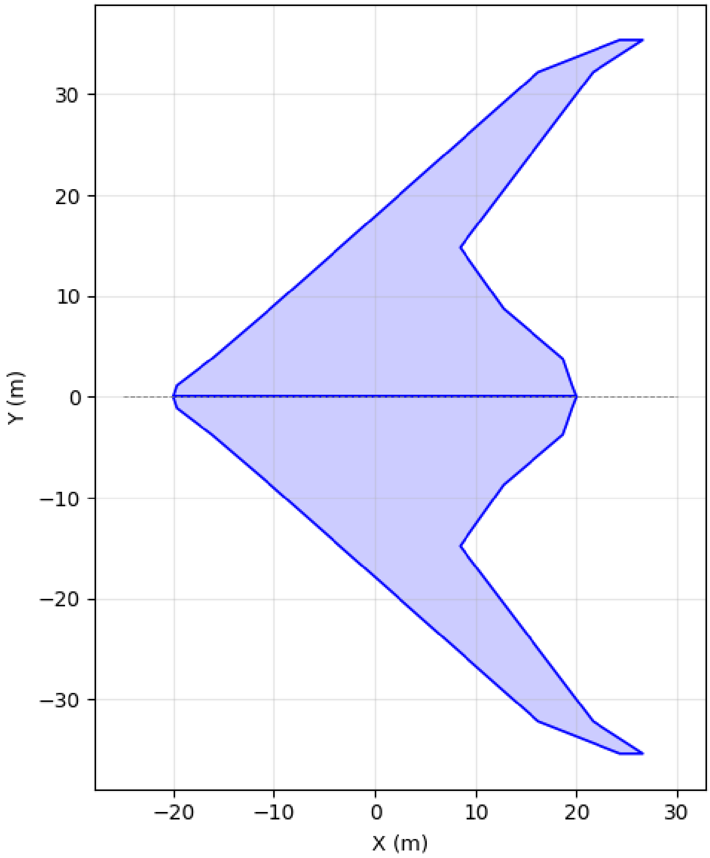

Figure 4.17: Delft BWB: Reference top planform

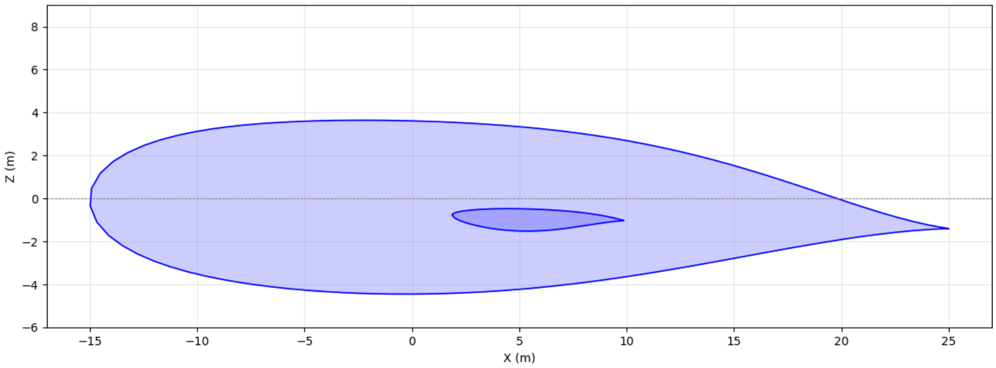

Figure 4.18: Delft BWB: Reference side planform

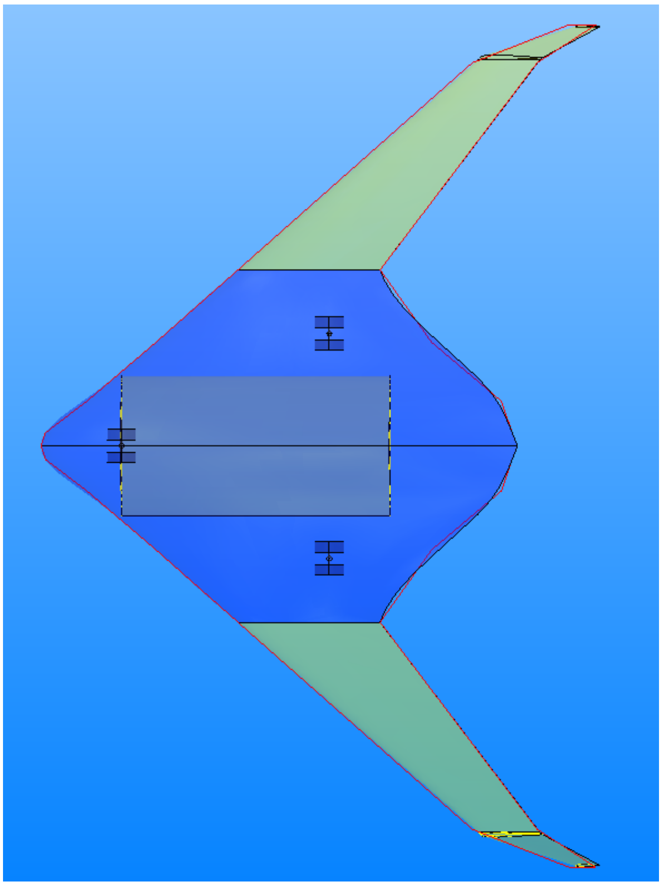

Figure 4.19: Delft BWB: Top planform validation

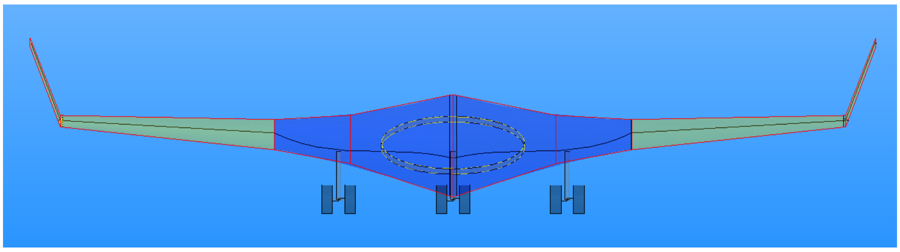

Figure 4.20: Delft BWB: Front planform validation

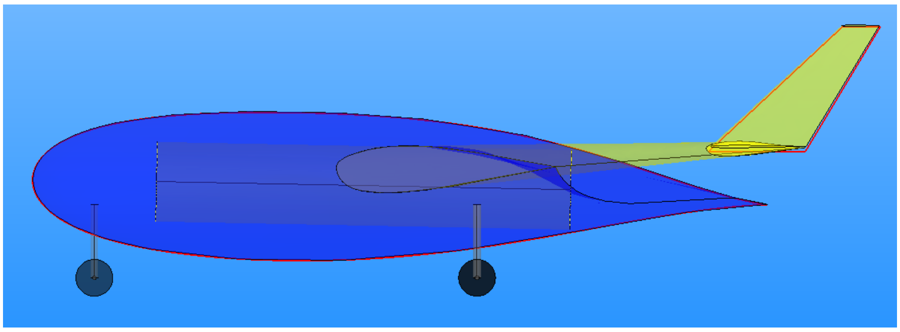

Figure 4.21: Delft BWB: Side planform validation

Table 4.7: Delft BWB metrics comparison

Wing	*Reference*	*Model*	*Units*	% *Error*
Root chord	40.00	40.00	m	0.00
Kink chord	11.94	11.92	m	0.14
Tip chord	5.27	5.27	m	0.00
Root thickness	8.50	8.21	m	3.44
Kink thickness	2.45	2.43	m	0.71
Tip thickness	0.96	0.96	m	0.00
Span	65.00	65.00	m	0.00
Sweep	48.50	48.50	deg	0.00
Dihedral	3.60	3.60	deg	0.00
Twist	0.00	0.00	deg	0.00
Total wing area	1487.55	1487.57	m^2	0.02
Wing volume estimation	3034.09	2943.74	m^3	2.98
Fuselage				
Width Fuselage	14.94	14.79	m	1.01
Height Fuselage	8.30	8.21	m	1.11
Length Fuselage	40.00	40.00	m	0.00
Eccentricity	1.50	1.50	n/a	0.14
Fineness ratio	4.82	4.87	n/a	1.12
Fairing mean curvature	0.020	0.022	m^{-1}	7.38
Areas				
Top Planform	1080.43	1085.10	m^2	0.43
Side Planform	229.06	228.61	m^2	0.20
Front Planform	351.17	347.92	m^2	0.93

Table 4.8: Key inputs of the DelftBWB validator

Input	**Value**	**Unit**
χ	0.4565	[-]
τ	-3	[-]
c_{root}	40	m
c_{tip}	5.2	m
h_{min}	6	m
Y_i	[0.25, 0.5, 0.75]	[-]
a_c	[-0.015, 11.125, -1.45, 1.55]	[-]
a_t	[15.75, 8, 5.85, 2.85]	[-]
a_i	[0.0, 4.5, 5.5, 0.01]	[-]
a_x	[0.015, 2.75, -0.675, -0.1]	[-]
a_z	[0.01, 0.25, 0.2, -0.05]	[-]
$a_{U,\text{root}}$	[0.2, 0.175, 0.175, 0.2, 0.3, 0.075]	[-]
$a_{L,\text{root}}$	[-0.2, -0.175, -0.175, -0.2, -0.15, -0.05]	[-]
a_U	[0.2, 0.25, 0.25, 0.25, 0.125, 0.25]	[-]
a_L	[-0.425, -0.25, -0.29, -0.265, -0.125, -0.25]	[-]

4.6 Validation Summary

From these results, it can be concluded that the model has the ability to model existing aircraft geometries to a high degree of accuracy. All the aircraft had areas and volumes within ±3% and ±5% respectively. At this level of the design stage, this level of precision satisfies the requirements for means of compliance, as the results demonstrate consistent geometric and aerodynamic fidelity relative to known aircraft data. Minor deviations were mainly observed near the fuselage–wing junction and tail regions, where curvature transitions are highly sensitive to parameterization. This validation establishes confidence in the framework's ability to represent both conventional and blended-wing configurations accurately enough to support future optimization and design exploration activities.

Chapter 5

Design Study

This chapter outlines how the hybridization factor and newly introduced parameterization can be used to optimize a conceptual hydrogen-powered BWB aircraft design. This will be done by hand and will serve as an example of how it can be applied to higher fidelity optimization. The BWB design will be based off of the top-level aircraft requirements of the Airbus A320-200.

5.1 Design Objective

The main objective of this task is to use the novel parameterization to increase the aerodynamic efficiency and stability of a short-range, hydrogen-powered BWB without compromising the volume requirements. First, an A320-200 model will be generated and tested using the same CFD procedure that will be used for the BWB configurations. This will give a reference value so that accurate comparisons can be made. Then, a BWB model will be generated based off of the initial A320-200 geometry using the steps outlined in subsection 3.5.2, with an initial assumption for the hybridization factor. With this geometry, a simple sensitivity analysis will be performed to see how the aerodynamic performance varies with the hybridization factor. Using the results from this analysis, 4 configurations with different hybridization will be selected. Each configuration will be designed such that there is sufficient volume for the fuselage and fuel tanks. For each of these configurations, wing parameters like sweep, dihedral and taper ratio will be varied to see how sensitive different χ configurations are to a change in parameter. Using these results, a selection of parameters will be made such that it has the best aerodynamic improvement from the A320-200 baseline and adequately meets the mission requirements. Once this design choice has been made, the utility of the shape factors will be explored, specifically looking at how they relate to the frontal fairing curvature and how that curvature affects the pressure distribution. The adjustments shape factors will be done until improvements in the aerodynamic efficiency has been realized. This design routine will be possible due to the integration of FlightStream within ParaPy, as it allows for a change in geometry to be meshed and analyzed quickly. This enables for many designs to be tested in a short time frame with a medium-fidelity software.

5.2 Top Level Requirements

The aircraft requirements for the HBWB design will be based on the Airbus A320-200F, a freighter version of the A320-200. This is chosen due to the commercial success of the A320 for both passenger and cargo applications [65]. The choice of cargo aircraft is made as it is the most realistic option where a BWB can begin operating in the near future based on the advantages and disadvantages discussed in subsection 1.2.2. The aircraft will fly at around Mach 0.78 at FL30 (30,000ft) which is a common cruise speed and altitude for the A320. The aircraft will share the same payload weight and volume as the A320, which is 19000kg and 160m^3 respectively. As the aircraft needs to be an evolutionary design fit to comply to the emission requirements of the future, the fuel source will be selected to be hydrogen. This means that the required fuel weight will be much lower, however the weight of the fuel system and components will be much greater. This will be more carefully analyzed in section 5.4. The range of the aircraft will not be exactly the same as A320-200 as we are assuming hydrogen as the fuel source, which means the aircraft has a much larger operating empty weight due the heavier fuel systems. The A320 boasts a range of around 6500km, but in 2019, 90% of its missions were shorter than 3180km [66]. This means that we can select a lower maximum range for the BWB configuration to improve efficiency and to keep similar weight characteristics as the baseline A320. This analysis was performed in [66] and found that an LH2 equivalent A320 would have a range of 3400km for a gravimetric index of 0.35. Other top level aircraft requirements were based off of the typical requirements for a CS/FAR-25 propeller aircraft. The airport was chosen to be Schiphol airport, as information for this was readily available [58]. Using the requirements outlined in CS/FAR 25.119, the climb characteristics were defined. The landing and approach parameters were calculated based off of the selected aircraft geometry using the equations found in [58]. The approach speed was found by calculating the stall speed, $V_{\text{app}} = 1.23V_{\text{stall}}$. V_{stall} was calculated using the $C_{\text{L,max}}$ found through the preliminary simulations in section 5.6. It is important to note the high mass fraction of 0.95 for approach and landing. This is due to the high energy density of hydrogen, meaning the fuel mass fraction is much lower for hydrogen fuel-cell powered aircraft.

All of the airfoils were selected to be supercritical as these are considered to be the most efficient in high-subsonic flight regime and commonly found on transport aircraft[36]. The root used a NASA SC(2)-0518 airfoil that had its cambered removed. The 18% maximum thickness-to-chord ensures sufficient volume in the center section, which meets the requirement set by Liebeck et al. of 17% [7]. The airfoil at the kink section is the same NASA SC(2)-0518 airfoil but keeping the camber. The 05 designation indicates the lift coefficient that this airfoil is designed to fly at, which is 0.5. This value was deemed acceptable as it is common for commercial airliners; the Airbus A320-200 has a lift coefficient of around 0.44 at its max speed [67]. The airfoil used for the tip will be the NASA SC(2)-0410, which is of the same family but has a smaller thickness-to-chord ratio and camber, designed to fly at a slightly lower lift coefficient of 0.4. This was chosen in an attempt to reduce the lift-induced drag that arises from the wing-tip vortices, as a higher lift means a greater pressure difference and thus stronger vortices. Winglets will also be added to both the baseline TAW configuration as well as the HBWB, as they also offer improved aerodynamic efficiency from both the reduction in lift induced drag and increase in effective span. The winglet airfoil will be a thinner, symmetrical one of the same family, the NASA SC(2)-0010. The initial leading-edge sweep angle for the outboard wing was chosen to be 40° to allow for better longitudinal stability characteristics, it is similar to that of the Delft BWB concept in section 4.5. The initial dihedral will be 5° which is close to that of the A320-200 [67].

The fuselage dimensions are determined based off of the hybridization factor, required volume and minimum height. Once the internal fuselage is established, the chord is increased until the centerbody airfoil has the adequate thickness to enclose the fuselage. For the A320-200 fuselage requirements and a hybridization factor of $\chi = 0.45$, the root chord length was deemed to be 25m, which will be used as the initial baseline. The tip chord was selected to be 3m, based on a taper ratio of 0.45 and an aspect ratio of around 5. The overall planform of the geometry will be similar to that of the Dzyne Ascent 1000 and the BWB presented by Lyu et al., shown in Figure 2.10.

Table 5.1: Flight Phase and Performance Parameters

Parameter	Value
Take-off	
Take-off distance	1900 m
Runway surface type*	asphalt/tarmac
Airport altitude	500 m
Airport temperature	298 K
Mass fraction take-off	1 -
Climb	
Minimum climb rate required	0.5 m/s
Altitude for climb performance	9144 m
Temperature	229 K
Mass fraction climb	0.98 -
Climb Gradient	3.2 %
Cruise	
Cruise speed required	0.78 Mach
Cruise altitude	9144 m
Speed of sound at cruise altitude	303 m/s
Temperature	229 K
Mass fraction cruise	0.95 -
Landing	
Landing field length	1600 m
Runway condition	dry
Runway surface type*	asphalt/tarmac
Airport altitude	500 m
Airport temperature	288.15 K
Mass fraction landing	0.95 -
Loiter time	45 min
Diversion range	250 km
Approach	
Altitude for approach speed	0 m
Mass fraction approach speed	0.93 -
Temperature	288.15 K
Approach speed	70 m/s

Table 5.2: Initial Geometry

Wing Geometry	
Span	34 m
Root chord	25 m
Kink chord	6.6 m
Tip chord	3 m
Twist	-1
Dihedral	5°
Sweep	40°
Root airfoil	NASA SC(2)-0518*
Kink airfoil	NASA SC(2)-0518
Tip airfoil	NASA SC(2)-0410
Fuselage Geometry	
Min. Height	2 m
Volume	160 m^3
Winglet	
Winglet span	0.8 m
Winglet tip chord	0.5 m
Winglet sweep	30°
Winglet cant angle	80°
Winglet airfoil	NASA SC(2)-0010
Cargo	
MTOM	73300 kg
Payload volume	160 m^3
Tank volume	60 m^3
Range	
Range	3400 km

5.3 Simulation Setup and Mesh Convergence

The flow solver selected for flightstream was chosen to be a subsonic Prandtl-Glauert solver, as the aircraft aims to fly at $M = 0.78$ which is within the acceptable range for this solver. This applies corrections to the incompressible solution so that certain compressible effects can be included. Another solver option relevant to this flight regime would be the transonic field panel model as this has certain capabilities in shock prediction, but this required significantly more computational time, which was not beneficial as the goal was to be able to test many configurations within a reasonable amount of time. The downside to using the subsonic solver is that shocks cannot be modelled. This is a significant flow phenomena that would certainly need to be addressed in future work. Even though this is a vortex panel method, viscous effects can still be modelled through the implementation of the viscous coupling within FlightStream. This works by making an initial inviscid linear calculation and then performing a second run with the boundary layer coupled with the flow solution to achieve the non-linear viscous boundary layer de-cambering effects.

Before running simulations on FlightStream, one must first complete a mesh convergence study. This is a mesh refinement process that consists of gradually improving the mesh quality in the U and V (chordwise and spanwise) until the resultant forces are within 1% of the previous result. This is an important part of the CFD analysis as CCS meshing is not done by hand and relies on the user to input adequate mesh densities and distributions that are tailored to the model. Table 5.3 shows the parameters selected to achieve the desired distributions. The growth type of dual-sided successive allows for the leading and trailing edge to be much more dense with respect with respect to the rest of the component. Periodicity describes how much the mesh needs to be repeated, in the case of a wing, we need the upper and lower surface, thus it needs to be set to 2. FlightStream can also select these parameters automatically depending on the type of component (lifting or non-lifting). As the spanwise direction is not as important to capture the necessary flow phenomena, it was set to automatic. The chordwise distribution was kept the same for all the components because this produced the smoothest between them. A change in the chordwise distribution would mean that the components would have to be united using OpenVSP's mesh unite feature, which can produce some skewed cells and cause problems with convergence. Small discontinuities in the coefficient of pressure due to the mesh uniting can be seen at the wing-body and tail-body junction in Figure 5.2b. The spanwise density of the components were selected based off of the sensitivity analysis and to get similar aspect ratio across the entire mesh.

Table 5.3: Meshing parameters found after mesh convergence study for BWB configurations

Mesh parameter	**Number of sections**	**Growth type**	**Growth rate**	**Periodicity**
Fairing Chordwise	100	Dual-sided Successive	1.1	2
Fairing Spanwise	110	Auto	Auto	Auto
Wing Chordwise	100	Dual-sided Successive	1.1	2
Wing Spanwise	80	Auto	Auto	Auto
Winglet Chordwise	100	Dual-sided Successive	1.1	2
Winglet Spanwise	50	Auto	Auto	Auto

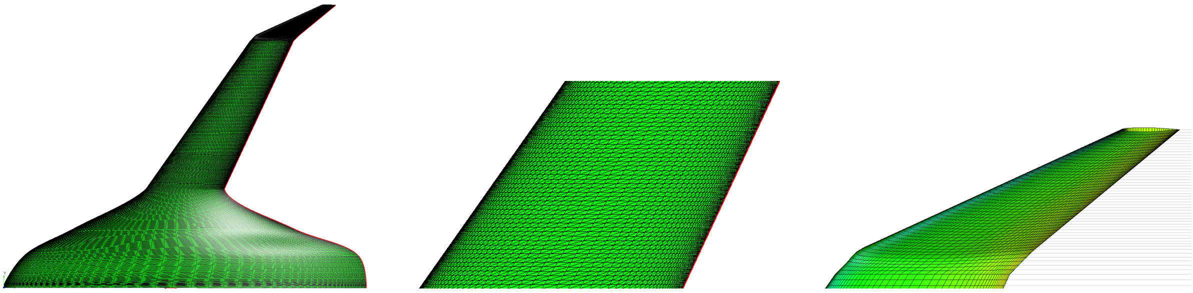
(a) Top view **(b)** Wing mesh **(c)** Winglet mesh

Figure 5.1: Mesh visualizations of top, tail, and wing configurations.

For the A320-200 model, the wing, fuselage and tail are united using OpenVSP's Mesh Unite procedure, which stitches the cells together. Its quality is highly dependent on the number of sections selected and the ratio between the sections. If there is a large difference between the cell sizes, the cells can become highly skewed and the solver is likely to produce erroneous results or not converge. To alleviate this, small tweaks to the mesh density were made by observing this junction.

5.4 Weight estimation

As specific structural components, like ribs and spars, are not modelled directly in the application, the individual weights and density of the components are an input to the application. The effective density of the wing-body structure is calculated using the structural weight of the A320 and then dividing it by the total volume. The structural weight was determined by subtracting the total weight of the propulsion system, empty fuel tank weight and landing gear weight from the operating empty weight [67]. This weight was calculated to be 30t and the volume was found to be around 314m^3 through the validation model created in section 4.3. With this we can create an "effective" structural density, which treats the structure and materials of empty wing and fuselage as a conglomerate. Multiplying this structural density with the volume attribute of the wing-body structure will give a rough estimate of the weight for any of the configurations. This means that there will be slight deviations in the wing structure weight as χ is varied. The weight of the payload will be fixed as the typical maximum payload of the A320-200, which is around 19000kg. This is a very rough estimate and it assumes that the structural requirements would be the same for all configurations which is not true, as they will have different wing bending characteristics. However, as we are not focusing on the specific structural requirements, this will be sufficient for this level of analysis.

The weight of the fuel is converted from kerosene to hydrogen and is made based on the assumption that the engines will combust hydrogen, implying the use of future engine technologies [66]. This conversion was performed by Mukhopadhaya et al.[66] and their A320-equivalent aircraft had a LH_2 weight of $5000kg$. Their aircraft was very similar in terms of MTOM, however the maximum range was 33% lower due to the lower gravimetric index of a hydrogen-based fuel system [66].Gravimetric index is defined as the mass of the fuel divided by the sum of the fuel and fuel systems. The tank weight mass-fraction assumption is made based on an optimized lightweight tank design in

ParaPy automatically returns the CG of solid objects by finding their volume centroid, assuming constant density. Whenever weights are assigned to each component, the weighted sum of each center of gravity is calculated to return the x,y and z coordinates of the overall center of gravity, as described in subsection 3.3.1. This simple assumption does introduce large uncertainty, but we are more interested in how the CG moves for different configurations, rather than knowing the exact position, so this is deemed acceptable for this level of analysis.

Component	**Weight [kg]**	**Mass Fraction**
Wing Structure	40315	0.550
Payload	19000	0.259
Tank + Systems	5485	0.075
Fuel (LH_2)	5000	0.068
Engines + Systems	3500	0.048
MTOM	73300	1.000

Table 5.4: Mass breakdown for an A320-class hydrogen BWB with 5000 kg LH_2 and structural mass fraction of 0.55.

5.5 Baseline analysis: A320-200

Before being able to compare the efficiency of the new BWB designs. We need to conduct a baseline analysis on the reference aircraft, using the same model, solver and procedure to get an accurate representation. The model used was the same as the one in the A320-200 validation section, section 4.3, with the addition of winglets. The winglet geometry is outlined in Table 5.2. From the CFD analysis, the static longitudinal stability, lateral-roll stability and lateral-yaw stability coefficients will be extracted to get a general grasp of what is expected from the BWB. Although, modern flying wing and BWB concepts are sometimes designed without being statically stable, relying on automatic controls for stability. However, as we are trying to emulate the same requirements on the BWB configuration, it is important to keep these values in consideration. The C_L/C_D from the results was 18.07, which is expected to be higher than the reference in cruise as this is a clean wing without any engines. From [68] the cruise C_L/C_D of their reference A320 is around 16. The reference point for the stability derivatives was selected to be at 30% of the mean aerodynamic chord. The residuals of the simulation are shown in Figure 5.3, to show how convergence was achieved for a value of 0.0001. There are two peaks towards the end of the simulation that indicate the recalculation for the stability coefficients and viscous effects, this is normal and expected from this method. The smooth line between 50 and 200 iterations indicates that the first calculation converges well as there is no significant fluctuations.

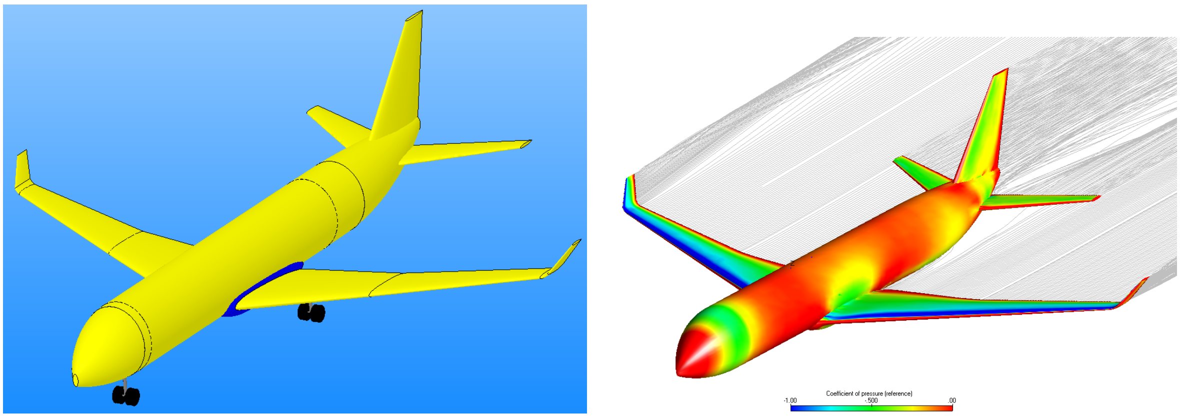

(a) A320-200 model from validation with winglets

(b) Coefficient of pressure distribution over aircraft

Figure 5.2: Analysis on Airbus A320-200 geometry

Performance Parameter	**Symbol**	**Value**
Lift-to-drag ratio	C_L/C_D	18.07
Longitudinal stability derivative	C_{M_α}	-0.0167
Lateral-Roll stability derivative	C_{l_β}	-0.0169
Lateral-Yaw stability derivative	C_{n_β}	0.0183

Table 5.5: Performance parameter results for the clean A320-200 validation model

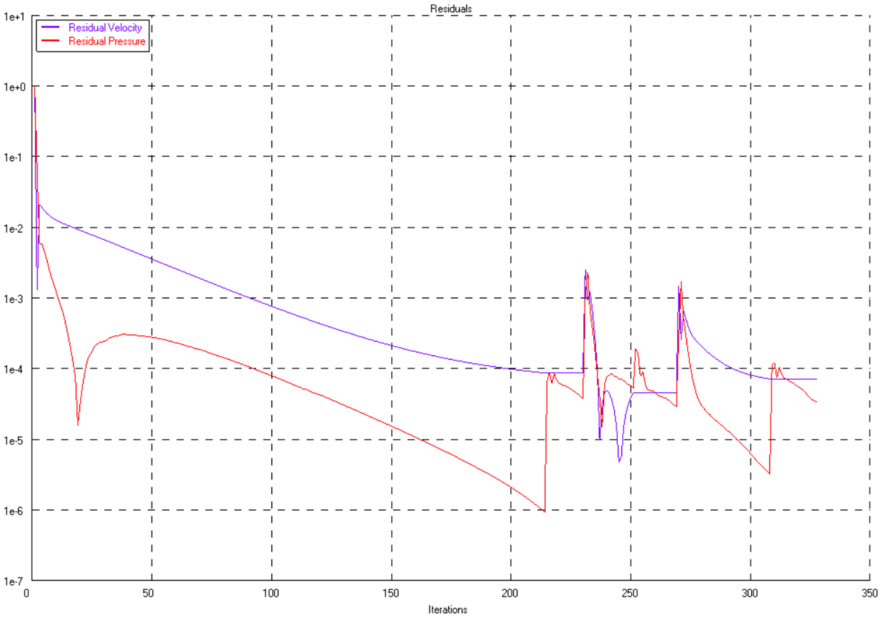

Figure 5.3: Residuals of A320-200 Flightstream simulation

5.6 Sensitivity of the hybridization factor

To quantify the effect of the hybridization factor on the baseline geometry, we need to first make a brief sensitivity analysis. This way we can see what are the changes in aerodynamics and volume requirements whenever there is a change in hybridization factor, χ. To do this we will first take the initial geometry in Table 5.2 and keep everything fixed except for the hybridization factor. The root chord length of the center-body and the thickness distribution is kept constant for this analysis, which is why the volume and wing area will increase linearly with the hybridization factor. By doing this, the fairing volume will increase whilst reducing the outboard wing span, affecting the aerodynamic efficiency of the aircraft. This will not cover all of the effects caused by varying the hybridization factor but it will give some initial insight on finding the right balance between performance and payload volume. This will also give an initial insight into how the stability of the aircraft is affected by the hybridization factor. The ranges for the χ will remain between 0.3 and 0.6 as the resulting geometry from these values is more likely to fall under the classical "BWB" category. The hybridization factor will be increased by 0.05 increments. When the hybridization factor was varied, little changes to the shape factor were needed, only requiring a small tweak of the outboard thickness and x-positioning shape factors, a_{t3} and a_{x3}, when increasing beyond $\chi = 0.5$. This shows that the curvature distribution stays proportionate as χ is varied for the same configuration.

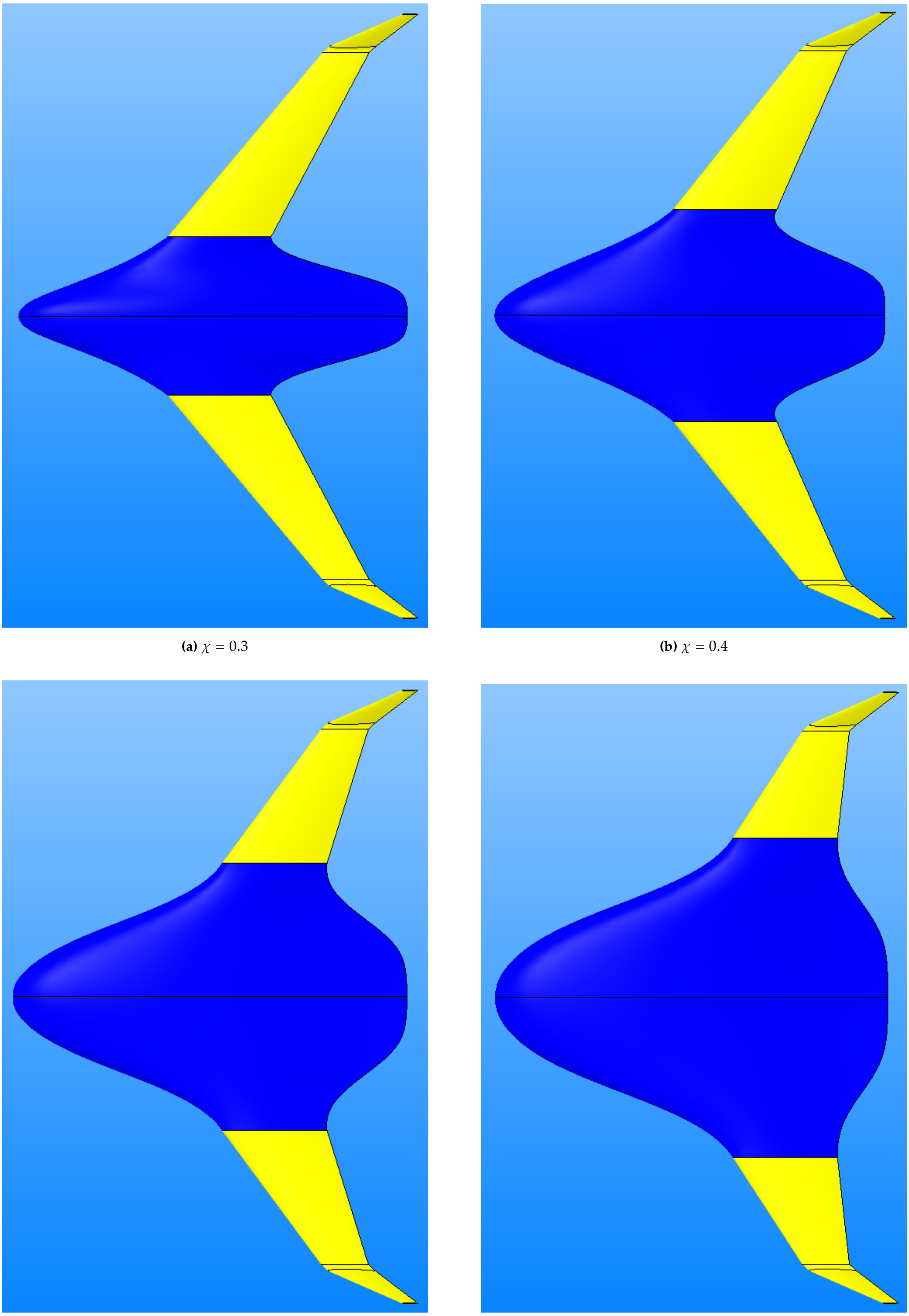

(a) χ = 0.3

(b) χ = 0.4

(c) χ = 0.5

(d) χ = 0.6

Figure 5.4: Effect of χ on top-planform geometry.

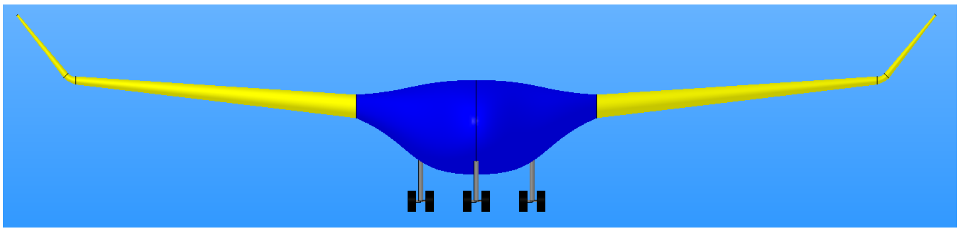

(a) $\chi = 0.3$

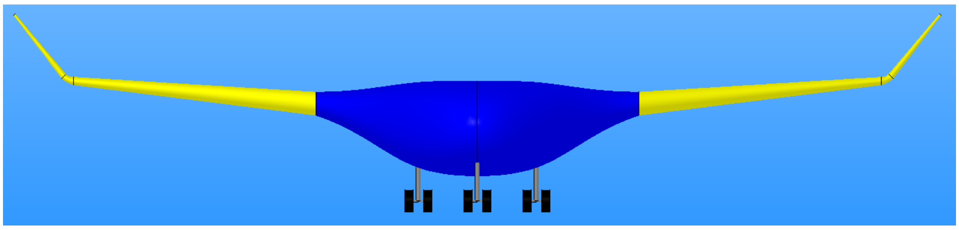

(b) $\chi = 0.4$

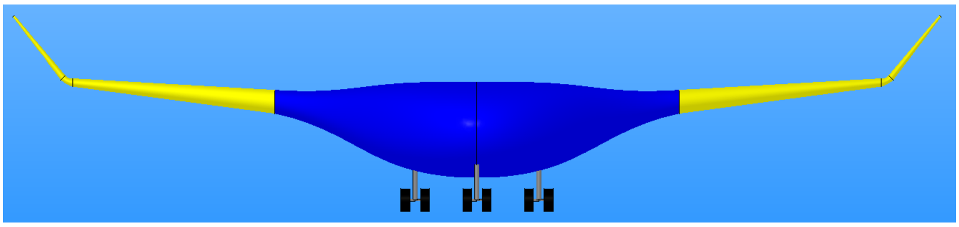

(c) $\chi = 0.5$

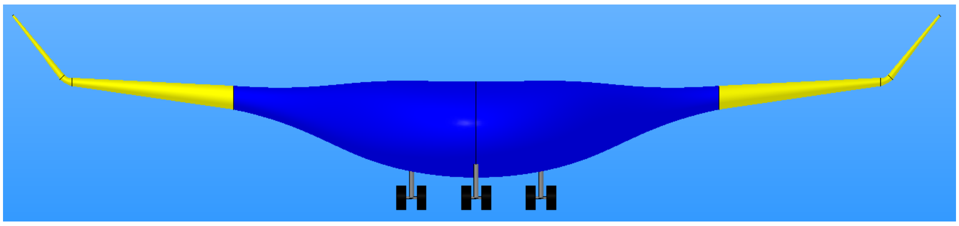

(d) $\chi = 0.6$

Figure 5.5: Effect of χ on front planform geometry.

The volume and aerodynamic efficiency are plotted versus χ at cruise conditions, which is stated above in Table 5.1 as being $M = 0.78$ at FL250 or around $9144m$. The angle of attack to acheive an approximate value of $C_{L,cruise} = 0.45$ was selected to be $\alpha = 2$. This is a common value for commercial aircraft and is also on the lower end of the range, which should be beneficial to improve aerodynamic efficiency as it can reduce the pressured drag.

From Figure 5.6, it can be seen the aircraft is most efficient at $\chi = 0.3$. Lower values of χ exhibited higher C_L. This was quite surprising because lower χ values had a smaller surface area and generated less overall lift. The main reason is that the fairing section is less aerodynamically efficient than the wing section. As it has a greater reference area than the outboard wing, it produces more lift but this in turn produces more lift-induced drag. The lift-induced drag, for a given lift coefficient, is also greater for the fairing section due to its lower aspect ratio with respect to the wing. The lift-induced drag is calculated using Equation 5.2. The skin-friction drag is also always greater for the fairing as it has a larger wetted area to reference area ratio. So the fairing is always less efficient than the wing section, meaning that larger hybridization factors with larger fairing sections will reduce the aircraft's total aerodynamic efficiency.

When χ increased, ratio between the aircraft's wetted area and top-planform reference area, $S_{\text{wet}}/S_{\text{ref}}$ increases, increasing $C_{D,0}$. To better understand this, we can look at the subsonic skin friction drag coefficient equation for a single component from Raymer [16]:

$$C_{D,0} = \frac{C_f \cdot FF \cdot Q \cdot S_{\text{wet}}}{S_{\text{ref}}} \tag{5.1}$$

where C_f is the friction coefficient, FF is the form factor and Q is the interference factor.

However the key driver to the decrease in efficiency is the drop in C_L. One reason for this phenomena is that the center airfoil is uncambered, however the outboard wing airfoil is cambered. As the outboard wing is larger for lower χ values, this means that a larger portion of the BWB has a cambered airfoil and thus generates a greater overall C_L for the aircraft at the same angle of attack. If we imagine the BWB as a normal wing, by increasing the hybridization factor we are decreasing the overall camber of the wing. However, this effect was not as strong as the change in fairing size, as this was tested by using uncambered airfoils for the whole aircraft and it still resulted in the same relationship; lower χ configurations were still more efficient. Another explanation could be due to the increase in the Reynolds number as the overall chord increases. This causes the boundary layer to grow further which changes the direction of the velocity exiting the trailing edge, effectively de-cambering the airfoil and thus decreasing lift.

Even though low hybridization factors proved to be more efficient, one thing that this analysis does not show is how this affects the wing bending moment. Higher hybridization factors have higher volume and also spread the load further along the wing span. This reduces the bending moment which can offer structural weight savings. This means that higher χ configurations could hold a larger payload with a lighter structure. The twist and camber of the airfoils were kept constant, if this were to be adjusted for $\chi = 0.6$, for example, it would yield significant improvements in efficiency. Combining the need for high efficiencies, low bending moment and high fairing volume indicates the need for a multi-disciplinary optimization routine, which was out of the scope of this work.

Another important aspect that was selected to be analyzed was the excursion of the neutral point and center of gravity with respect to χ as seen in Figure 5.7. The CG moves back slightly as the fairing size increases, as the spanwise growth in fairing follows the sweep angle, moving the mass of the fairing back. For a swept wing, the mean aerodynamic chord increases and shifts aft with an increase in χ. This means that the aerodynamic center shifts aft, causing the neutral point to also shift aft.

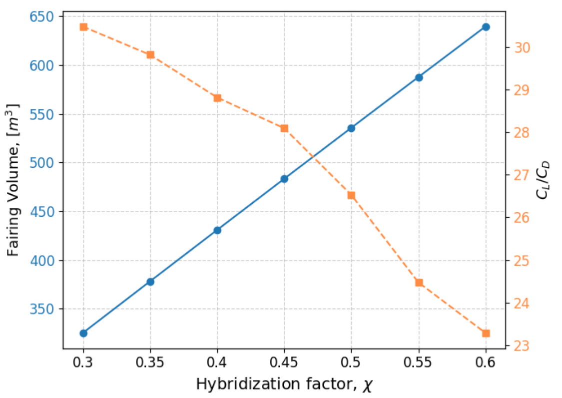

Figure 5.6: Variation of volume and aerodynamic efficiency with respect to χ at cruise conditions ($V = 238$ m/s, $\alpha = 2°$).

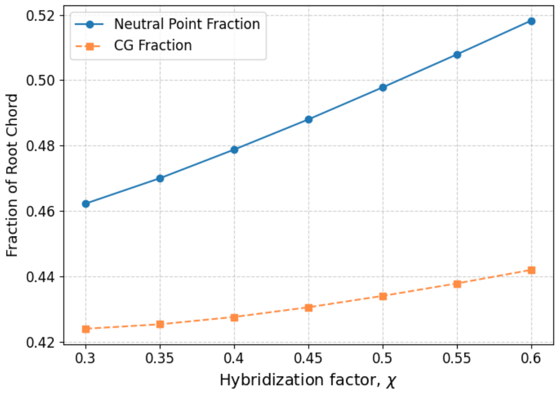

Figure 5.7: Variation of neutral point and center of gravity of the empty fairing-wing structure with respect to χ as a fraction of the root chord.

The longitudinal stability derivative results in Figure 5.8a revealed a parabolic distribution where $\chi = 0.6$ had the most negative C_{M_α}, providing the strongest restoring moment. This occurs likely due to the faster aft shift in the neutral point as χ increases, increasing the static margin and thus increasing the magnitude of C_{M_α}. The lateral-roll stability in Figure 5.8c revealed that the $\chi = 0.3$ had the most favourable restoring moment, this due to the larger outboard wing carrying a larger portion of the aircraft lift coefficient and therefore providing a larger moment. This will be further investigated in subsection 5.7.4. For the lateral static stability coefficient, shown in Figure 5.8b, a larger χ had more lateral stability. Values below $\chi = 0.4$ were laterally unstable. An explanation for this could be that as χ increases the side area on the forward part of the fairing also increases, resulting in an increase in the side force moment. In general the lateral stability coefficient was 2 orders lower than the TAW counterpart, suggesting this as an important area that needs to be addressed.

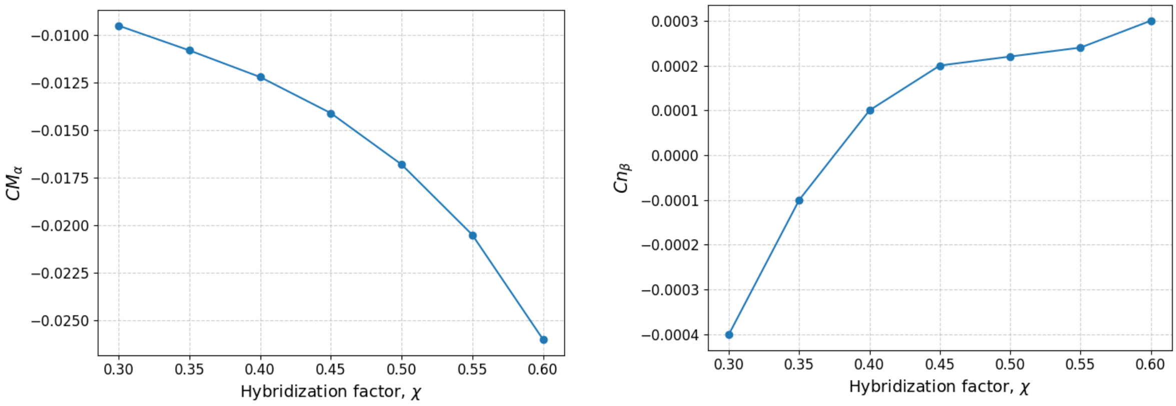

(a) Variation of longitudinal static stability, C_{M_α}, with respect to χ

(b) Variation of lateral static stability, C_{n_β}, with respect to χ

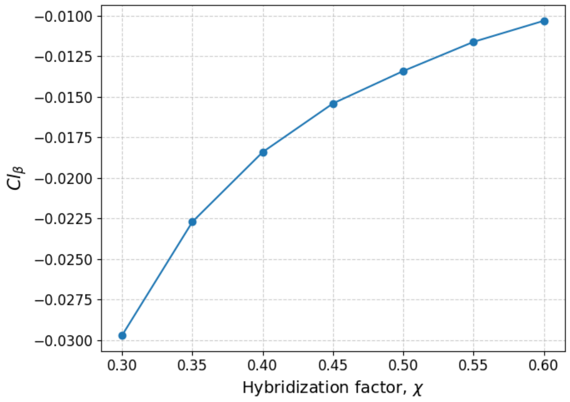

(c) Variation of lateral-roll static stability, C_{l_β}, with respect to χ

Figure 5.8: Stability derivatives at cruise conditions ($V = 238\,\mathrm{m/s}$, $\alpha = 2°$)

5.7 Wing Parameter Analysis

Now that the effects of the hybridization have been specifically isolated. The next step is to create 4 designs that respect the top level requirements of the A320-200, but using hydrogen as a fuel source. This basically means the aircraft need the same payload volume and equivalent fuel tank volume, whilst also flying at the same speed and altitude. For the each of the different hybridization configurations, the sweep, dihedral and taper ratio will be varied. For the sweep and taper, the static longitudinal stability derivative, C_{M_α}, will be extracted. For the dihedral, this will instead be the static lateral-roll stability derivative, C_{l_β}. Each parameter will be varied individually from the baseline configuration. For example, the sweep angle will be varied at a constant dihedral of 5° and taper ratio of 0.45 for all the configurations. This way, the individual effects of each parameter can be analyzed for each hybridization factor. Also, each individual configuration will be created using the design routine outlined in subsection 3.5.2.

5.7.1 Configuration Creation

Configuration 1: $\chi = 0.3$

The first configuration for testing was selected to be $\chi = 0.3$. This aircraft had the most narrow and thick fairing. This was the lowest χ possible for a BWB, based on the proposed definition of the hybridization factor. It would be possible to decrease the hybridization further, but this would make it difficult to place the hydrogen tanks. This configuration met the volume requirement by having a longer root chord and chord distribution. To have sufficient volume for the tanks, the thickness distribution of the outboard fairing had to be increased, which resulted in a strong curvature to the outboard wing, slightly compromising the convex-concave curvature requirement. This also meant that the tank positioning was fixed and could not be varied without changing the outboard wing position. This configuration shows certain similarities to Aurora D8 that was validated earlier in section 4.4. The tall and narrow fuselage would likely raise problems in terms of payload loading, as pallets would likely have to be stacked or re-organized in a better configuration, but this is not the main focus for this analysis as we just assume the payload volume is loaded successfully. Due to the narrow center body, the nose of the aircraft also becomes quite sharp.

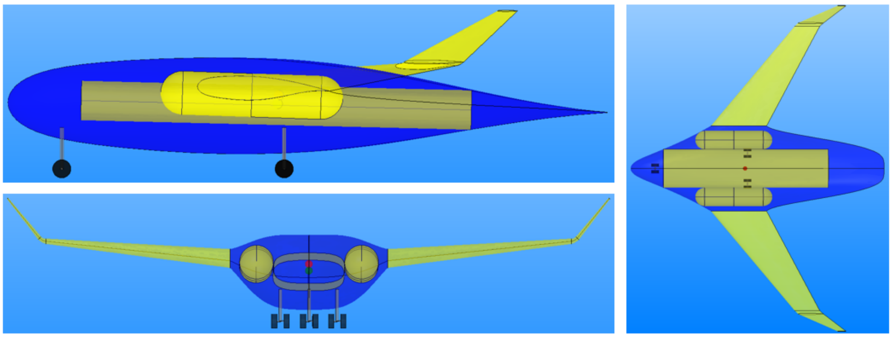

Figure 5.9: Three-view diagram of the $\chi = 0.3$ configuration

Table 5.6: Key inputs for the $\chi = 0.3$ configuration

Input	Value	Unit
χ	0.3	[-]
τ	-1	[-]
c_{root}	30.25	m
c_{tip}	3	m
Λ_{total}	47.5	m
Λ_{out}	40	m
h_{min}	2	m
a_c	[0, 5.95, 0.25, 0.66]	[-]
a_t	[0.35, 0.825, 1.25, 0.325]	[-]
a_i	[0, 0, 0, 1]	[-]
a_x	[-0.5, 0.9125, 0.5, 1.5]	[-]
a_z	[-0.175, -0.25, -0.25, 0]	[-]

Configuration 2: $\chi = 0.4$

The next configuration to be created is the $\chi = 0.4$. This requires a slightly smaller root chord than the $\chi = 0.3$ to meet the volume requirements. As the fairing is wider, the curvature between the fairing and wing is slightly reduced. This also allows for more space for the fuel tanks, allowing for a smoother concave-convex transition to the outbaord wing. However, there is still no room to vary the tank positioning.

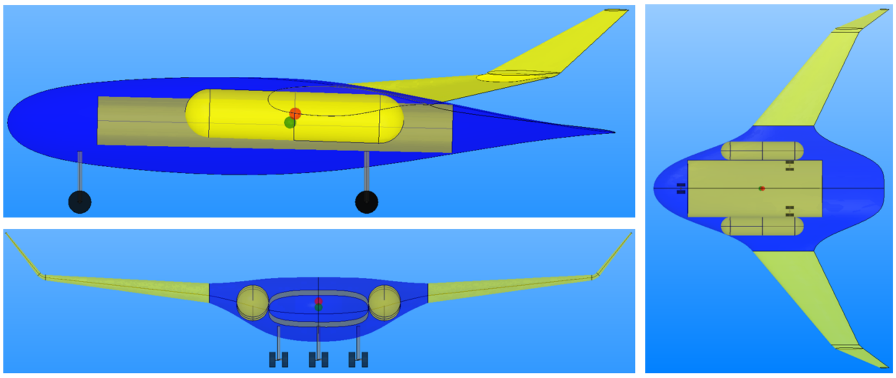

Figure 5.10: Three-view diagram of the χ = 0.4 configuration

Table 5.7: Key inputs for the χ = 0.4 configuration

Input	Value	Unit
χ	0.4	[-]
τ	-1	[-]
c_{root}	25	m
c_{tip}	3	m
Λ_{total}	48.6	m
Λ_{out}	40	m
h_{min}	3.7	m
x_{fuse}	1.25	m
z_{fuse}	0.1	m
a_c	[0, 6.25, -0.075, 0.8]	[-]
a_t	[0.35, 0.75, 1.2, 0.325]	[-]
a_i	[0, 0, 0, 1]	[-]
a_x	[0, 0.9125, 0.125, 1.5]	[-]
a_z	[-0.175, -0.25, -0.175, 0]	[-]

Configuration 3: χ = 0.5

The next configuration was chosen to be at a hybridization factor of χ = 0.5. This had a much larger fairing size, which allowed for a smaller root chord of 22.5m, to fit the fuselage. The curvature transition to the outboard wing becomes smoother with an almost flat upper surface. Now that the fairing is larger, it allows for more variation in the tank position, however it was still chosen to be as close to the leading edge as possible.

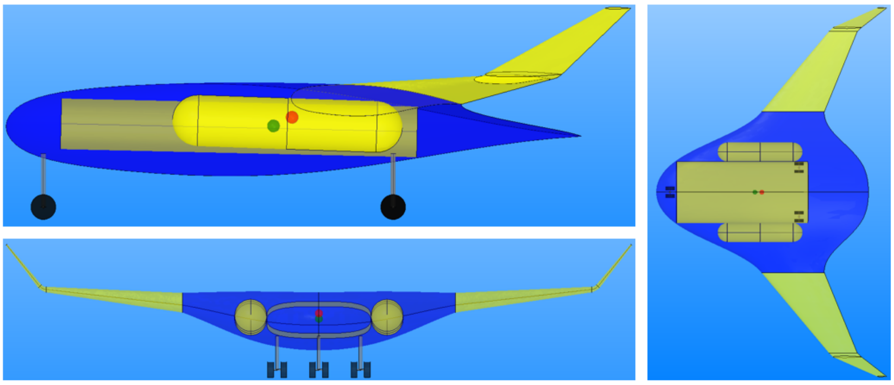

Figure 5.11: Three-view diagram of the χ = 0.5 configuration

Table 5.8: Key inputs for the χ = 0.5 configuration

Input	Value	Unit
χ	0.5	[-]
τ	-1	[-]
c_{root}	22.5	m
c_{tip}	3	m
Λ_{total}	47	m
Λ_{out}	40	m
h_{min}	2	m
a_c	[0, 6.1, 0, 0.8875]	[-]
a_t	[0.35, 0.8, 1.1, 0.325]	[-]
a_i	[0, 0, 0, 0]	[-]
a_x	[0, 1, -0.45, 1]	[-]
a_z	[-0.175, -0.25, -0.175, 0]	[-]

Configuration 4: χ = 0.6

The final configuration was selected to be χ = 0.6 which had the largest proportion of fairing with respect to the wing, allowing the fuselage to fit with the smallest root chord of 21m. Any larger χ values than this for the given sweep and taper ratio would compromise the convex-concave curvature requirements. The fairing had a much smoother distribution to the outboard wing, with a flat upper surface. As the fairing was the largest out of the four configurations, it allowed for the most variation in tank position. Comparing this to the χ = 0.3 configuration, we can see how the fairing is growing in the direction of the sweep.

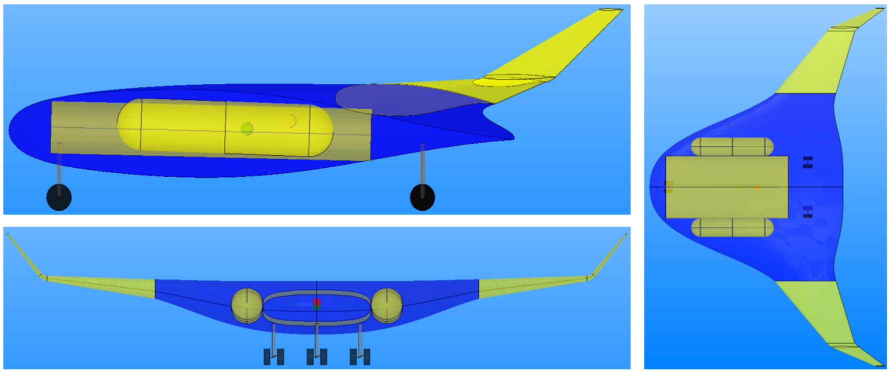

Figure 5.12: Three-view diagram of the χ = 0.6 configuration

Table 5.9: Key inputs for the χ = 0.6 configuration

Input	Value	Unit
χ	0.6	[-]
τ	-1	[-]
c_{root}	21	m
c_{tip}	3	m
Λ_{total}	48.6	m
Λ_{out}	40	m
h_{min}	2	m
a_c	[0, 6.1, 0.4, 0.9525]	[-]
a_t	[0.35, 0.65, 1.15, 0.325]	[-]
a_i	[0, 0, 0, 1]	[-]
a_x	[0, 1, -1.5, 1]	[-]
a_z	[-0.175, -0.25, -0.175, 0]	[-]

5.7.2 Wing Sweep

The variation in sweep generally followed the general expectations except for a few cases. The general expectation is that aerodynamic efficiency decreases with an increase in sweep, this is mainly due to the fact that the effective airflow that the wing experiences is now at angle, thus reducing the effective velocity that travels over the wing. This is an important reason for why high-subsonic aircraft implement sweep; to reduce the effective velocity over the wing to postpone the formation of shockwaves. But, for eccentric designs like BWB that have a very small tail arm or no tail at all, sweep with winglets may be used to increase this tail arm and find a compromise between longitudinal stability and aerodynamic efficiency. The results in Figure 5.16 provide an initial conduit for this type of analysis. It is important to note that the wingspan of the aircraft was kept constant for all the sweep angles. For most aircraft, increasing the sweep tends to increase stability by shifting back the location of the neutral point, increasing the static margin and hence improving the restoring moment. Usually, The more negative C_{M_α} is, the more longitudinally stable the aircraft is. This is known as the static longitudinal stability derivative, which describes how the pitching moment around the center of gravity changes with a change in angle of attack. Another requirement for static longitudinal stability is that zero-lift pitching moment, $C_{M,0}$, is greater than 0. This was ensured for all the cases by giving the center section a small incidence angle of $i = 2°$.

From the results in Figure 5.16, it was found that the most efficient aircraft was the $\chi = 0.3$ configuration with a sweep of $\Lambda = 35°$. As χ increased the efficiency decreased slightly, due to the reasons outline in section 5.6. The $\chi = 0.6$ was the least efficient. When looking at the individual components that make up C_L/C_D, lower χ configurations had higher C_L but also higher lift induced and skin-friction drag $C_{d,i}$ and $C_{d,0}$, but the change in C_L from configuration to configuration was greater. This is due to the outboard wing being much larger for the $\chi = 0.3$ configuration. As the outboard wing airfoil is cambered, it generates more sectional C_L than the un-cambered root airfoil. As the C_L changed the most between configurations, this means that the lift-induced drag also varied more than the skin-friction drag. Nevertheless, all configurations were much more efficient than the baseline A320-200 configuration.

For all the cases, an interesting phenomenon was observed when decreasing the sweep angle beyond $\Lambda = 35°$, the aerodynamic efficiency decreased when it was expected to increase. This effect was more pronounced for lower χ configurations due to the larger change in thickness between the fairing and the outboard wing. When looking at the drag components, this arises mainly due to an increase in the pressure drag $C_{D,p}$. In FlightStream, the pressure drag is lumped together with the lift-induced drag in $C_{D,i}$, so it cannot be found individually [64]. This means that other plots need to be visualized to deduce this drag. One for example, is the boundary layer thickness, as shown in Figure 5.15, where the leading edge of the $\Lambda = 25°$ configuration shows a thicker boundary layer. A thicker boundary layer usually indicates more pressure drag. From Figure 5.13 we can see that lower sweep angles pull the fairing forward causing a curvature that is more perpendicular to the streamwise direction, increasing the adverse pressure gradient along the wing, which slows the flow down and creates thicker boundary layer. A thicker boundary layer creates a thicker effective airfoil shape and thus generates more pressure drag. This is a type of pressure drag known as the form drag. This indicates that aircraft with a hybridization factor $\chi \leq 0.4$ should not use a sweep angle lower than 35° for high-subsonic applications.

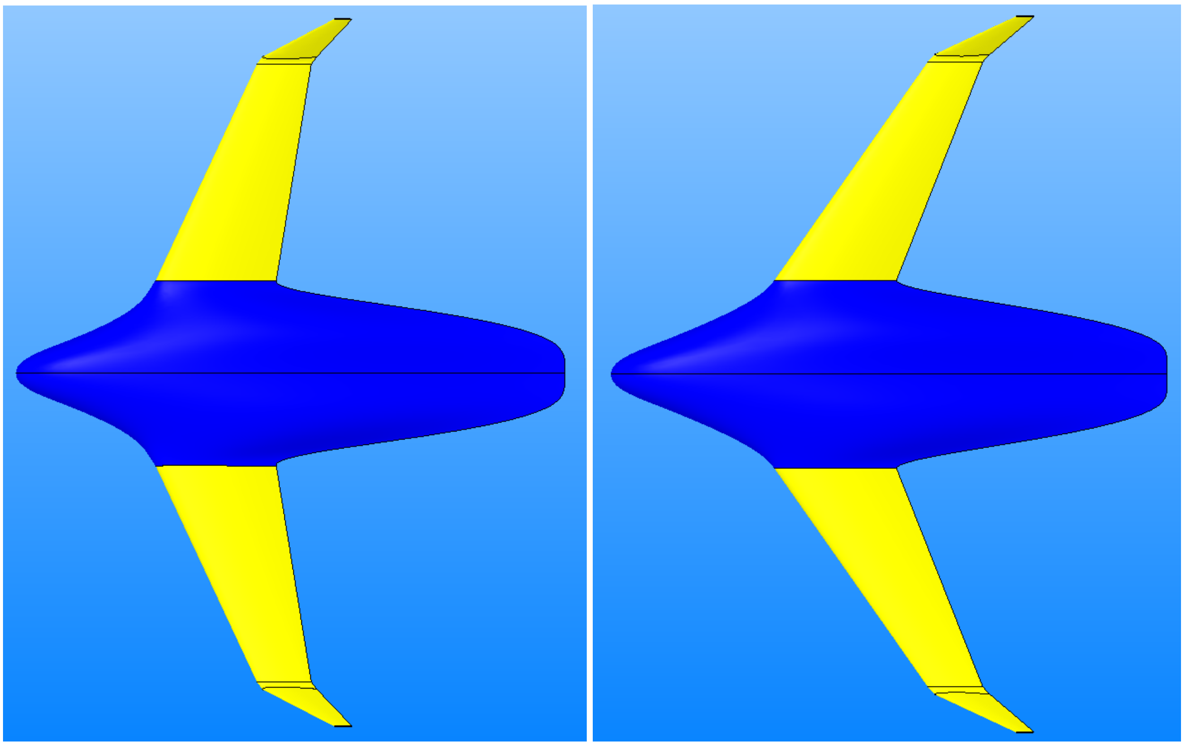
(a) Λ = 25° (b) Λ = 35°

Figure 5.13: Effect of sweep on fairing shape for the χ = 0.3 configuration

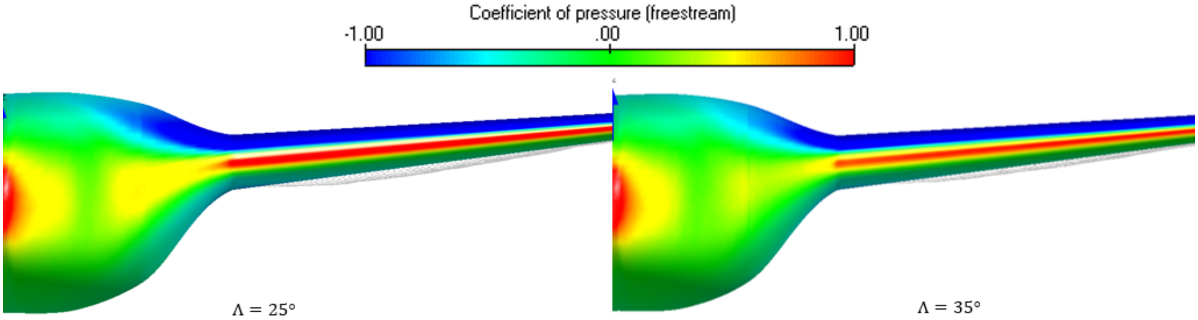

Figure 5.14: Coefficient of pressure distribution for the χ = 0.3 configuration

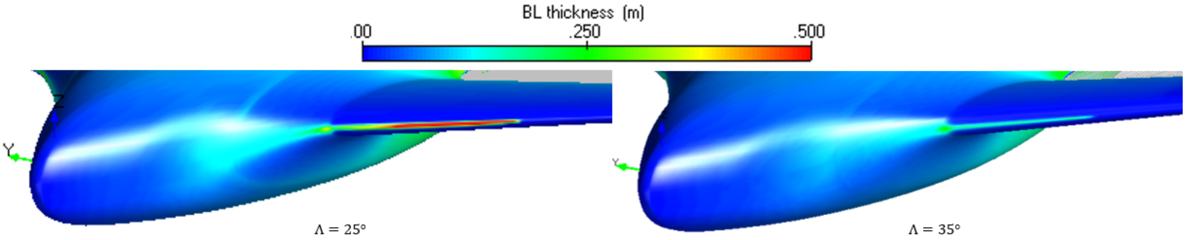

Figure 5.15: Boundary layer thickness for the χ = 0.3 configuration

The effect of sweep on stability yielded quasi-linear results for all cases, with only a few discrepancies. C_{M_α} decreased with an increase in sweep angle for all cases. By looking at the slope of the C_{M_α} vs sweep curve, we arrive at the following conclusion; the C_{M_α} of lower χ values were more sensitive to a change in sweep. This is due to them having a larger outboard wing and smaller center body, so there is a larger shift in aerodynamic center of the aircraft. For sweep values larger than $\Lambda = 40°$, the most longitudinally stable aircraft was the $\chi = 0.4$ configuration. For sweep angles lower than $\Lambda = 40°$ the most longitudinally stable was the $\chi = 0.6$ configuration. The $\chi = 0.3$ configuration was the least stable configuration as the C_{m_α} was positive until $\Lambda = 40°$.

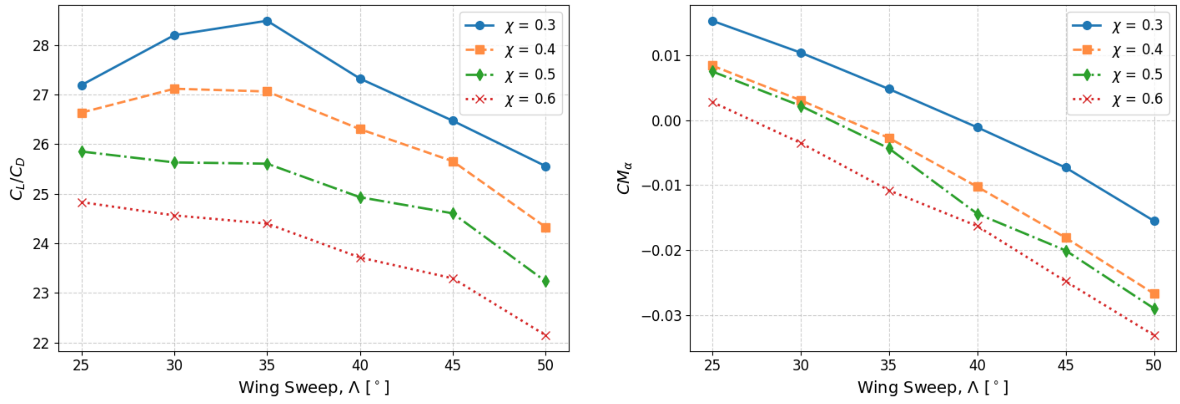

(a)

(b)

Figure 5.16: Effect of sweep on **a)** aerodynamic efficiency and **b)** longitudinal stability for different hybridization factors χ at cruise conditions (M=0.78, $\alpha = 2°$)

5.7.3 Taper Ratio

Another important wing parameter that was explored was the taper ratio, which is defined as the ratio between the tip chord and root chord of the outboard wing. As χ increases, the span of the outboard wing decreases, which means the effect of the taper ratio should differ, and thus needs to be examined for all configurations. The taper ratio in aircraft design is a crucial parameter because it can control the lift distribution, stall characteristics, drag and bending moment of the wing. For this experiment, the outboard root chord was varied whilst keeping the tip chord constant, such that the possible variations and effects were limited.

From Figure 5.17, the aerodynamic efficiency increased with an increase in taper ratio. One of the driving factors is due to the fact that a increasing the taper ratio reduces the outboard wing area, which increases the aspect ratio for fixed span. This then causes a reduction in the lift-induced drag, which is obtained through the equation,

$$C_{D,i} = \frac{C_L^2}{\pi ARe} \tag{5.2}$$

where the aspect ratio is $AR = \frac{b^2}{S}$, C_L is the lift coefficient and e is the Oswald efficiency factor. From this we can see that a smaller wing area, S, increases the AR and thus reduces $C_{D,i}$. This explains the increase in efficiency as the taper ratio increases. Another aspect that should be considered is how elliptical the lift distribution is. This is quantified by the Oswald efficiency factor, e. A study performed by Guzelbey et al. showed that increasing the taper ratio actually slightly decreased the Oswald efficiency factor [69]. This would increase $C_{D,i}$ for an increase in taper ratio. However, this effect is diminished by the larger increase in AR.

When looking at the sensitivity of the efficiency, so how *much* the C_L/C_D changed with a change in taper ratio, the $\chi = 0.3$ configuration was the most sensitive to a change in taper ratio as it had the greatest increase in C_L/C_D. This is expected due to $\chi = 0.3$ having the a larger outboard wing, meaning there is a larger change in surface area when varying the taper ratio. This leads to the main conclusion of these results; the efficiency of aircraft with lower χ values is greater but are also more sensitive to a change in taper ratio.

The change in longitudinal stability with respect to taper ratio also provided interesting insights. Increasing the taper ratio generally produced lower C_{M_α}, except for the $\chi = 0.3$ case. A reason for this could be due to how the wing is modelled, as the leading edge of the wing is fixed as the chord increases, meaning the trailing edge moves with a change in chord. This change has a large effect on the size of the fairing section and increases as the hybridization factor increases, as the have a larger fairing section. So, as the chord decreases, the overall CG moves slightly forward, creating a larger static margin and thus increasing the C_{M_α}. Therefore, as χ increased, the sensitivity of C_{M_α} to a change in taper ratio also increased. This can be seen through the the steeper slope of the $\chi = 0.6$ configuration compared to the $\chi = 0.3$ and $\chi = 0.4$ in Figure 5.17b. A reason for this is due to the fact that the taper ratio has a much stronger effect on the area of the fairing for higher values of χ, as it is dictated by the outboard root chord. The change in wing area between taper ratios $\lambda = 0.25$ and $\lambda = 0.55$ was 39.6m^3 for $\chi = 0.5$ and 74.8m^3 for $\chi = 0.6$. Increasing the planform area (lower taper ratio) shifts the neutral point location forwards, thus creates a less negative C_{M_α}, which agrees with the results of the $\chi = 0.3$ configuration. This suggests that for a BWB configuration, the largest possible taper ratio should be used, without compromising the volume requirements of the center body.

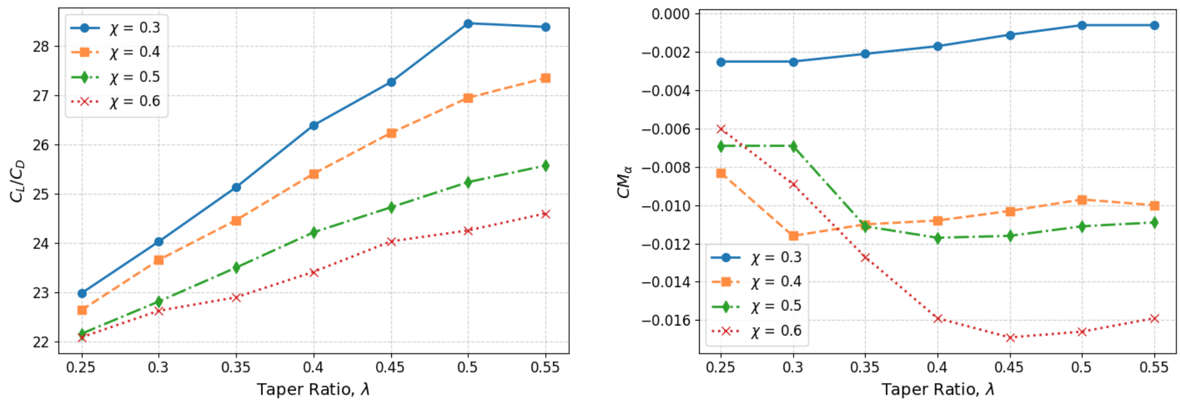

(a) **(b)**

Figure 5.17: Effect of taper ratio on **a)** aerodynamic efficiency and **b)** longitudinal stability for different hybridization factors χ at cruise conditions (M=0.78, $\alpha = 2°$)

5.7.4 Dihedral

The dihedral analysis provided a valuable insight into how the lateral stability and aerodynamic efficiency varied with both hybridization factor and dihedral. The lateral stability in this case is the lateral-roll stability, defined as C_{l_β}. This describes the rolling moment, or the moment about the conventional x-axis, with respect to a change in sideslip angle β. A negative C_{l_β} implies that the aircraft has a restoring rolling moment with a change in sideslip angle, meaning the aircraft has a tendency to move back to its level position. When the wing experiences airflow from the side, due to sideslip or a gust, it causes one of the wings to rise and the other one to drop. Applying a small angle of dihedral to the wing improves this restoring moment because the wing that has risen will now experience a lower angle of attack, reducing the lift, and the lower wing will experience a higher angle of attack which increases the lift. So, if the wing that has dropped can increase its lift, it moves up again towards its original position. This effect is increased for a small increase in dihedral angle, as the difference in lift between the lower and higher wing increases and thus provides a larger restoring moment, as shown from the results in Figure 5.19b. These results also indicate that a lower hybridization factor proved to be consistently more laterally stable at a given dihedral angle. This is because a lower χ value has a larger outboard wing meaning there is a larger sectional lift coefficient outboard of the aircraft, giving a larger rolling moment arm and thus generating a stronger restoring moment. This means that lower χ values have increased lateral-roll sensitivity with a change in dihedral as $\chi = 0.3$ has the greatest difference in C_{l_β} between $\Gamma = 0°$ and $\Gamma = 10°$. In general, the results for the C_{l_β} with respect to a change in dihedral showed little discrepancies, and correlated well with the expected theory, indicating a successful simulation.

The results for the aerodynamic efficiency with respect to dihedral, in Figure 5.19a, also followed the expected behavior, with some minor deviations. In general, small angles of dihedral have little effect on the lift and drag of an aircraft, except for higher angles of attack [70]. However, as this is a BWB, a change in dihedral also has a large effect on the shape and curvature of the fairing and can have a greater effect on its effective angle of attack. This is mainly seen with the $\chi = 0.3$ configuration, as the C_L/C_D varied significantly between $\Gamma = 0°$ and $\Gamma = 10°$. This due to the fact that the $\chi = 0.3$ configuration experiences a greater change in fairing curvature as Γ changes, as shown in Figure 5.18. This means the effective angle of attack is lower for $\Gamma = 0°$ and higher for $\Gamma = 10°$. This effect diminishes quickly as χ increases because there is a much smaller change in curvature.

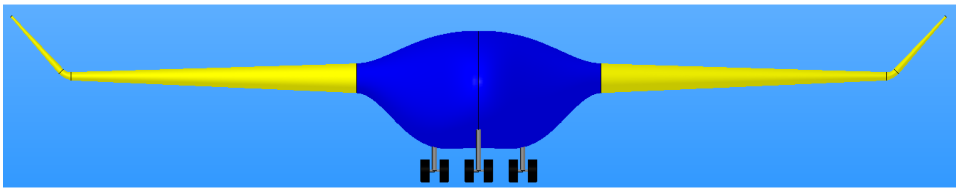

(a) $\Gamma = 0°$

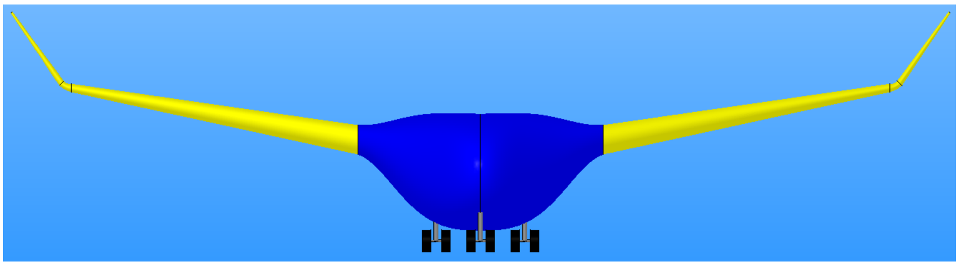

(b) $\Gamma = 10°$

Figure 5.18: Effect of dihedral change on the front planform of the $\chi = 0.3$ configuration

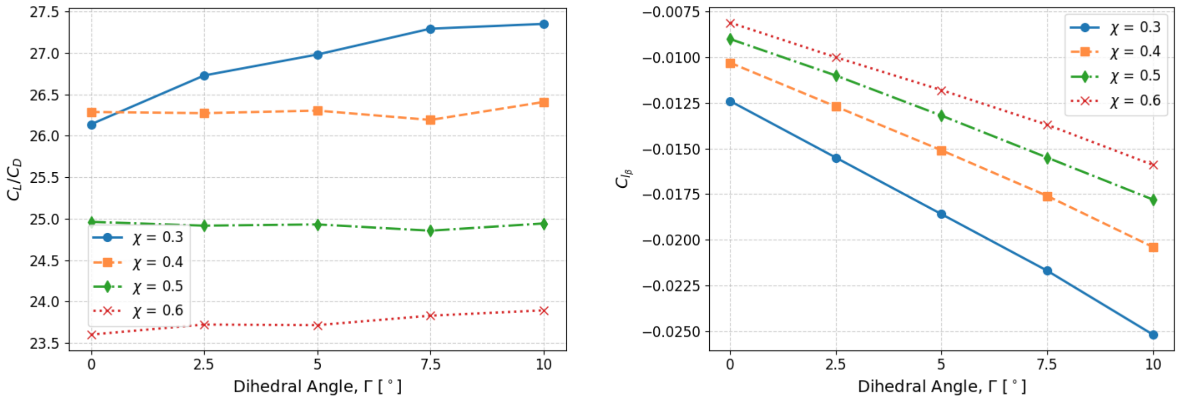

(a) **(b)**

Figure 5.19: Effect of dihedral on **a)** aerodynamic efficiency and **b)** lateral-roll stability for different hybridization factors χ at cruise conditions (M=0.78, $\alpha = 2°$)

5.7.5 Pressure Distributions

An important next step is to analyze the pressure distribution for each configuration, for the baseline wing parameters of $\Lambda = 40°$, $\Gamma = 5°$ and $\lambda = 0.45$. This will be done for 4 different angles of attack of ranging from $\alpha = 2°$ to $\alpha = 12°$. For the lower hybridization factors, like $\chi = 0.3$ in Figure 5.20, the outboard wing carries a majority of the lift. The stronger pressure drop in this region suggests that separation would be more likely to occur earlier on the outboard wing than a larger configuration at the same angle of attack. As the angle of attack increases, the low-pressure area grows faster on the centerbody of the $\chi = 0.6$ configuration, suggesting it may be more susceptible to separation on the centerbody. At lower angles of attack however, the $\chi = 0.6$ configuration had an overall less negative coefficient of pressure over the whole wing, suggestig it may have better separation characteristics at cruise. The $\chi = 0.3$ configuration had interesting behaviour at the aft part of its center section, as there was staggered regions of separated and attached flow. This suggests there are mesh imperfections. One reason for this could be due to skewed cells near this trailing edge, as it was a trailing edge almost tangent to the flow.

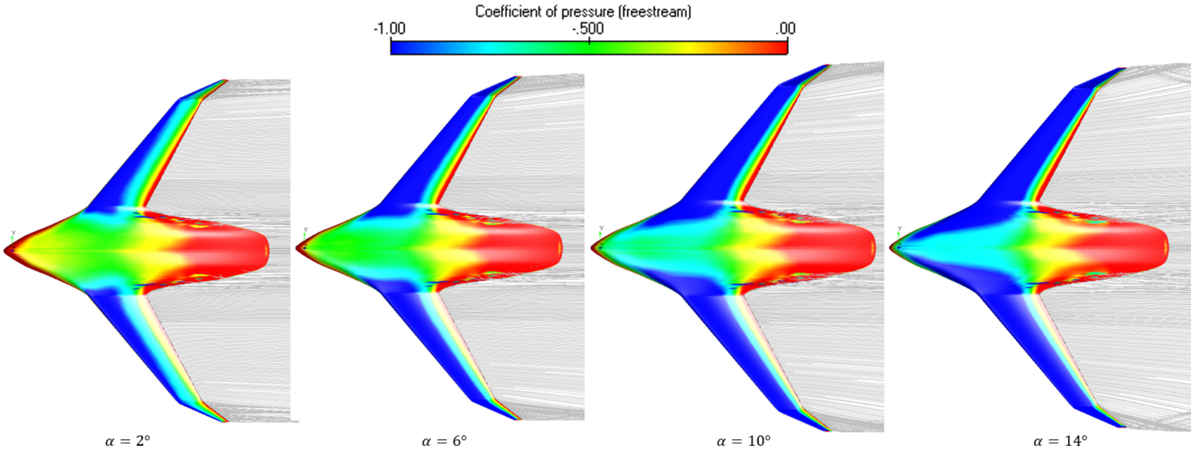

Figure 5.20: Upper surface coefficient of pressure plots for the $\chi = 0.3$ configuration

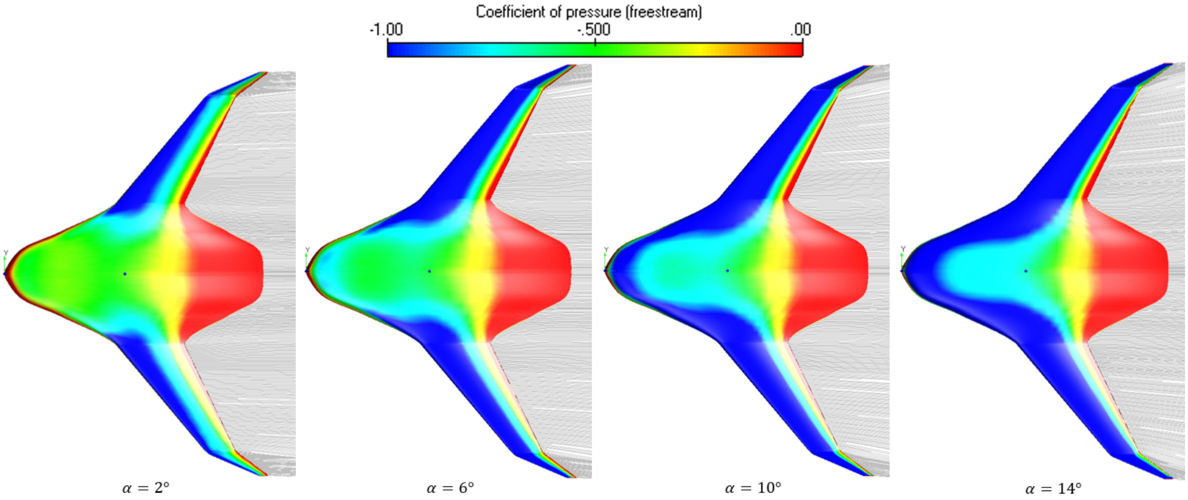

Figure 5.21: Upper surface coefficient of pressure plots for the $\chi = 0.4$ configuration

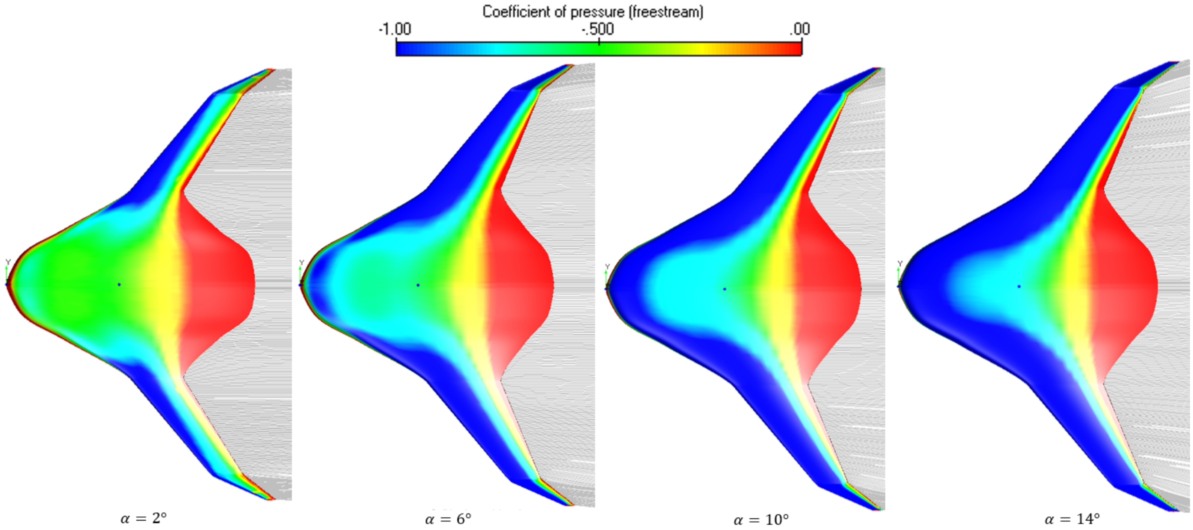

Figure 5.22: Upper surface coefficient of pressure plots for the χ = 0.5 configuration

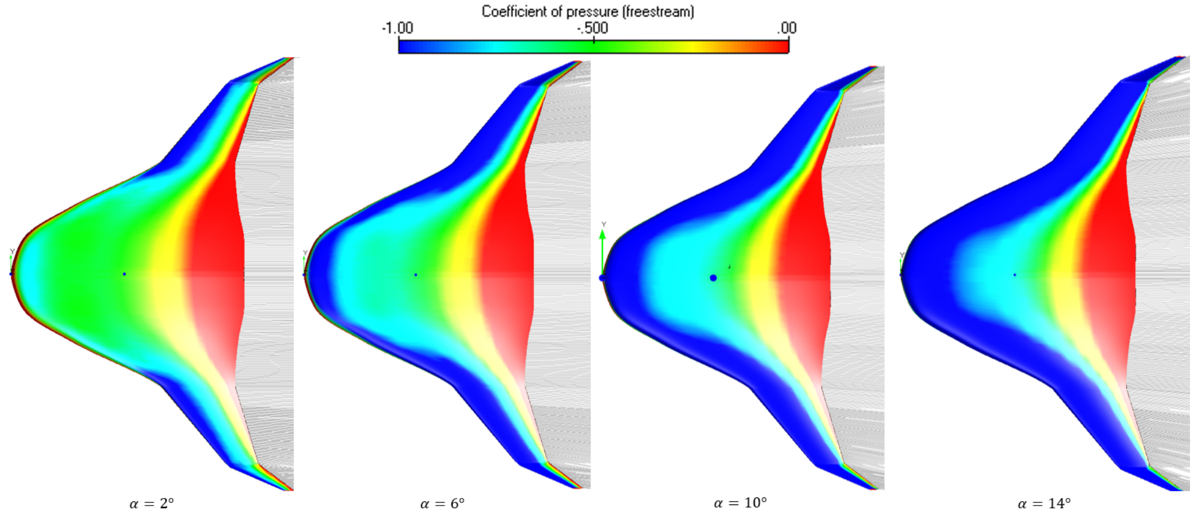

Figure 5.23: Upper surface coefficient of pressure plots for the χ = 0.6 configuration

5.7.6 Design selection and iteration

Once the best configuration of interest has been selected based off of the wing parameter analysis we can begin a simple design iteration process. This process will be iterated manually, guided by pressure contours, separation contours and numerical results. The main goal here is to increase the aerodynamic efficiency as much as possible, without compromising longitudinal stability and, if possible, improving it. This will be done by looking at the C_P contours over the wing and then making small adjustments to areas that require attention. The first step is to find a set of thickness and z-position shape factors, a_t and a_z, that can create a better pressure distribution whilst maintaining a smooth concave-convex curvature. Then, the chord and x-positioning factors, a_c and a_x, will also be checked to see if slight changes to the top planform can prove beneficial. Finally, the incidence angle distribution, a_i, will also be adjusted based on the pressure and separation distribution. This will be done until a 1% improvement in efficiency is found without reducing the longitudinal stability derivative. Then, new plots for the pressure and separation will be evaluated to see how the efficiency was improved.

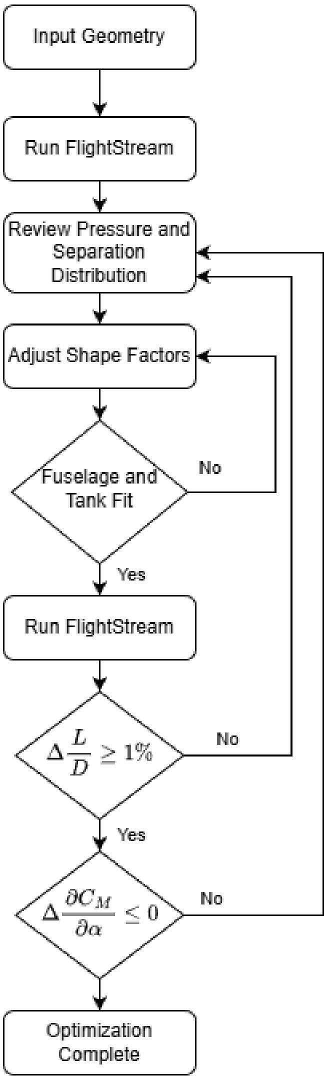

Figure 5.24: Design loop for optimizing fairing curvature for a specific χ configuration

The selected design, as the input for this routine, will have a hybridization factor of $\chi = 0.4$, with an outboard wing sweep of $\Lambda = 35°$, a dihedral of $\Gamma = 5°$ and a taper ratio of $\lambda = 0.55$. When looking at the pressure coefficient plots in Figure 5.25, it can be seen that the main area of concern is the aft center-body, which has a more positive C_P and is more prone to separation. After iterating this process around 5-6 times, it was found that changing the a_t, a_z, a_c and a_x did not yield sufficient improvements to meet the 1% threshold. This means that the preliminary BWB creation routine in subsection 3.5.2 yields acceptable performance. Surprisingly, significant improvements in efficiency were realized when making small adjustments to the incidence angle distribution, a_i. By slightly decreasing the incidence angle distribution of the outboard fairing, the aerodynamic efficiency improved by 1.03%. As the fairing incidence was more aligned with the flow direction, this created a slightly more negative C_P distribution on the aft portion of the upper surface and also pushed the point of boundary layer transition further aft. The parameters describing the improved design are outlined in Table 5.10.

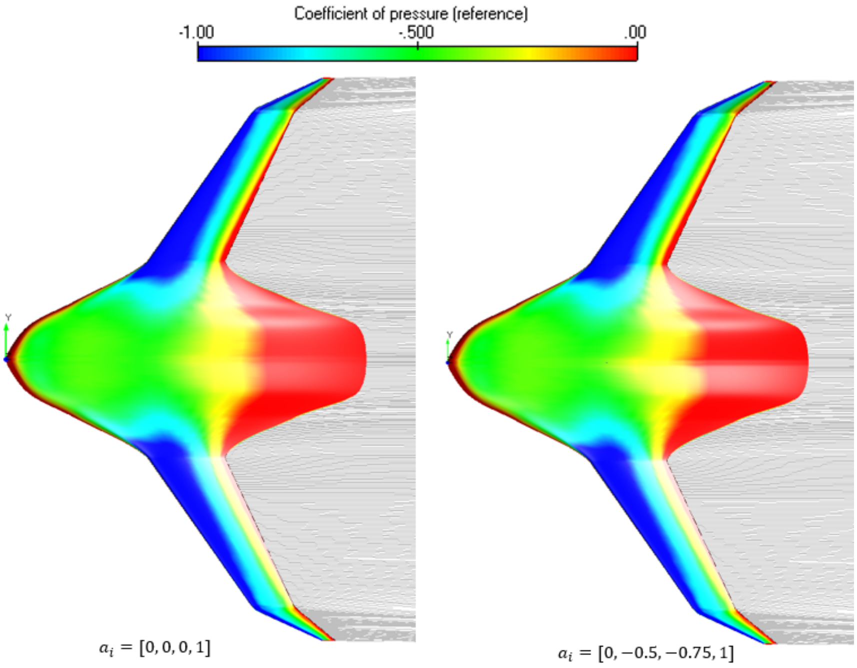

$a_i = [0, 0, 0, 1]$

$a_i = [0, -0.5, -0.75, 1]$

Figure 5.25: Effect of changing the a_i shape factors on the upper surface pressure coefficient distribution

Table 5.10: Key inputs for the improved $\chi = 0.4$ configuration

Input	Value	Unit
χ	0.4	[-]
τ	-1	[-]
b	34	m
c_{root}	25	m
c_{tip}	3	m
Λ_{total}	44.9	m
Λ_{out}	35	m
h_{min}	2	m
a_c	[0, 6.35, -0.35, 0.65]	[-]
a_t	[0.35, 0.75, 1.2, 0.325]	[-]
a_i	[0, -0.5, -0.75, 1]	[-]
a_x	[0, 0.9125, 0.125, 1.5]	[-]
a_z	[-0.175, -0.25, -0.25, 0]	[-]

5.7.7 Discussion of Wing Parameter Analysis

The optimization study examined a range of hybridization factors, followed by variations in their wing sweep, dihedral and taper ratio. It also examined how the shape factors can be directly used to modify pressure and separation distributions. The results confirmed that the hybridization factor remains the dominant parameter influencing aerodynamic performance and stability.

The $\chi = 0.3$ and $\chi = 0.4$ configurations consistently achieved the best aerodynamic efficiency. Higher χ values had reduced aerodynamic efficiency but much higher volume and lower wing bending moment, suggesting that more efficient structures can be created with higher hybridization factors. If a twist distribution was tailored to the $\chi = 0.6$ configuration, for example, it could potentially see large improvements in aerodynamic efficiency whilst maintaining these structural benefits.

The analysis of the wing sweep confirmed the expected trade-off between aerodynamic efficiency and longitudinal stability. Increasing sweep reduced C_L/C_D but improved stability by shifting the aerodynamic center aft. All configurations reached their maximum efficiency at $\Lambda = 35°$, with $\chi = 0.3$ performing best due to its larger outboard wing. An unexpected drop in efficiency occurred when sweep was reduced below 35°, caused by the fairing moving forward and steepening its curvature, which increased adverse pressure gradients, thickened the boundary layer, and raised pressure drag. This effect was strongest for lower χ values.

The variation of taper-ratio with respect to χ showed that higher taper ratios consistently improved aerodynamic efficiency by reducing outboard wing area and increasing effective aspect ratio, thus reducing lift-induced drag. Lower χ configurations were most sensitive to this change because of their larger outboard wings. Increasing taper ratio generally reduced static longitudinal stability, with sensitivity increasing as χ increased. This was linked to the larger planform-area changes at higher χ, which shift the neutral point forward and make C_{M_α} less negative. Overall, sweep and taper ratio exhibited predictable effects, but their influence became stronger as hybridization increased.

The dihedral study showed that increasing dihedral consistently improved lateral-roll stability for all hybridization factors. A more positive dihedral angle generates a larger restoring rolling moment during sideslip, following the expectations, Lower hybridization factors exhibited the strongest stabilizing effect because their larger outboard wings provide greater sectional lift and a longer moment arm, making $\chi = 0.3$ the most sensitive configuration to changes in dihedral. Aerodynamic efficiency was only weakly affected by dihedral for most configurations, consistent with conventional aircraft behaviour. However, the $\chi = 0.3$ configuration showed a more noticeable variation in C_L/C_D between $\Gamma = 0°$ and $\Gamma = 10°$. This resulted from greater sensitivity in the fairing curvature to a change in dihedral, which altered the effective local angle of attack. For larger hybridization factors, the fairing shape changed much less with dihedral, and the influence on efficiency became minimal.

This design routine served as a proof of concept for how the integration of FlightStream, ParaPy and a novel parameterization can be used to automate aerodynamic studies. It also showed how the hybridization factor can be used to evaluate BWB configurations in a novel manner, opening up new possibilities for their design.

5.8 Implementation into design pipeline

Using the results from the previous section, a configuration with a hybridization factor of $\chi = 0.4$, an outboard wing sweep of $\Lambda = 35°$, a dihedral of $\Gamma = 5°$ and a taper ratio of $\lambda = 0.55$ was selected. After performing a short design iteration with the shape factors, this design yielded an efficiency of $C_L/C_D = 28.66$. With this design, the first few steps of implementing the aircraft into a typical design pipeline will be carried out. This will involved using the TLAR, simulation results and ParaPy model to create a matching diagram as well as a CG loading diagram.

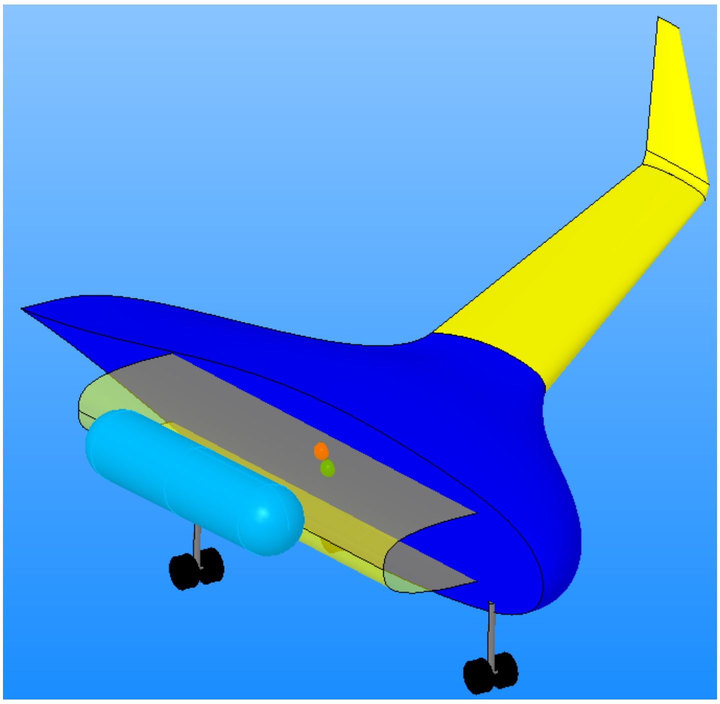

Figure 5.26: Split-view of selected design and its components

5.8.1 Matching Diagram

Using the information from the selected conceptual design and the requirements highlighted in Table 5.1, a matching diagram was created based off of performance calculations found in literature [58]. This diagram shows the region where all of the basic requirements for the aircraft are met, which in this case is considered to be above the cruise speed and take-off field length, and to the left of the minimum speed requirement. So when future changes are made to the geometry, the designer can use this to ensure the design is still feasible. Another important feature of this matching diagram is that it also shows the required power of the motors for a given wing loading, which is crucial when reaching the engine integration phase. The design cruise lift coefficient used here was 0.6, as this was what was found for the $\chi = 0.3$ configuration flying at $\alpha = 2°$. This is a little higher than the typical C_L of an A320-200, which means maybe the configuration could fly at a slightly lower angle of attack. The climb rate was selected to be 0.5m/s at the cruise altitude, which defines the service ceiling altitude for a typical transport aircraft [58]. The only climb gradient evaluated was the CS25.119, which states a 3.2% climb gradient at the maximum take-off mass with all engines operating. Other assumptions were made based off of the data in Table 5.1. The design point was chosen to be 3598 $\mathrm{N/m^2}$ for the wing loading and 0.275 for the thrust-to-weight.

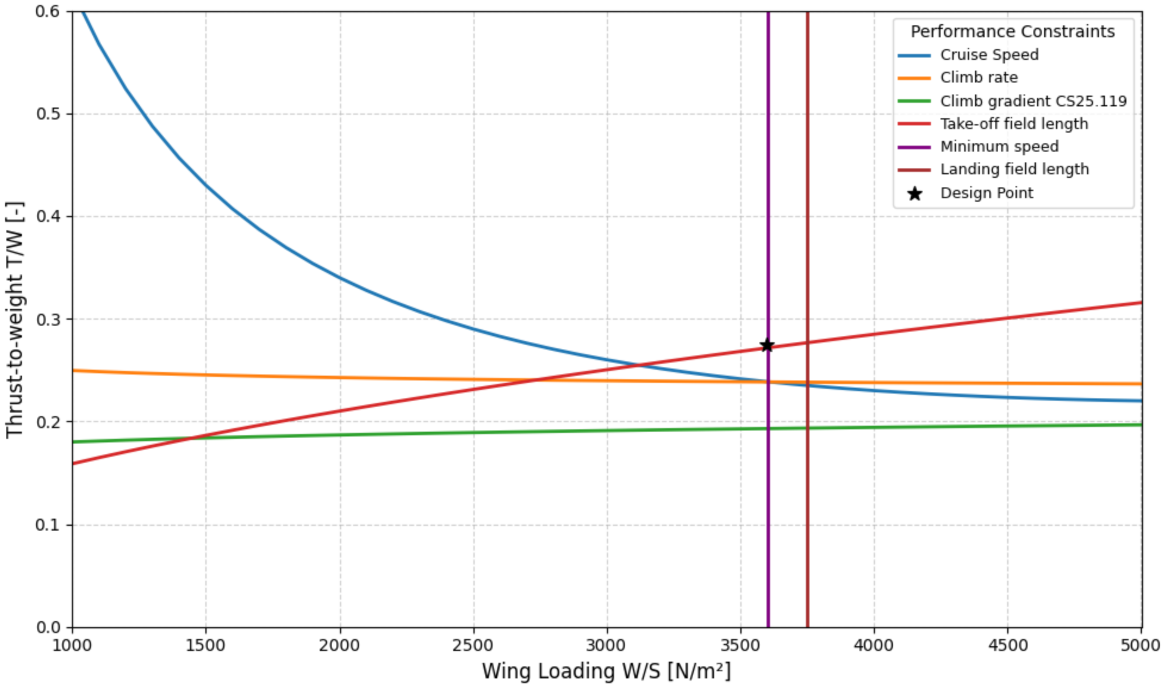

Figure 5.27: Matching diagram for the final design using the requirements outlined in Table 5.1

5.8.2 Center of gravity excursion

A very important aspect of designing a BWB is to analyze how the center of gravity will shift for specific loading configurations. Using a loading diagram helps visualize this shift, displaying the location of the CG for a specific mass configuration. The loading diagram shown in Figure 5.28 is relatively different than one made for conventional aircraft due to the fact that it is a BWB and hydrogen powered. Normally, the CG is expected to travel closer to the leading edge of the MAC, around 0.2 to 0.4, but as the MAC is much larger for BWB, its excursion is pushed further aft. As the MAC is very close to the center of the aircraft, x_i/MAC can almost be viewed as a fraction of the fuselage length. This also means that the change in x_i/MAC is relatively small in comparison to a TAW. Another difference is the significantly smaller fuel mass fraction in comparison to conventional aircraft. Hydrogen powered aircraft require heavy tanks and fuel cell systems to power the engines, but the amount of hydrogen required is quite modest due to its high energy density. This is seen in Figure 5.28 through the small increase in m_i whenever fuel is added. When the fuel is added to the OEM and max payload, the CG moves slightly aft due to the placement of the fuel tanks as seen in Figure 5.26. The payload also has a very important role in the loading of the aircraft as it is loaded very far forward with respect to the OEM. For a more robust design, the nose of the aircraft should be stretched forward, with the wings either placed further back or slightly more swept. This loading diagram reveals a significant weak point in this design and would need to be studied further to ensure a safe and certifiable aircraft.

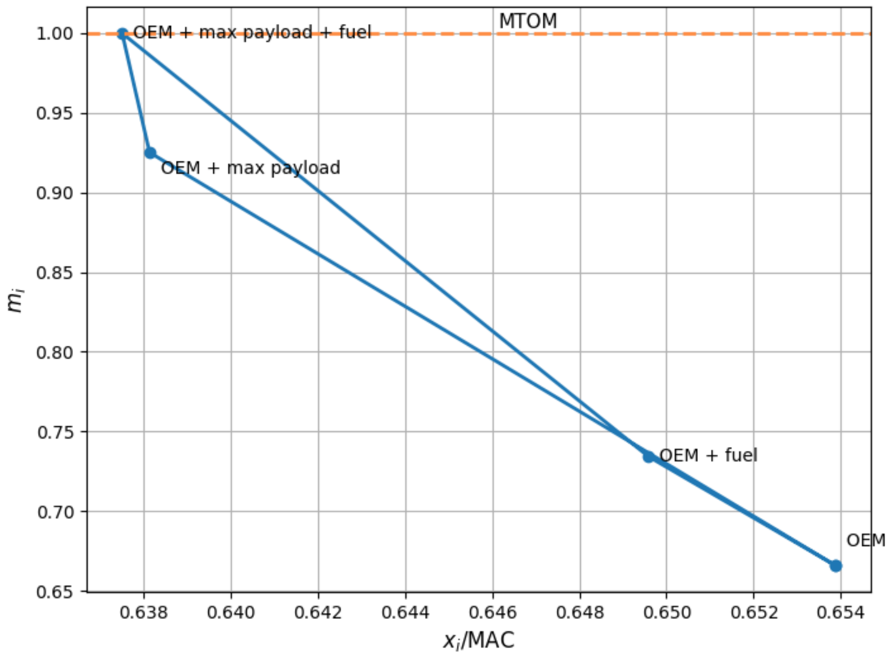

Figure 5.28: Loading diagram of final conceptual design

Chapter 6

Conclusions

This research developed and validated a novel three-dimensional parametric framework that enables the geometric representation of the transition between conventional tube-and-wing aircraft and blended wing-body configurations within a single modelling environment. The framework allows aircraft performance, stability, and volumetric characteristics to be directly related to the geometric parameters of BWB aircraft, addressing a long-standing challenge in the conceptual design of highly integrated aircraft.

This parameterization used a 3D CST approach along with a newly introduced parameter; the hybridization factor. Although there is a substantial learning curve, using shape factors to describe an aircraft's geometry has proven to be very handy for creating BWB/HBWB designs based on an initial baseline TAW configuration. This new methodology also enabled the novel analysis of BWB configurations, allowing for the exploration of how different levels of wing-body integration affect aircraft geometry and performance.

The validation displayed the flexibility of the parameterization, as it was able to model a range of different aircraft configurations to a high degree of accuracy. The use of shape factors enables aircraft to be reproduced with a set of weights, rather than fixed inputs. This reduces the amount of physical inputs required for the sizing, especially for complex geometries like fairings. Although it may be less intuitive, this approach has the potential to be more beneficial for optimizations. A good argument for its use would be the comparison of two common airfoil parameterizations, the PARSEC and CST, which were introduced in chapter 2. PARSEC has many design variables that make physical sense for a designer, like leading edge radii and maximum thickness. This is useful for a designer but not for an optimizer, which is why methods like CST are preferred for design optimization studies, and have proven successful in 2D applications [71].

Before individually performing a wing parameter analysis on a set of configurations, a sensitivity analysis on the hybridization factor was performed in section 5.6. This consisted of adjusting the hybridization factor whilst keeping all other geometric parameters constant and collecting key parameters from the FlightStream simulation. These parameters included volume, longitudinal stability, directional stability, neutral point location and CG location. This was then followed by a wing parameter analysis that explored the effect of wing sweep, taper ratio and dihedral for different χ configurations, whilst keeping all other wing parameters constant. Then, the separation characteristics for each χ configuration were analyzed for a range of angles of attack. From these results, an optimum design was selected for further analysis to see the effects of varying the shape factors. It was found that little improvements could be made by changing the thickness ratio, chord and positioning shape factors, which suggested that the geometry creation methodology in subsection 3.5.1 successfully created viable baseline designs. To begin the implementation to the design pipeline, a matching diagram and CG loading diagram was created for the selected design.

To quantify the conclusions of this thesis, the research question will be reiterated:

Research Question

What are hypotheses and methods to parametrize the geometric representation of an aircraft digital model regardless of the degree of integration between fuselage and wing, ranging from the wing-body configuration to the blended wing-body?

This study demonstrated that a unified geometric representation between a TAW, HBWB and a BWB is indeed achievable. This was accomplished through the introduction of the hybridization factor combined with a 3D Class-Shape Transformation parameterization. This methodology allows for a smooth transition between all levels of integration, with a modest amount of parameters. Using this approach enables designers to link geometric variations directly to aerodynamic performance, as well as provide a new way to analyze BWB/HBWB aircraft.

This then invoked the following sub questions, which will now be answered:

Is it possible to define a unique hybridization factor that allows a parametric and coherent representation of the different levels of integration between fuselage and wing?

After conducting this study, it was found that it is not possible to define a single parameter that can accurately represent all levels of wing-fuselage integration. This was due to the different requirements in fairing curvature when transitioning from a TAW to a BWB. However, by implementing this new hybridization parameter with the help of 3D-CST methodology, it is possible to model a wide spectrum of configurations. This was proven through the validation and the design study, where the design of a TAW, BWB and HBWB were produced using a single application.

What are the geometric features and associated parameters that cannot be directly related to the level of integration between fuselage and wing?

The main geometric feature that is not directly related to the level of integration is the fairing curvature. For lower levels of integration, there is a different curvature requirement for the wing-body fairing, as here the fairing serves as a wing-body fillet rather than a complete fuselage housing. This means that there had to be a significant adjustment to the shape factors to transition from TAW to a BWB. This process was formalized in subsection 3.5.2, showing how to do this in a modest number of steps. However, once the shape factors were established for configurations with higher hybridization factors, like $\chi \geq 0.3$, they required very few changes to maintain the fairing curvature. For example, if you increase the hybridization from $\chi = 0.3$ to $\chi = 0.6$, you only need to make small changes to the 3rd shape factor $a_{j,3}$ to maintain the curvature requirements outlined in section 3.5.

What are the aerodynamic effects related to varying wing parameters for different levels of integration between wing and fuselage?

When looking at the results from the sensitivity study in section 5.6, it can be seen that there is a large increase in efficiency as soon as $\chi = 0.3$ as this is the point where the fuselage becomes fully enclosed by the fairing. This is seen by comparing the baseline A320-200 to the BWB configurations. Then as χ increased beyond $\chi = 0.3$, the efficiency slowly dropped due to the increase in wing planform area, which decreased the overall wing lift coefficient, C_L, and increase $C_{D,0}$, as explained in section 5.6. In terms of wing parameters, varying the sweep revealed that lower χ configurations were more prone to adverse pressure gradients at sweep angles below 35° due to the sharper fairing curvature transition to the outboard wing. This created a thicker boundary layer near the wing-fairing intersection which increased the pressure drag and thus reduced the aerodynamic efficiency. As lower χ configurations have a larger outboard wing, their efficiency was also more sensitive to a change in taper ratio. However, for lower χ configurations, the static longitudinal stability derivative was less sensitive to a change in taper ratio. When changing the dihedral, there was a significant variation in the aerodynamic efficiency of the $\chi = 0.3$ configuration, whilst larger χ values stayed almost constant. This was due to the larger change in fairing curvature that $\chi = 0.3$ experiences, which altered its effective angle of attack. This means that designers need to pay careful attention when changing the dihedral of aircraft with lower hybridization factors.

What are the design parameters that may drive the selection of the most promising integration level?

The selection of the most suitable hybridization factor is governed by a combination of volumetric, geometric, and aerodynamic requirements. The most influential of these are the payload volume and the allowable wingspan. This determines the chordwise and spanwise extent of the fairing, as well as its curvature, which in turn affects the distribution of lift, the wetted area, and the resulting aerodynamic efficiency. For example, lower values of χ provide smaller center-body volumes and sharper fairing transitions, while higher values yield larger fairing volumes and smoother curvatures, which alters both performance and stability. The next design drivers would be the stability characteristics. In general, higher χ values exhibited better static longitudinal stability, due to the increased contribution of the center-body to the overall lift and the rearward shift of the aerodynamic center, increasing the static margin. Conversely, lower χ configurations were more sensitive to variations in sweep, taper ratio, and dihedral, and more prone to adverse pressure gradients near the wing–fairing junction. These stability considerations directly influence the feasibility of a given integration level, particularly when seeking to satisfy certification or handling requirements. However, it should be noted that BWB aircraft can be intentionally designed with relaxed or even negative static stability, relying on active control systems to maintain controllability in exchange for improved aerodynamic performance, as discussed by Rocca et al. in [33]. This means that while stability trends give strong guidance, they do not necessarily impose absolute limits on the achievable integration level. The mission requirements will also be an important driver for the selection of the most promising χ value. Parameters such as the design lift coefficient, wing loading, and thrust-to-weight ratio influence how different χ values perform within the constraints of the matching diagram. Certain χ values may offer good aerodynamic efficiency but become less attractive due to insufficient volume for fuel or payload. Even if it is possible to "fit" the fuel and payload, certain χ values may not allow for a smooth concave-convex curvature to the outboard wing which can generate issues with its aerodynamics, like the ones discussed in section 3.5.

Is there any level of integration between the wing and fuselage that can be considered globally an optimum?

For a given set of fuselage, wing, and mission requirements, the results of this study indicate that there exists a local aerodynamic optimum for the hybridization factor, however as this optimum is specific to the baseline constraints, it cannot be considered global. The sensitivity study performed in section 5.6 showed that aerodynamic efficiency increases sharply between $\chi = 0.3$ and the conventional tube-and-wing configuration, primarily because $\chi = 0.3$ marks the point at which the fuselage becomes fully enclosed within the fairing, which significantly reduces interference effects and allows the fuselage to generate lift. Although $\chi = 0.3$ showed the highest efficiency wing parameter analysis, this configuration also exhibited weaker longitudinal static stability and greater susceptibility to separation near the wing–fairing junction compared to more blended designs, due to a sharper change in curvature. When the efficiency and stability margins were considered, $\chi = 0.4$ emerged as the best compromise. However, due to the lack of a full optimization process and structural analysis, it is possible that similar values could offer comparable or even superior performance. This is due to the larger fairing sizes spreading the required load in the spanwise direction, which produces a smaller bending moment thus requiring a lighter structure, which would reduce fuel burn as well as lift-induced drag. Therefore, an adequate weight and structural analysis needs to be included to find an actual optimum.

In summary, this work has demonstrated that the hybridization factor provides a powerful and flexible means to explore the continuous design space between conventional and fully blended aircraft configurations. By coupling the hybridization factor with CST-based parameterization, the research established an application capable of combining modeling, analysis, and design iteration whilst using a simple parametric representation. The implementation of this new methodology allows for a more deliberate control on the amount of "blending", curvature and sizing of a BWB's geometry. While the present study focused on a specific hydrogen powered cargo configuration, the methodology is broadly applicable to other platforms, particularly as the aerospace industry transitions towards unconventional aircraft to address the ever-growing climate concerns.

6.1 Future Work

There are several opportunities that can extend this research and the capabilities of this new design framework. The first being the exploration of the model's capabilities in designing the wing-body fairing of conventional aircraft, as this study mainly focused on how to transition the fairing from a TAW to a BWB. This would involve looking deeper into the characteristics of conventional wing-body fairings and analyzing how this parameterization can facilitate aerodynamic improvements. This study focused mainly on high-subsonic cruise conditions at a moderate angle of attack. BWB configurations may experience leading-edge vortices at higher angles of attack, which may cause unwanted drag or instabilities. The fairing curvature at the fairing-wing transition strongly influences the creation of vortices at high α. Future CFD at higher α would be required to analyze the hybridization factors effect on stall and separation for take-off and landing. For the CFD analysis, a medium-fidelity vortex-lattice method with certain viscous capabilities was used. using a more advanced CFD solver, like a RANS, and a highly refined mesh would yield better results, especially if they can represent complex flow phenomena like shocks and shock-induced separation. Another important future step would be to find a method that can couple the CST shape factors to certain curvature requirements and constraints. Although this may limit the creation of certain aircraft configurations, it would greatly speed up the design process of typical TAW and BWB designs whilst also making them more robust. As 2-D CST has already proved itself to be a good parameterization for optimizations [71], moving this theory to 3-D could yield the same benefits. Therefore, this work would greatly benefit from the creation of a design optimization loop using this new parameterization, as it would reveal the value of the hybridization and shape factors to multi-disciplinary design optimizations and also produce a more precise value for χ for a given configuration. Implementing other optimization procedures, like an airfoil optimization for would be greatly beneficial, especially due to the specific needs of the center section of BWB aircraft. However, before an optimization loop can be created, the modelled must be thoroughly and properly constrained. Another interesting area of research would be the effect of the hybridization factor on control surface design and effectiveness. Control surfaces on BWB are still being extensively researched and finding ways where the geometry of the aircraft can alleviate certain control issues would be very valuable research.

Bibliography

[1] D. S. Lee, D. W. Fahey, A. Skowron, M. R. Allen, U. Burkhardt, Q. Chen, S. J. Doherty, S. Freeman, P. M. Forster, J. Fuglestvedt, A. Gettelman, R. R. De León, L. L. Lim, M. T. Lund, R. J. Millar, B. Owen, J. E. Penner, G. Pitari, M. J. Prather, R. Sausen, and L. J. Wilcox, "The contribution of global aviation to anthropogenic climate forcing for 2000 to 2018," *Atmospheric Environment*, vol. 244, 1 2021.

[2] European Comission, "Reducing emissions from aviation." [Online]. Available: https://climate.ec.europa.eu/eu-action/transport-decarbonisation/reducing-emissions-aviation_en

[3] F. Franke, S. Kazula, and L. Enghardt, "Elaboration and outlook for metal hydride applications in future hydrogen-powered aviation," *Aeronautical Journal*, vol. 128, no. 1325, pp. 1501–1531, 7 2024.

[4] A. Gonzalez-Garay, C. Heuberger-Austin, X. Fu, M. Klokkenburg, D. Zhang, A. van der Made, and N. Shah, "Unravelling the potential of sustainable aviation fuels to decarbonise the aviation sector," *Energy and Environmental Science*, vol. 15, no. 8, pp. 3291–3309, 6 2022.

[5] Z. CHEN, M. ZHANG, Y. CHEN, W. SANG, Z. TAN, D. LI, and B. ZHANG, "Assessment on critical technologies for conceptual design of blended-wing-body civil aircraft," *Chinese Journal of Aeronautics*, vol. 32, no. 8, pp. 1797–1827, 8 2019.

[6] J. R. Chambers, "INNOVATION IN FLIGHT: RESEARCH OF THE NASA LANGLEY RESEARCH CENTER ON REVOLUTIONARY ADVANCED CONCEPTS FOR AERONAUTICS," Tech. Rep.

[7] R. H. Liebeck, "Design of the Blended Wing Body Subsonic Transport," Tech. Rep. 1, 2001.

[8] V. F. Wilod Versprille, "Aerodynamic Shape Op-timization of a Liquid-Hydrogen-Powered Blended-Wing-Body," Tech. Rep. [Online]. Available: http://repository.tudelft.nl/.

[9] R. H. Liebeck, M. A. Page, and B. K. Rawdon, "Blended-Wing-Body subsonic commercial transport," in *36th AIAA Aerospace Sciences Meeting and Exhibit*. American Institute of Aeronautics and Astronautics Inc, AIAA, 1998.

[10] K. Chen, X. Wang, P. Li, and J. Xie, "Modeling and evaluating passenger evacuation and risk in blended wing body aircraft using continuous displacement agents," *Discover Applied Sciences*, vol. 7, no. 1, 1 2025.

[11] R. Wittmann, "PASSENGER ACCEPTANCE OF BWB CONFIGURATIONS," 2004.

[12] P. Okonkwo and H. Smith, "Review of evolving trends in blended wing body aircraft design," pp. 1–23, 4 2016.

[13] D. Di Pasquale, D. Verma, and G. Pagliuca, "BLENDED WING BODY (BWB) PLANFORM MULTIDISCIPLINARY OPTIMISATION (MDO) FOR EARLY STAGE AIRCRAFT DESIGN USING MODEL BASED ENGINEERING," Tech. Rep.

[14] M. Brown and R. Vos, "Conceptual design and evaluation of blended-wing-body aircraft," in *AIAA Aerospace Sciences Meeting, 2018*. American Institute of Aeronautics and Astronautics Inc, AIAA, 2018.

[15] M. Johnson and H. Patel, "Blended Wing Body Multi-Discipline Model Development for MBSA&E Final Report," Tech. Rep., 2025. [Online]. Available: http://www.sti.nasa.gov

[16] D. P. Raymer, “Aircraft Design-A Conceptual Approach,” 1989.

[17] S. L. Yang, M. A. Page, and E. J. Smetak, “Achievement of NASA new aviation horizons N+2 goals with a blended-wing-body X-plane designed for the regional jet and single-aisle jet markets,” in *AIAA Aerospace Sciences Meeting, 2018*. American Institute of Aeronautics and Astronautics Inc, AIAA, 2018.

[18] W. Zhu, X. Yu, and Y. Wang, “Layout Optimization for Blended Wing Body Aircraft Structure,” *International Journal of Aeronautical and Space Sciences*, vol. 20, no. 4, pp. 879–890, 12 2019.

[19] R. Vos, F. J. Geuskens, and M. F. Hoogreef, “A new structural design concept for blended wing body cabins,” in *Collection of Technical Papers - AIAA/ASME/ASCE/AHS/ASC Structures, Structural Dynamics and Materials Conference*, 2012.

[20] T. R. Landis, “A Look Back: Northrop Flying Wings Part 1,” Tech. Rep.

[21] J. Baugher, “Northrop B-35.” [Online]. Available: https://www.joebaugher.com/usaf_bombers/b35.html

[22] B. I. Larrimer, “Beyond Tube-and-Wing,” 2020.

[23] “Burgess-Dunne-FlyingWing .” [Online]. Available: http://www.fiddlersgreen.net/models/aircraft/Burgess-Dunne-FlyingWing.html

[24] B. Lockett, “Northrop N9M-B Flying Wing.” [Online]. Available: https://www.air-and-space.com/Northrop%20N9M-B%20Flying%20Wing.htm

[25] P. J. Hoe and N. A. R. Nik Mohd, “Numerical prediction of blended wing body aerodynamic characteristics at subsonic speed,” *Jurnal Teknologi*, vol. 71, no. 2, pp. 65–69, 2014.

[26] A. Basyirah, A. Muta’ali, R. Effendy, M. Nasir, W. Wisnoe, and W. Kuntjoro, “Aerodynamic Performance of a Tail-less Blended Wing-Body Small Transport Aircraft,” *Journal of Advanced Research in Fluid Mechanics and Thermal Sciences Journal homepage*, vol. 66, pp. 135–150, 2020. [Online]. Available: www.akademiabaru.com/arfmts.html

[27] S. Dakka and O. Johnson, “Aerodynamic design and exploration of a blended wing body aircraft at subsonic speed,” *International Journal of Aviation, Aeronautics, and Aerospace*, vol. 6, no. 5, 2019.

[28] J. Van Dommelen and R. Vos, “Conceptual design and analysis of blended-wing-body aircraft,” *Proceedings of the Institution of Mechanical Engineers, Part G: Journal of Aerospace Engineering*, vol. 228, no. 13, pp. 2452–2474, 11 2014.

[29] J. I. Hileman, Z. S. Spakovszky, M. Drela, M. A. Sargeant, and A. Jones, “Airframe design for silent fuel-efficient aircraft,” *Journal of Aircraft*, vol. 47, no. 3, pp. 956–969, 2010.

[30] R. H. Thomas, C. L. Burley, L. V. Lopes, C. J. Bahr, F. H. Gern, and D. E. Van Zante, “System noise assessment and the potential for a low noise hybrid wing body aircraft with open rotor propulsion,” in *52nd Aerospace Sciences Meeting*. American Institute of Aeronautics and Astronautics Inc., 2014.

[31] K. Sun, W. Wang, R. Cheng, Y. Liang, H. Xie, J. Wang, and M. Zhang, “Evolutionary generative design of supercritical airfoils: an automated approach driven by small data,” *Complex and Intelligent Systems*, vol. 10, no. 1, pp. 1167–1183, 2 2024.

[32] U. Ali, M. Okasha, T. N. Dief, M. S. ElSayed, and M. M. Kamra, “Blended wing body designs for aerodynamic, stability, and control optimization: A comprehensive review,” 12 2025.

[33] G. L. Rocca and F. Dircken, “Controllability Of Blended Wing Body,” Tech. Rep.

[34] V. Mukhopadhyay, “Structural Concepts Study of Non-circular Fuselage Configurations,” Tech. Rep., 1996. [Online]. Available: https://www.researchgate.net/publication/2294002

[35] S. Hwan Cho, C. Bil, and J. Bayandor, “BWB MILITARY CARGO TRANSPORT FUSELAGE DESIGN AND ANALYSIS,” 2008.

[36] E. Obert, "AERODYNAMIC DESIGN OF TRANSPORT AIRCRAFT," Tech. Rep.

[37] Olivier Cleynen, "Wing-fuselage fairing of an Airbus A320," 12 2016.

[38] S. Xu, S. Timme, O. Mykhaskiv, and J. D. Müller, "Wing-body junction optimisation with CAD-based parametrisation including a moving intersection," *Aerospace Science and Technology*, vol. 68, pp. 543–551, 9 2017.

[39] E. C. Polhamus, "A CONCEPT OF THE VORTEX LIFT OF SHARP-EDGE DELTA WINGS BASED ON A LEADING-EDGE-SUCTION ANALOGY," Tech. Rep.

[40] Z. Lyu and J. R. Martins, "Aerodynamic design optimization studies of a blended-wing-body aircraft," in *Journal of Aircraft*, vol. 51, no. 5. American Institute of Aeronautics and Astronautics Inc., 9 2014, pp. 1604–1617.

[41] S. Karpuk, Y. Ma, and A. Elham, "Design Investigation of Potential Long-Range Hydrogen Combustion Blended Wing Body Aircraft with Future Technologies," *Aerospace*, vol. 10, no. 6, 6 2023.

[42] E. J. Adler and J. R. R. A. Martins, "Blended wing body configuration for hydrogen-powered aviation," Tech. Rep. [Online]. Available: https://github.com/mdolab/openconcept

[43] K. Suzuki, S. E. Phenisee, and M. Salviato, "REPORT: Investigation on Curvilinear Anisotropy via Isogeometric Analysis (IGA)," 9 2020. [Online]. Available: http://arxiv.org/abs/2009.10230

[44] Y. Liang, X. Q. Cheng, Z. N. Li, and J. W. Xiang, "Multi-objective robust airfoil optimization based on non-uniform rational B-spline(NURBS) representation," *Science China Technological Sciences*, vol. 53, no. 10, pp. 2708–2717, 2010.

[45] H. Sobieczky, "Parametric Airfoils and Wings," Tech. Rep., 1998.

[46] P. Della Vecchia, E. Daniele, and E. D'Amato, "An airfoil shape optimization technique coupling PARSEC parameterization and evolutionary algorithm," *Aerospace Science and Technology*, vol. 32, no. 1, pp. 103–110, 1 2014.

[47] H. Sobieczky, "Knowledge Based Aerodynamic Optimization," Tech. Rep. [Online]. Available: http://www.as.dlr.de/hs/

[48] H. M. Sheikh, S. Lee, J. Wang, and P. S. Marcus, "Airfoil optimization using Design-by-Morphing," *Journal of Computational Design and Engineering*, vol. 10, no. 4, pp. 1443–1459, 8 2023.

[49] M. Ceze, M. Hayashiy, and E. Volpez, "A study of the CST parameterization characteristics," in *Collection of Technical Papers - AIAA Applied Aerodynamics Conference*. American Institute of Aeronautics and Astronautics Inc., 2009.

[50] B. M. Kulfan and J. E. Bussoletti, "1th AIAA/ISSMO Multidisciplinary Analysis and Optimization Conference: The Modeling and Simulation Frontier for Multidisciplinary Design Optimization "Fundamental" Parametric Geometry Representations for Aircraft Component Shapes "Fundamental" Parametric Geometry Representations for Aircraft Component Shapes," Tech. Rep.

[51] N. Khailany, P. R. Mokotoff, and G. Cinar, "Aircraft Geometry and Propulsion Architecture Visualization for the Future Aircraft Sizing Tool (FAST)," in *AIAA Science and Technology Forum and Exposition, AIAA SciTech Forum 2025*. American Institute of Aeronautics and Astronautics Inc, AIAA, 2025.

[52] E. D. Olson, "Three-Dimensional Piecewise-Continuous Class-Shape Transformation of Wings," Tech. Rep.

[53] A. Bentamy, J.-Y. Trépanier, and F. Guibault, "WING SHAPE OPTIMIZATION USING A CONSTRAINED NURBS SURFACE GEOMETRICAL REPRESENTATION," Tech. Rep., 2002. [Online]. Available: http://www.cerca.umontreal.ca/pirate/

[54] L. Piegl and Tiller W, "Springer-TheNURBSBook," 1997.

[55] L. Piegl, "On NURBS: A Survey," Tech. Rep., 1991.

[56] B. Abou and E. Majd, "Parameterization adaption for 3D shape optimization in aerodynamics," Tech. Rep.

[57] J. A. Samareh, "Aerodynamic Shape Optimization Based on Free-form Deformation," Tech. Rep. [Online]. Available: http://mdob.larc.nasa.gov,

[58] R. Vos, "D R A F T AIRPLANE DESIGN AND ANALYSIS," Tech. Rep.

[59] K. A. Lane ′ and D. D. Marshall, "A Surface Parameterization Method for Airfoil Optimization and High Lift 2D Geometries Utilizing the CST Methodology," Tech. Rep., 2009.

[60] J. Gallier, "Geometric Methods and Applications," 2011.

[61] D. Darling, "Superellipse," 2016.

[62] N. S. Currey, "Aircraft Landing Gear Design: Principles and Practices," Tech. Rep., 1988.

[63] J. D. Anderson and M. L. Bowden, *Introduction to flight*. McGraw Hill LLC, 2022.

[64] Altair Engineering, "FlightStream Theory Manual," 2024.

[65] Airbus, "Orders and Deliveries since the creation of Airbus," Tech. Rep., 2025.

[66] J. Mukhopadhaya and D. Rutherford, "PERFORMANCE ANALYSIS OF EVOLUTIONARY HYDROGEN-POWERED AIRCRAFT," Tech. Rep., 2022. [Online]. Available: www.theicct.orgcommunications@theicct.org

[67] B van der Zalm, "Weight and performance calculations for the Airbus A320-200 (CFM56 engines)," 10 2022.

[68] M. Orlita and R. Vos, "Cruise performance optimization of the airbus A320 through flap morphing," in *17th AIAA Aviation Technology, Integration, and Operations Conference, 2017*. American Institute of Aeronautics and Astronautics Inc, AIAA, 2017.

[69] H. GÜZELBEY, Y. ERASLAN, and M. H. DOĞRU, "Effects of Taper Ratio on Aircraft Wing Aerodynamic Parameters: A Comperative Study," *European Mechanical Science*, vol. 3, no. 1, pp. 18–23, 3 2019.

[70] M. P. Fink, "Full-scale investigation of the aerodynamic characteristics of a sailwing of aspect ratio 5.9," *NASA*, 1969.

[71] M. T. Akram and M. H. Kim, "CFD analysis and shape optimization of airfoils using class shape transformation and genetic algorithm—part i," *Applied Sciences (Switzerland)*, vol. 11, no. 9, 5 2021.

Appendix A

Appendix A: Validation Results

A.1 EMB-145

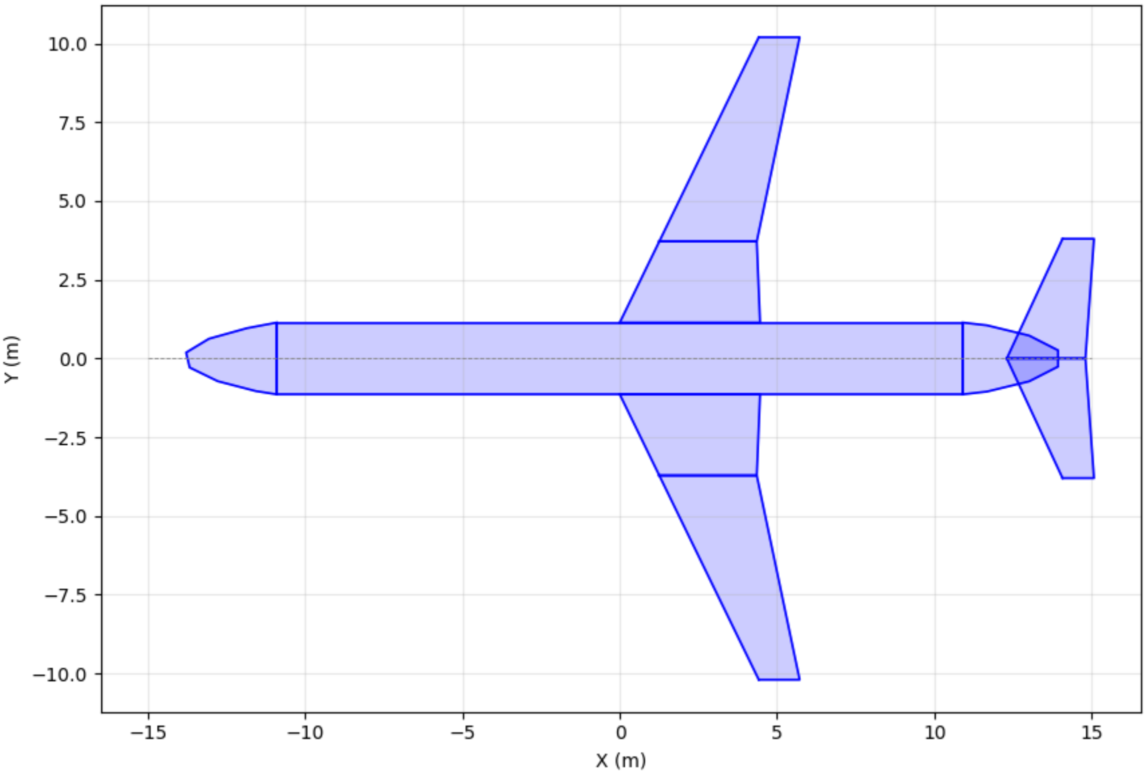

Figure A.1: EMB-145: Reference top planform

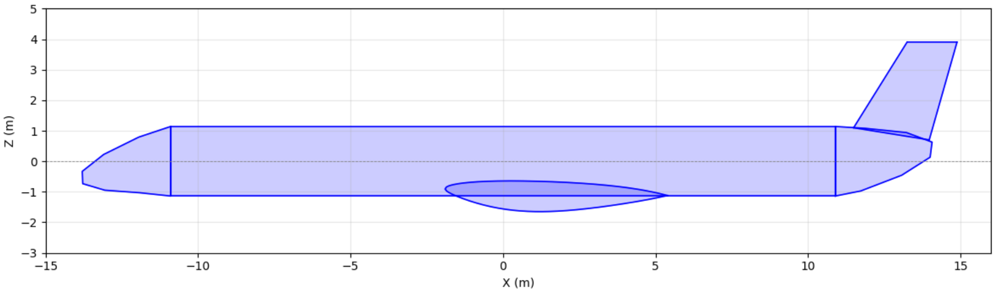

Figure A.2: EMB-145: Reference side planform

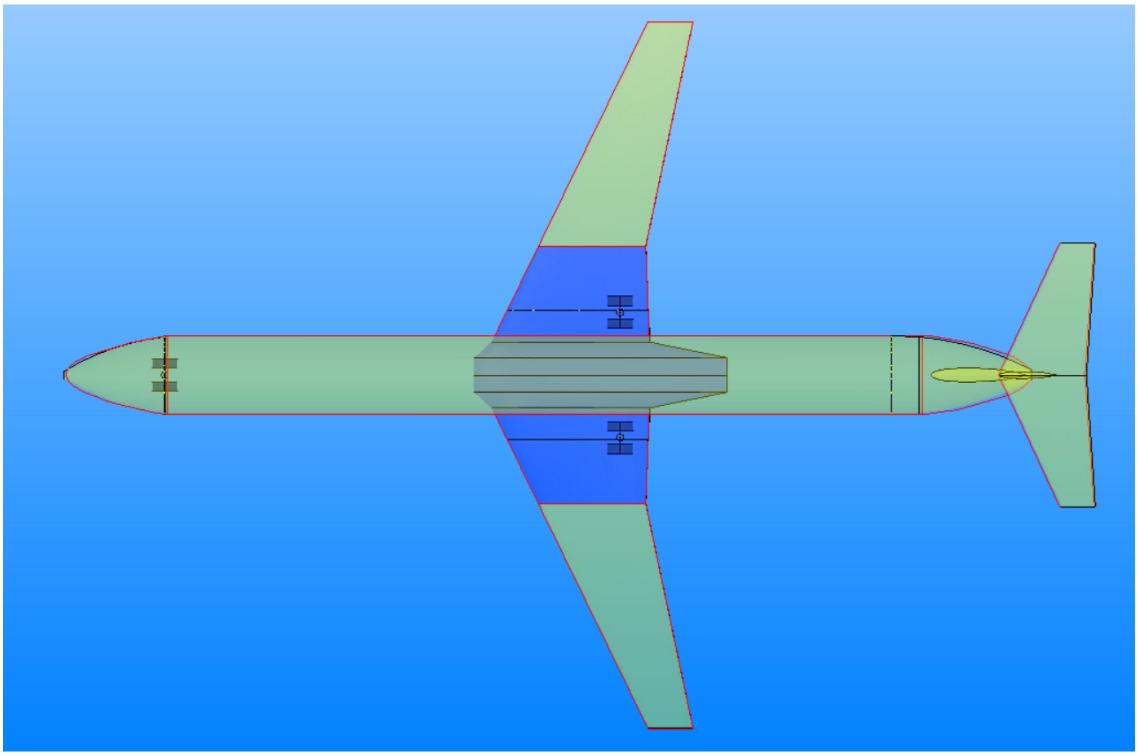

Figure A.3: EMB-145: Top planform validation

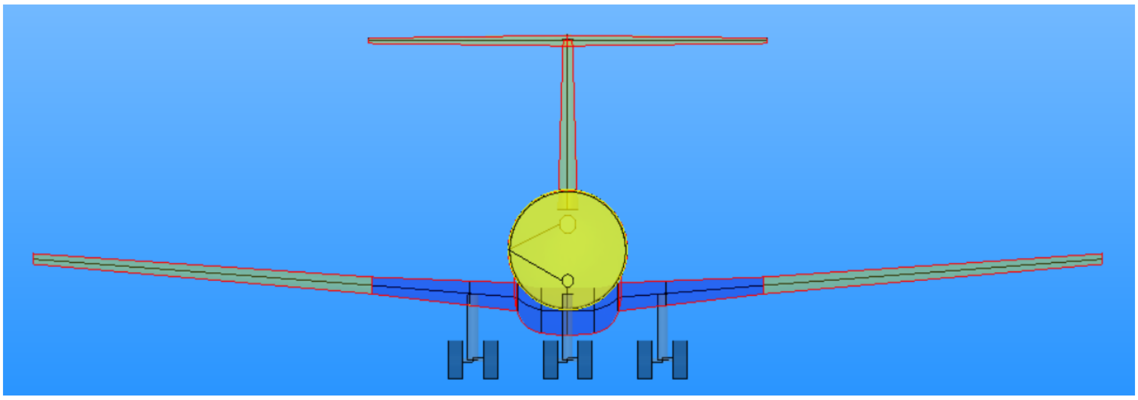

Figure A.4: EMB-145: Front planform validation

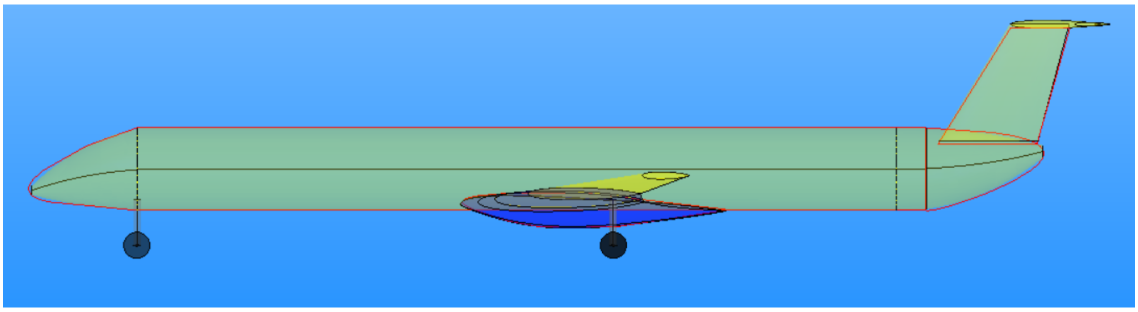

Figure A.5: EMB-145: Side planform validation

Table A.1: Inputs of the EMB145 validator

Input	Value	Unit
chi	0.365	[-]
slender factor	0.7	[-]
wing span	20.4	m
wing sweep	26	deg
wing vertical position	-0.94	m
Υ_i	[1.1, 0.255, 0.5]	[-]
c_{root}	7.2	m
c_{tip}	1.3	m
t_{root}	0.35	[-]
t_{tip}	0.2	[-]
root incidence	1.5	deg
twist	0	deg
dihedral	4.45	deg
a_c	[0.875, 2.775, 2.9125, 2.21]	[-]
a_t	[3.1, 2.85, 2, 1.435]	[-]
a_i	[0.0, 0.05, 0.02, 0.01]	[-]
a_x	[-0.05, 1.65, -1.65, 0]	[-]
a_z	[0, -0.025, 0, 0]	[-]
$a_{U,\text{root}}$	[0.2, 0.18, 0.15, 0.35]	[-]
$a_{L,\text{root}}$	[-0.175, -0.65, -0.35, -0.45]	[-]
a_U	[0.25, 0.25, 0.25, 0.45]	[-]
a_L	[-0.25, -0.25, -0.25, -0.45]	[-]
h_{min}	1.85	m
fuselage position	-9	m
fuselage rotation	0	deg
fuselage vertical position	0	m
fuselage roundness	2	[-]
fuselage length	21	m
κ	-0.24	[-]
ν	1.1	m
nose spacing factor	3.5	[-]
nose displacement	-0.55	m
nose tip height	0.29	m
nose profiles	42	[-]
nose scale	0.05	[-]
nose tail roundness	2	[-]
tail spacing factor	3.9	[-]
tail displacement	0.2	m
tail tip height	0.25	m
tail profiles	40	[-]
tail scale	0.05	[-]

A.2 A320

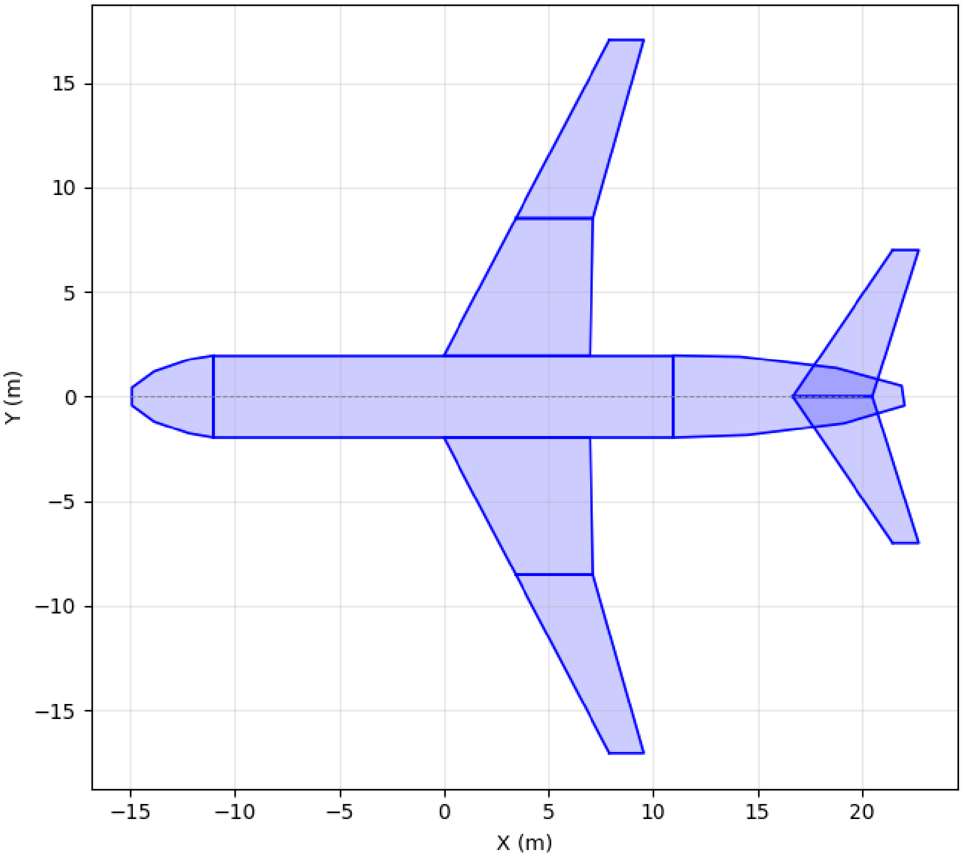

Figure A.6: A320: Reference top planform

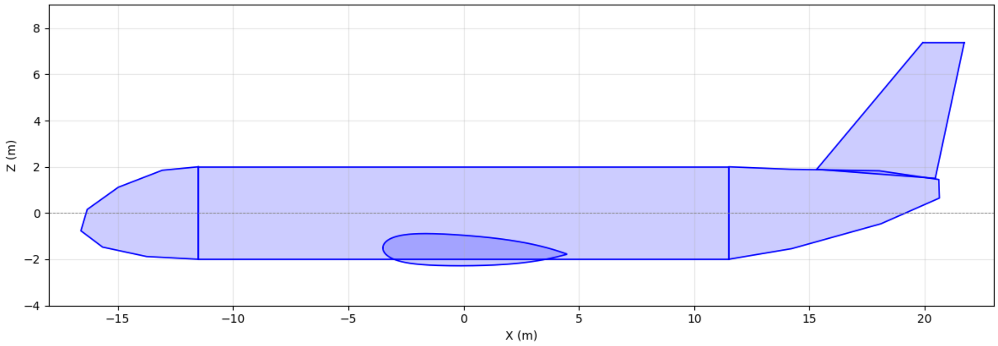

Figure A.7: A320: Reference side planform

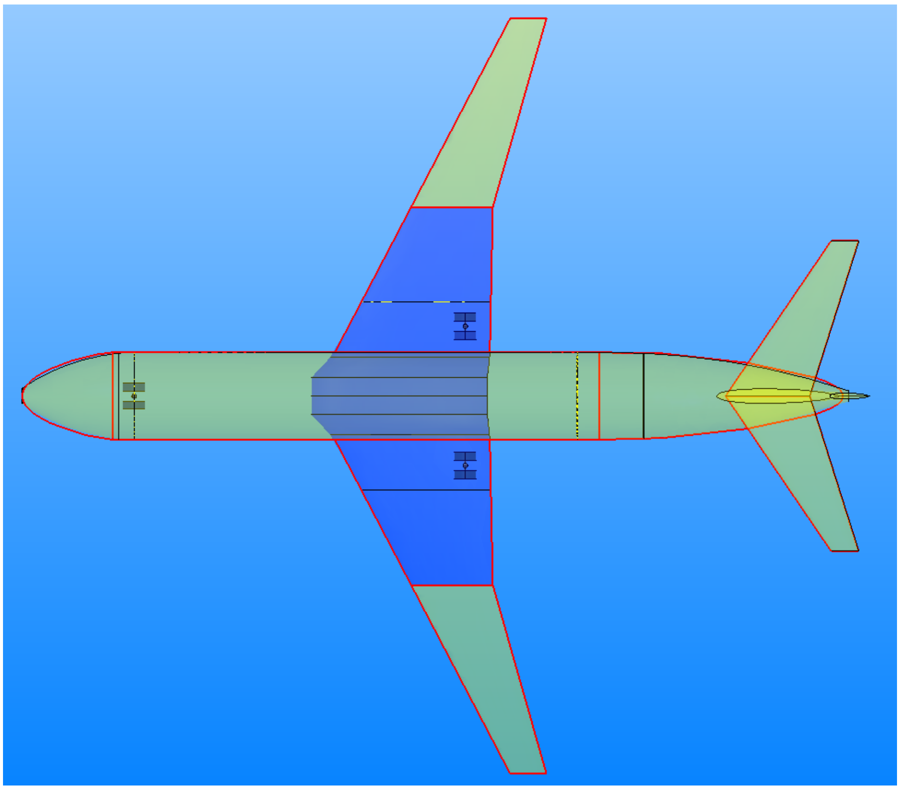

Figure A.8: A320: Top planform validation

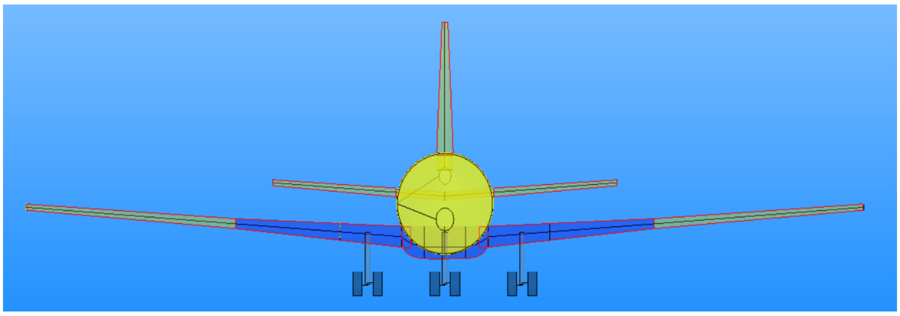

Figure A.9: A320: Front planform validation

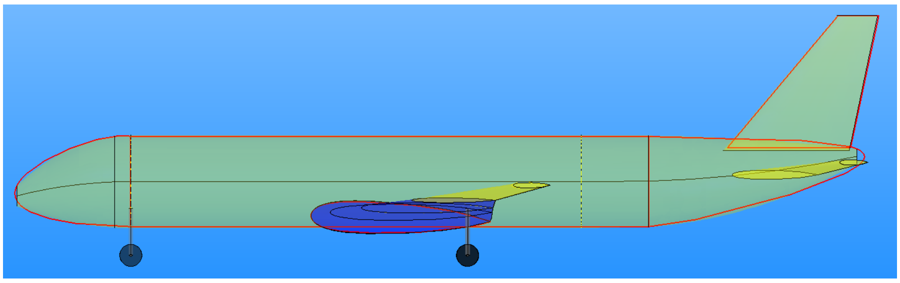

Figure A.10: A320: Side planform validation

Table A.2: Inputs of the A320 validator

Input	Value	Unit
chi	0.5	[-]
slender factor	0.85	[-]
wing span	34.09	m
wing sweep	27.7	deg
wing vertical position	-1.5	m
Y_i	[0.275, 0.205, 0.5]	[-]
c_{root}	6.07	m
c_{tip}	1.64	m
t_{root}	3	[-]
t_{tip}	0.246	[-]
root incidence	2	deg
twist	0	deg
dihedral	4.55	deg
a_c	[0, 4, -1.075, 0.75]	[-]
a_t	[0.25, 0.6, 0.0, 0.15]	[-]
a_i	[0.0, 0.05, 0.02, 0.01]	[-]
a_x	[0, 2.95, -2.95, 0]	[-]
a_z	[0, 0.04, 0, 0]	[-]
$a_{U,\text{root}}$	[0.33, 0.25, 0.25, 0.45]	[-]
$a_{L,\text{root}}$	[-0.33, -0.25, -0.25, -0.395]	[-]
a_U	[0.25, 0.25, 0.25, 0.45]	[-]
a_L	[-0.25, -0.25, -0.25, -0.45]	[-]
h_{min}	3.7	m
fuselage position	-8	m
fuselage rotation	0	deg
fuselage vertical position	0	m
fuselage roundness	2	[-]
fuselage length	20	m
κ	-0.35	[-]
ν	1	m
nose spacing factor	5	[-]
nose displacement	0.1	m
nose tip height	0.2	m
nose profiles	65	[-]
nose scale	0.05	[-]
nose tail roundness	2	[-]
tail spacing factor	10.25	[-]
tail displacement	1.725	m
tail tip height	0.325	m
tail profiles	70	[-]
tail scale	0.05	[-]

A.3 D8

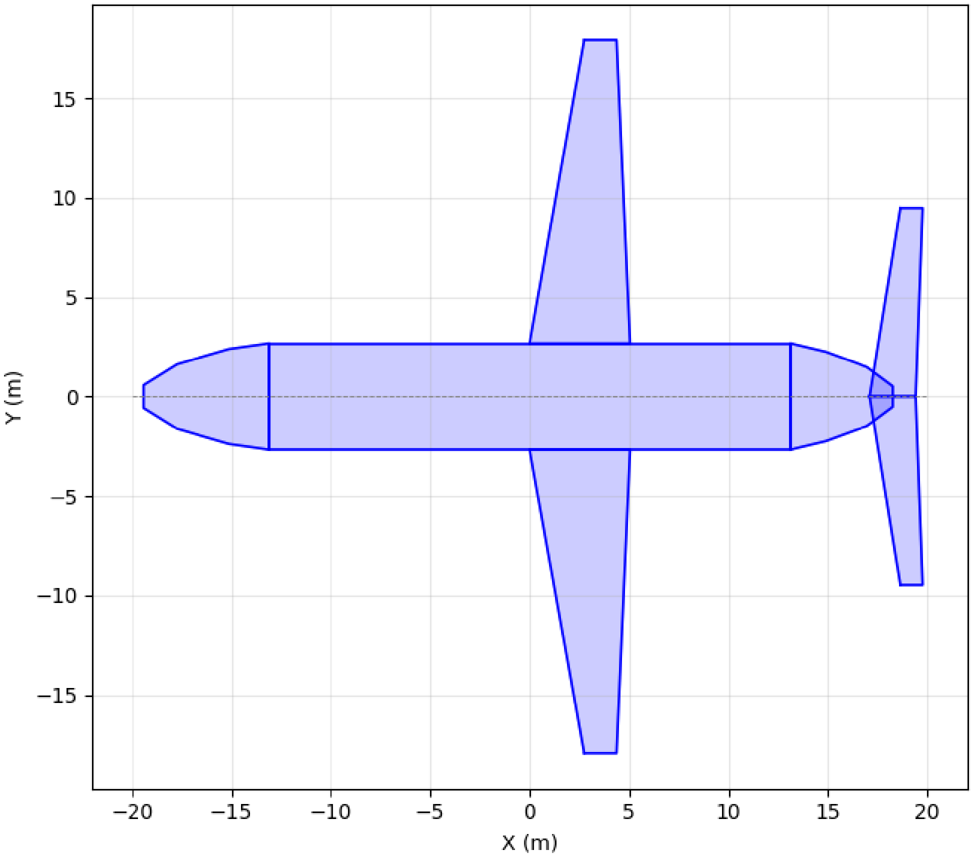

Figure A.11: D8: Reference top planform

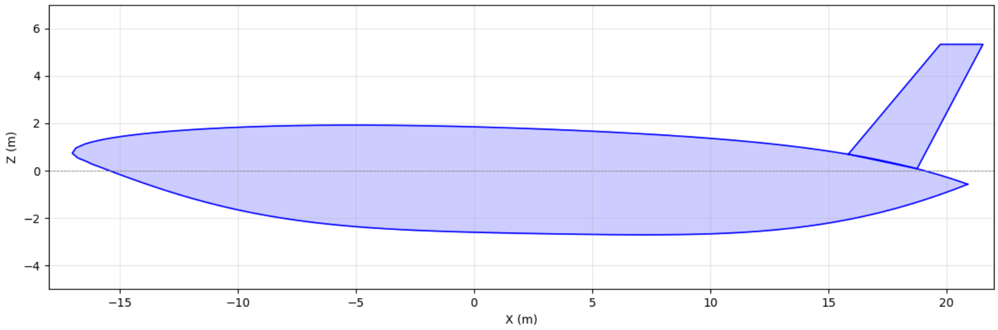

Figure A.12: D8: Reference side planform

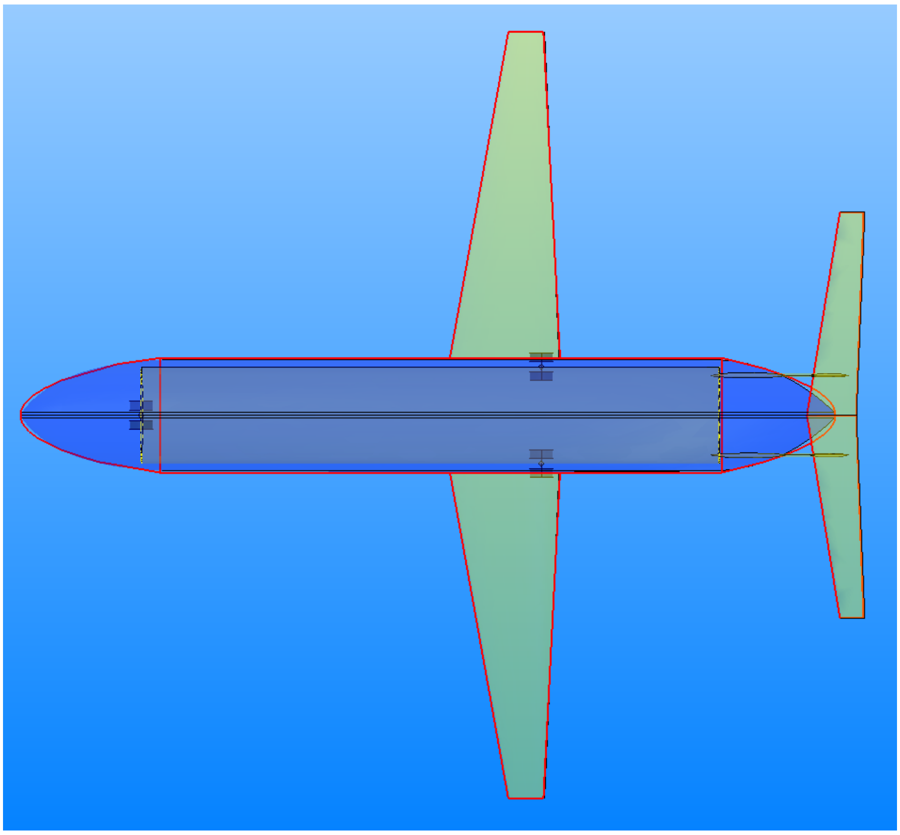

Figure A.13: D8: Top planform validation

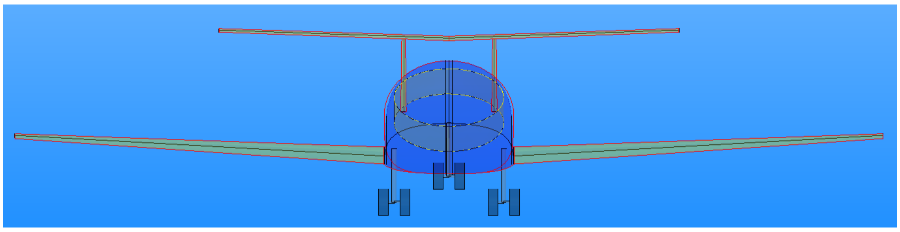

Figure A.14: D8: Front planform validation

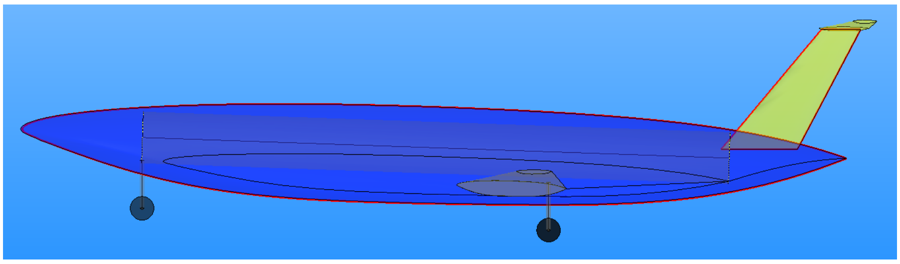

Figure A.15: D8: Side planform validation

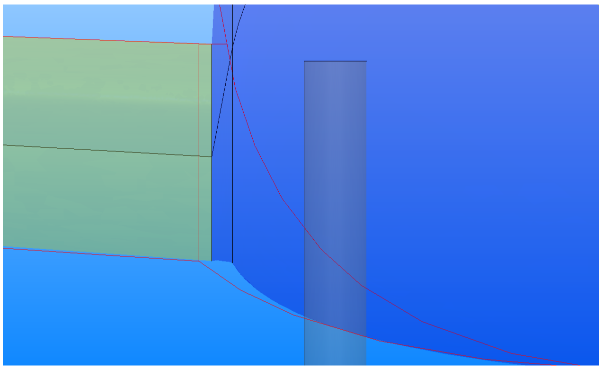

Figure A.16: D8: Fairing curvature error

Table A.3: Inputs of the D8 validator

Input	Value	Unit
chi	0.1485	[-]
slender factor	-0.5	[-]
wing span	35.814	m
wing sweep	10.15	deg
wing vertical position	-2.3	m
Y_i	[0.3, 0.5, 0.975]	[-]
c_{root}	37.98	m
c_{tip}	1.64	m
t_{root}	22	[-]
t_{tip}	1.275	[-]
root incidence	0	deg
twist	0	deg
dihedral	4.8	deg
a_c	[0, -9, 13, 0.215]	[-]
a_t	[0.455, -7.45, 11.5, 0.15]	[-]
a_i	[2, 2, 2, 2]	[-]
a_x	[-0.29, -0.85, 5.15, 0]	[-]
a_z	[1.68, 1.565, 1.675, 0.3]	[-]
$a_{U,\text{root}}$	[0.1125, 0.125, 0.15, 0.15, 0.2, 0.4]	[-]
$a_{L,\text{root}}$	[-0.075, -0.3, -0.25, -0.15, -0.425, -0.55]	[-]
a_U	[0.1125, 0.125, 0.15, 0.15, 0.2, 0.4]	[-]
a_L	[-0.075, -0.3, -0.25, -0.15, -0.425, -0.55]	[-]
h_{min}	2.8	m
fuselage position	-14	m
fuselage rotation	2	deg
fuselage vertical position	0.2	m
fuselage roundness	2	[-]
fuselage length	27	m
κ	0	[-]
ν	1	m

A.4 Delft BWB

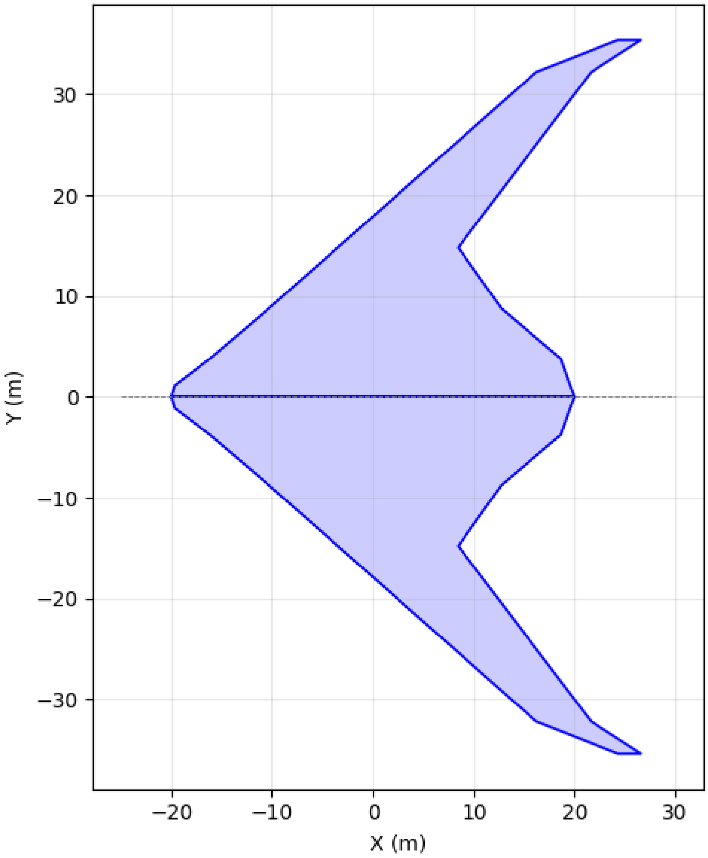

Figure A.17: Delft BWB: Reference top planform

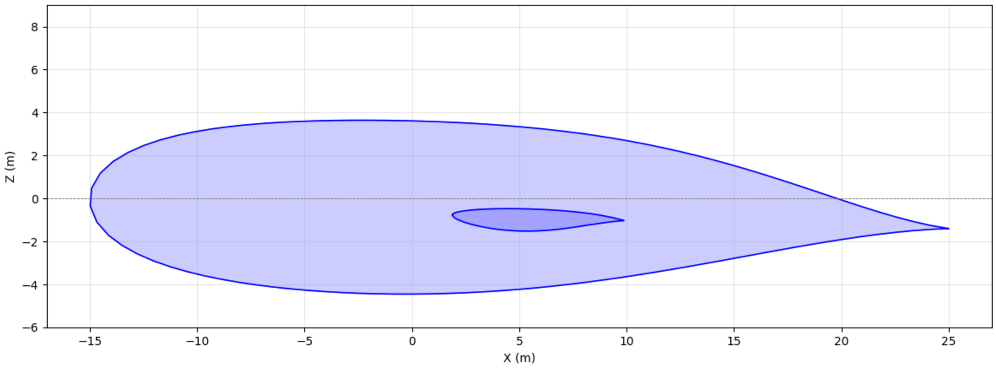

Figure A.18: Delft BWB: Reference side planform

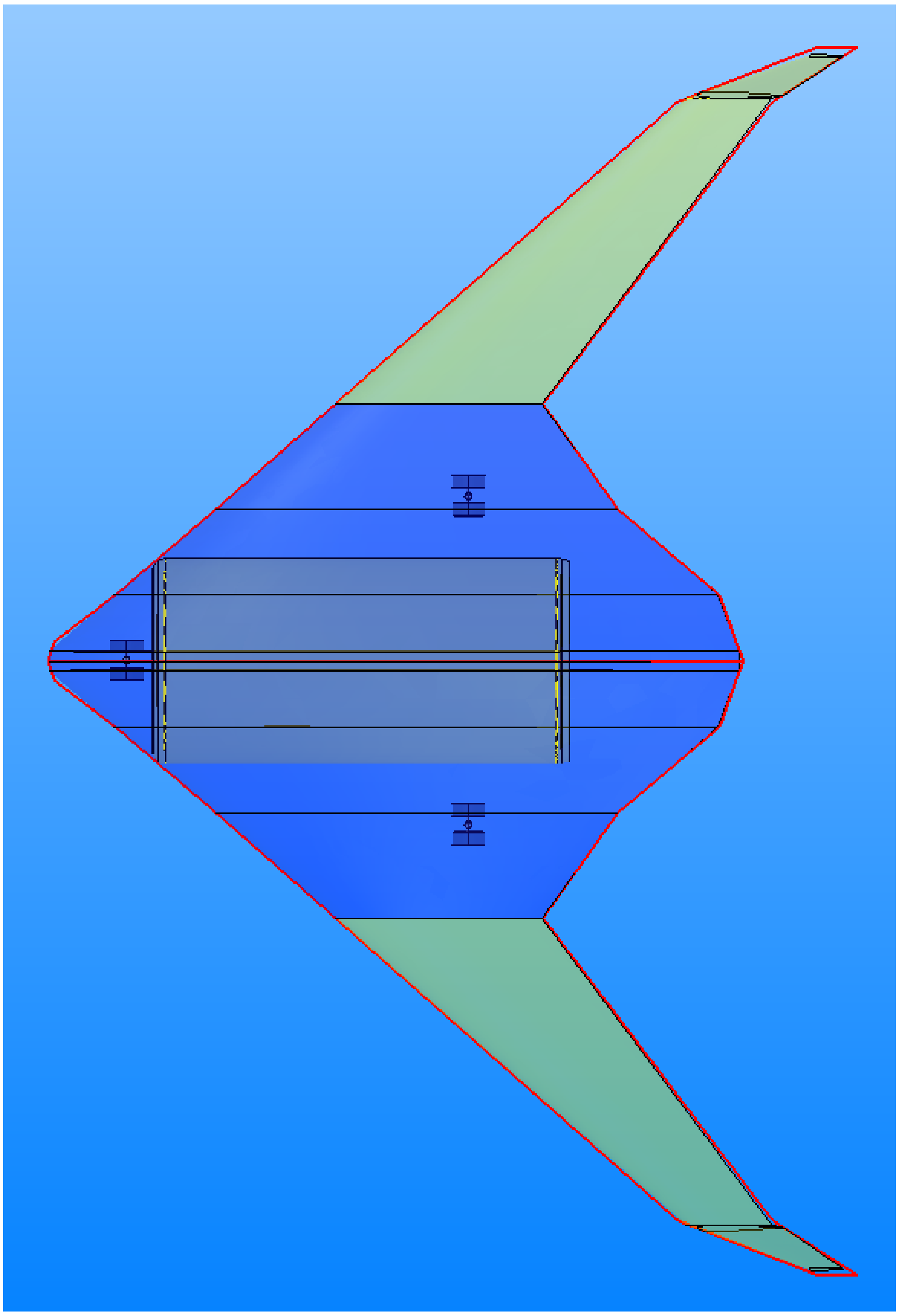

Figure A.19: Delft BWB: Top planform validation

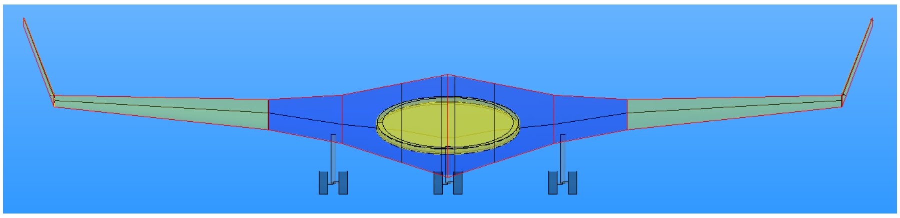

Figure A.20: Delft BWB: Front planform validation

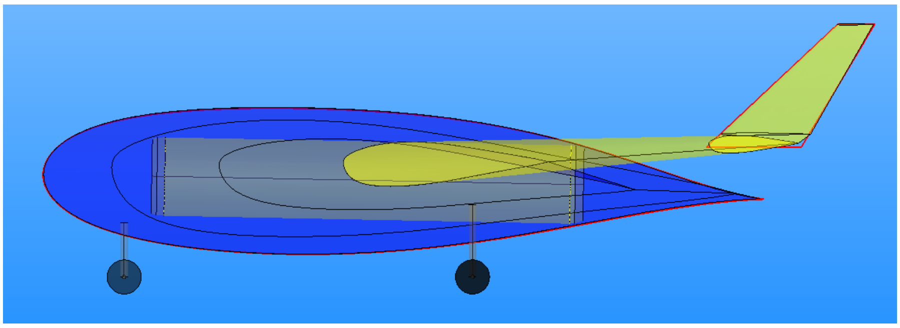

Figure A.21: Delft BWB: Side planform validation

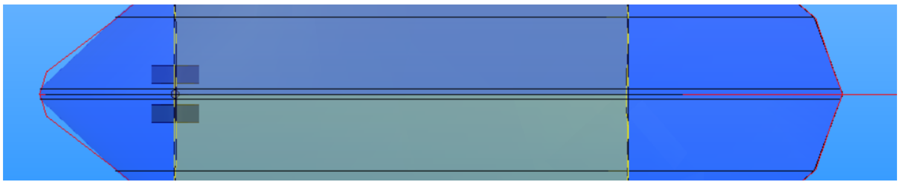

Figure A.22: Delft BWB: Discrepancies at nose and tail

Table A.4: Inputs of the DelftBWB validator

Input	Value	Unit
chi	0.4565	[-]
slender factor	-3	[-]
wing span	59	m
wing sweep	48.5	deg
wing vertical position	0	m
Y_i	[0.6, 0.2575, 0.59]	[-]
c_{root}	40	m
c_{tip}	5.2	m
t_{root}	12	[-]
t_{tip}	4	[-]
root incidence	2	deg
twist	0	deg
dihedral	3	deg
a_c	[-0.015, 11.125, -1.45, 1.55]	[-]
a_t	[15.75, 8, 5.85, 2.85]	[-]
a_i	[0.0, 4.5, 5.5, 0.01]	[-]
a_x	[0.015, 2.75, -0.675, -0.1]	[-]
a_z	[0.01, 0.25, 0.2, -0.05]	[-]
$a_{U,\text{root}}$	[0.2, 0.175, 0.175, 0.2, 0.3, 0.075]	[-]
$a_{L,\text{root}}$	[-0.2, -0.175, -0.175, -0.2, -0.15, -0.05]	[-]
a_U	[0.2, 0.25, 0.25, 0.25, 0.125, 0.25]	[-]
a_L	[-0.425, -0.25, -0.29, -0.265, -0.125, -0.25]	[-]
h_{min}	6	m
fuselage position	6.75	m
fuselage rotation	1.125	deg
fuselage vertical position	0	m
fuselage roundness	2	[-]
fuselage length	22.55	m
κ	0	[-]
ν	0	m

Appendix B

Helper Classes

B.1 AirfoilCurve Class

Listing B.1: AirfoilCurve

```python

from parapy.geom import *
from parapy.core import *
from parapy.gui import display
from math import radians, comb
import numpy as np


class AirfoilCurve(FittedCurve):

    N1 = Input(0.5)
    N2 = Input(1)
    aU = Input([0.25, 0.25, 0.25, 0.45])
    aL = Input([-0.25, -0.25, -0.25, -0.45])
    chord = Input(2)
    tc = Input(1)
    twist = Input(0)

    # Translation and rotation inputs
    x_translation = Input(0)
    y_translation = Input(0)
    z_translation = Input(0)
    x_rotation = Input(0)  # rotation about x-axis ( y z  plane)

    # Optional rotation center in y-z plane
    x_rotation_center_y = Input(None)
    x_rotation_center_z = Input(None)

    num_psi_vals = Input(100) # number of points defining airfoil
    tolerance = Input(0.001)

    def bernstein(self, n, j, x):
        return comb(n, j) * (x ** j) * ((1 - x) ** (n - j))

    @Attribute
    def points(self):
        psi_vals = np.linspace(0, 1, self.num_psi_vals)
        S_U, S_L = np.zeros_like(psi_vals), np.zeros_like(psi_vals)

```

```
        n_coef = len(self.aU)
        for j in range(n_coef):
            B = self.bernstein(n_coef - 1, j, psi_vals)
            S_U += self.aU[j] * B
            S_L += self.aL[j] * B

        C_vals = psi_vals ** self.N1 * (1 - psi_vals) ** self.N2
        z_u = self.tc * C_vals * S_U
        z_l = self.tc * C_vals * S_L

        x_coords = psi_vals * self.chord
        theta = radians(self.twist)      # rotation about y-axis
        phi = radians(self.x_rotation)   # rotation about x-axis

        # Apply twist rotation in  x z  plane
        x_u = x_coords * np.cos(theta) + z_u * np.sin(theta)
        z_u = z_u * np.cos(theta) - x_coords * np.sin(theta)
        x_l = x_coords * np.cos(theta) + z_l * np.sin(theta)
        z_l = z_l * np.cos(theta) - x_coords * np.sin(theta)

        y_u = np.zeros_like(x_u)
        y_l = np.zeros_like(x_l)

        # Determine rotation center in local (y,z)
        rot_cy = 0.0 if self.x_rotation_center_y is None else float(self.
            x_rotation_center_y)

        if self.x_rotation_center_z is not None:
            rot_cz = float(self.x_rotation_center_z)
        else:
            mean_z_u = np.mean(z_u) if z_u.size else 0.0
            mean_z_l = np.mean(z_l) if z_l.size else 0.0
            rot_cz = 0.5 * (mean_z_u + mean_z_l)

        # Translate y and z so rotation axis is centered
        y_u_shift = y_u - rot_cy
        z_u_shift = z_u - rot_cz
        y_l_shift = y_l - rot_cy
        z_l_shift = z_l - rot_cz

        # Apply x-axis rotation

        y_u_rot = y_u_shift * np.cos(phi) - z_u_shift * np.sin(phi)
        z_u_rot = y_u_shift * np.sin(phi) + z_u_shift * np.cos(phi)

        y_l_rot = y_l_shift * np.cos(phi) - z_l_shift * np.sin(phi)
        z_l_rot = y_l_shift * np.sin(phi) + z_l_shift * np.cos(phi)

        # Apply global translations
        y_u_final = y_u_rot + rot_cy + self.y_translation
        z_u_final = z_u_rot + rot_cz + self.z_translation

        y_l_final = y_l_rot + rot_cy + self.y_translation
        z_l_final = z_l_rot + rot_cz + self.z_translation

        x_u_final = x_u + self.x_translation
        x_l_final = x_l + self.x_translation

        pts_upper = [Point(x, y, z) for x, y, z in zip(x_u_final, y_u_final,
            z_u_final)]
        pts_lower = [Point(x, y, z) for x, y, z in zip(x_l_final, y_l_final,
```

```
            z_l_final)]

        return list(reversed(pts_lower)) + pts_upper

    @Attribute
    def area(self):
        """Calculate the enclosed area of the airfoil"""
        pts = self.points

        x = np.array([p.x for p in pts])
        z = np.array([p.z for p in pts])

        area = 0.5 * np.abs(np.dot(x, np.roll(z, 1)) - np.dot(z, np.roll(x, 1)))
        return area

    @Attribute
    def thickness(self):
        """Calculate maximum thickness of the airfoil"""
        psi_vals = np.linspace(0, 1, 200)
        S_U, S_L = np.zeros_like(psi_vals), np.zeros_like(psi_vals)

        n_coef = len(self.aU)
        for j in range(n_coef):
            B = self.bernstein(n_coef - 1, j, psi_vals)
            S_U += self.aU[j] * B
            S_L += self.aL[j] * B

        C_vals = psi_vals ** self.N1 * (1 - psi_vals) ** self.N2
        z_u = self.tc * C_vals * S_U
        z_l = self.tc * C_vals * S_L

        x_coords = psi_vals * self.chord
        theta = radians(self.twist)

        x_u = x_coords * np.cos(theta) + z_u * np.sin(theta)
        z_u = z_u * np.cos(theta) - x_coords * np.sin(theta)
        x_l = x_coords * np.cos(theta) + z_l * np.sin(theta)
        z_l = z_l * np.cos(theta) - x_coords * np.sin(theta)

        thickness = z_u - z_l
        return float(np.max(thickness))


    @Attribute
    def thickness_to_chord(self):
        return self.thickness/self.actual_chord


if __name__ == '__main__':
    obj = AirfoilCurve()
    display(obj)
```

B.2 LandingGear Class

Listing B.2: LandingGear

```

from parapy.geom import *
from parapy.core import *
```

```python
from parapy.gui import display
from math import radians

class LandingGear(GeomBase):

    strut_radius = Input(0.0025)
    strut_length = Input(0.04)
    wheel_radius = Input(0.01)
    # wheel_thickness = Input(0.01)

    @Attribute
    def axle_radius(self):
        return self.wheel_radius * 0.1

    @Attribute
    def axle_length(self):
        return 0.35*self.wheel_thickness + self.strut_radius

    @Attribute
    def wheel_thickness(self):
        return 0.75*self.wheel_radius

    @Attribute
    def tyre_profile_radius(self):
        return self.wheel_radius/4


    @Part
    def strut(self):
        return Cylinder(radius=self.strut_radius, height=self.strut_length, color=
            'gray')

    @Part
    def axle(self):
        return Cylinder(quantify=2, radius=self.axle_radius, height=self.
            axle_length,
                        position=rotate(self.position, 'y', radians(90)+radians
                            (180)*child.index), color='gray')

    @Part
    def wheel_center(self):
        return Cylinder(quantify=2, radius=self.wheel_radius, height=self.
            wheel_thickness,
                         position=translate(rotate(self.position, 'y', radians(90)
                             ),
                                            'z', self.axle_length-2*self.
                                                axle_length*child.index-self.
                                                wheel_thickness*child.index),
                        color='black'
                         )

if __name__ == '__main__':
    obj = LandingGear(label="LandingGear")
    display(obj)
```

B.3 HyperEllipse

Listing B.3: LandingGear

```python

from parapy.geom import *
from parapy.core import *
from parapy.gui import display
from math import radians, cos, sin
import numpy as np
from scipy.special import gamma

class HyperEllipse(FittedCurve):

    width = Input(1.0)
    height = Input(1.0)
    roundness = Input(2.0)
    n_points = Input(100)

    x_translation = Input(0)
    y_translation = Input(0)
    z_translation = Input(0)
    x_rotation = Input(0)
    y_rotation = Input(0)
    z_rotation = Input(0)

    continuity = 2

    def raw_points(self):
        """Superellipse points in XY-plane centered at origin"""
        a = self.width / 2
        b = self.height / 2
        n = self.roundness

        # Ensure n_points is a multiple of 4
        n_total = int(self.n_points)
        if n_total % 4 != 0:
            n_total += 4 - (n_total % 4)

        theta = np.linspace(0, 2 * np.pi, n_total, endpoint=False)
        cos_t = np.cos(theta)
        sin_t = np.sin(theta)

        x = a * np.sign(cos_t) * (np.abs(cos_t) ** (2.0 / n))
        y = b * np.sign(sin_t) * (np.abs(sin_t) ** (2.0 / n))

        # Close the curve by appending the first point at the end
        x = np.append(x, x[0])
        y = np.append(y, y[0])

        return [Point(x_, y_, 0) for x_, y_ in zip(x, y)]

    @Attribute
    def points(self):
        """Apply x-translation and rotation to raw_points"""

        rx = radians(self.x_rotation)
        ry = radians(self.y_rotation)
        rz = radians(self.z_rotation)

        # Rotation matrices
        Rx = np.array([[1, 0, 0],
                       [0, cos(rx), -sin(rx)],
                       [0, sin(rx), cos(rx)]])

```

```
        Ry = np.array([[cos(ry), 0, sin(ry)],
                       [0, 1, 0],
                       [-sin(ry), 0, cos(ry)]])

        Rz = np.array([[cos(rz), -sin(rz), 0],
                       [sin(rz), cos(rz), 0],
                       [0, 0, 1]])

        R = Rz @ Ry @ Rx

        transformed_points = []
        for p in self.raw_points:
            # Apply translation in x
            local_vec = np.array([p.x + self.x_translation, p.y + self.
                y_translation, p.z + self.z_translation])

            # Apply rotation
            rotated_vec = R @ local_vec

            transformed_points.append(Point(*rotated_vec))

        return transformed_points

    @Attribute
    def area(self):
        a = self.width / 2
        b = self.height / 2
        n = self.roundness

        gamma_factor = 4 * (gamma(1 + 1 / n)) ** 2 / gamma(1 + 2 / n)
        cross_area = gamma_factor * a * b
        return cross_area


if __name__ == '__main__':
    obj = HyperEllipse(label="HyperEllipse")
    display(obj)
```

B.4 Hydrogen Tank Class

Listing B.4: LandingGear

```
from parapy.geom import *
from parapy.core import *
from parapy.gui import display
from math import radians, tan, comb
import numpy as np


class Tank(GeomBase):
    """ Class describing hydrogen tank geometry."""

    tank_radius = Input(2)
    tank_length = Input(8)
    tank_x = Input(0)
    tank_y = Input(0)
    tank_z = Input(0)
    tank_rotation = Input(0)
    @Part
```

```python
    def tank_cylinder(self):
        return Cylinder(radius=self.tank_radius, height=self.tank_length/2, hidden=True)

    @Part
    def tank_end(self):
        return Sphere(radius=self.tank_radius,
                      position=translate(self.position, 'z', self.tank_length/2), hidden=True)

    @Part
    def half_tank(self):
        return FusedSolid(shape_in=self.tank_cylinder, tool=self.tank_end, hidden=True)

    @Part
    def mirrored_tank(self):
        return MirroredShape(shape_in=self.half_tank, reference_point=Point(0,0,0), hidden=True)

    @Part
    def tank_i(self):
        return FusedSolid(shape_in=self.half_tank, tool=self.mirrored_tank, hidden=True)

    @Part
    def rotated_tank(self):
        return RotatedShape(shape_in=self.tank_i, rotation_point=Point(0,0,0),
                            vector=Vector(0, 1, 0),
                            angle=radians(90+self.tank_rotation), hidden=True
                            )

    @Part
    def translated_tank(self):
        return TranslatedShape(shape_in=self.rotated_tank, displacement=Vector(self.tank_x, self.tank_y, self.tank_z))


    @Attribute
    def tank_volume(self):
        return self.tank_i.volume

if __name__ == '__main__':
    obj = Tank(label="Tank")
    display(obj)
```

B.5 Fuselage Class

Listing B.5: Fuselage

```python
from parapy.geom import *
from parapy.core import *
from parapy.gui import display

from hyper_ellipse import HyperEllipse


class Fuselage(GeomBase):

```

```
    fuselage_position = Input(2.5)
    fuselage_rotation = Input(1.3)
    fuselage_vertical_position = Input(-0.2)
    fuselage_roundness = Input(3)
    fuselage_volume = Input(160)  # <-- replaced fuselage_length
    min_height = Input(2)

    nose_scale = Input(0.05)
    nose_spacing_factor = Input(1)
    nose_displacement = Input(0.5)
    nose_tip_height = Input(0.35)
    nose_profiles = Input(10)
    nose_tail_roundness = Input(2)

    tail_scale = Input(0.05)
    tail_spacing_factor = Input(1)
    tail_displacement = Input(0)
    tail_tip_height = Input(0.25)
    tail_profiles = Input(10)

    fuselage_width = Input(1)
    fuselage_height = Input(1)
    fuselage_length = Input(1)

    hide_fuselage = Input(False)

    @Part
    def fuselage_profiles(self):
        return HyperEllipse(quantify=2, width=self.fuselage_width,
                            height=self.fuselage_height, roundness=self.fuselage_roundness,
                            n_points=50,
                            x_translation=0, y_translation=self.fuselage_vertical_position,
                            z_translation=child.index * self.fuselage_length + self.fuselage_position,
                            # z_translation=-(child.index - (self.fuse_n_points - 1) / 2.0) * (
                            #                 self.fuselage_length / (self.fuse_n_points - 1)) ,

                            x_rotation=90 + self.fuselage_rotation, z_rotation=90,
                            hidden=True
                            )

    @Part
    def fuselage(self):
        return LoftedSurface(profiles=self.fuselage_profiles, hidden=self.hide_fuselage)

    @Part
    def fuselage_nose_ellipses(self):
        return HyperEllipse(
            quantify=self.nose_profiles,
            width=self.fuselage_width - self.nose_scale * child.index,
            height=self.fuselage_height - self.nose_scale * child.index,
            roundness=self.nose_tail_roundness,
            n_points=self.ellipse_n_points,
            x_rotation=90 + self.fuselage_rotation,
            z_rotation=90,
            z_translation=self.fuselage_position - self.nose_displacement - self.
```

```
                nose_spacing_factor * (
                    child.index / self.nose_profiles) ** (1 / 2),

            y_translation=self.fuselage_vertical_position - self.nose_tip_height *
                 self.nose_scale * child.index,
            hidden=True
        )

    @Part
    def fuselage_tail_ellipses(self):
        return HyperEllipse(
            quantify=self.tail_profiles,
            width=self.fuselage_width - self.tail_scale * child.index,
            height=self.fuselage_height - self.tail_scale * child.index,
            roundness=self.nose_tail_roundness,
            n_points=self.ellipse_n_points,
            x_rotation=90 + self.fuselage_rotation,
            z_rotation=90,
            z_translation=self.fuselage_position + self.fuselage_length + self.
                tail_displacement +
                          self.tail_spacing_factor * (
                                  child.index / 13) ** (1 / 2),

            y_translation=self.fuselage_vertical_position + self.tail_tip_height *
                 self.tail_scale * child.index,
            hidden=True

        )

    @Part
    def fuselage_nose_tip(self):
        return LoftedSolid(profiles=self.fuselage_nose_ellipses[1:], tolerance
            =0.5,
                           hidden=self.nose_tail_hidden)

    @Part
    def fuselage_nose_base(self):
        return LoftedSurface(profiles=[self.fuselage_profiles[0], self.
            fuselage_nose_ellipses[1]], tolerance=0.5,
                             hidden=self.nose_tail_hidden)

    @Part
    def fuselage_tail_tip(self):
        return LoftedSolid(profiles=self.fuselage_tail_ellipses[1:], tolerance
            =0.5, hidden=self.nose_tail_hidden)

    @Part
    def fuselage_tail_base(self):
        return LoftedSolid(profiles=[self.fuselage_profiles[1], self.
            fuselage_tail_ellipses[1]], tolerance=0.5,
                           hidden=self.nose_tail_hidden)

if __name__ == '__main__':
    obj = Fuselage(label="Fuselage")
    display(obj)
```

Appendix C

Additional Figures

C.1 Sensitivity Section Plots

C.2 Dihedral

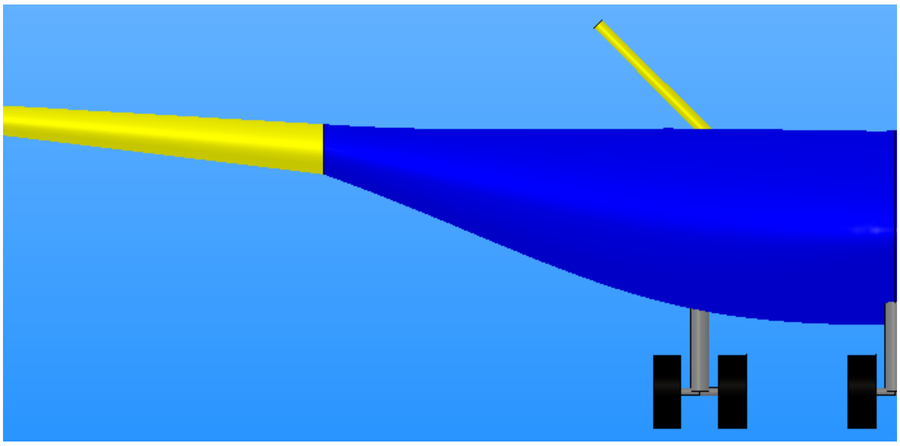

(a) $\Gamma = 5°$

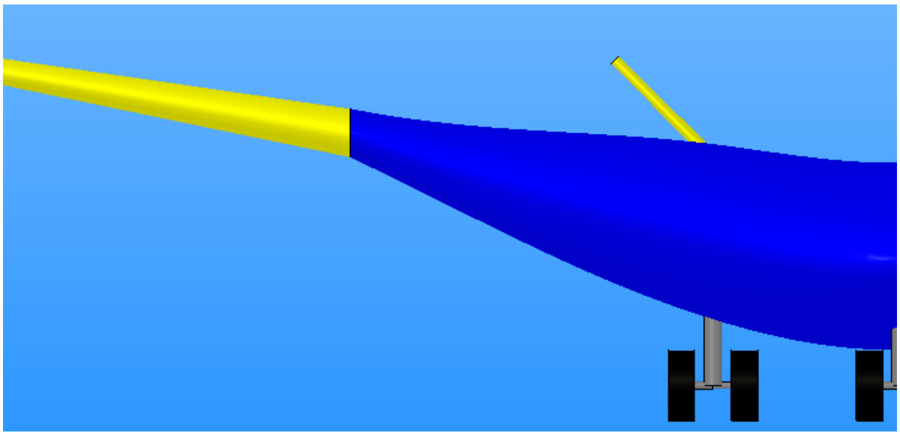

(b) $\Gamma = 10°$

Figure C.2: Frontal view of $\chi = 0.5$ with a change in dihedral

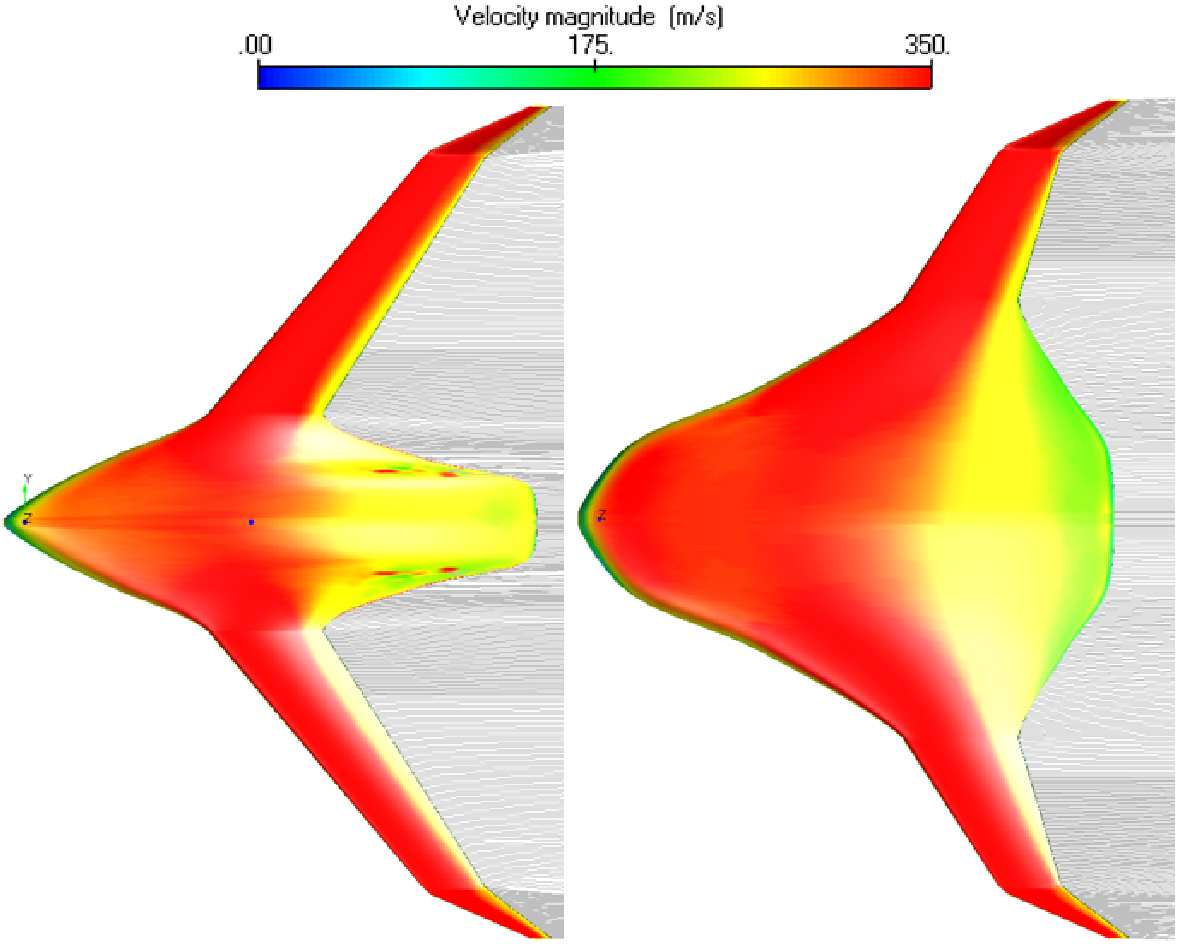

Figure C.1: Upper surface velocity distribution for the χ = 0.3 configuration (left) and the χ = 0.6 configuration (right), with a constant root chord

Appendix D

Simplified UML Diagram

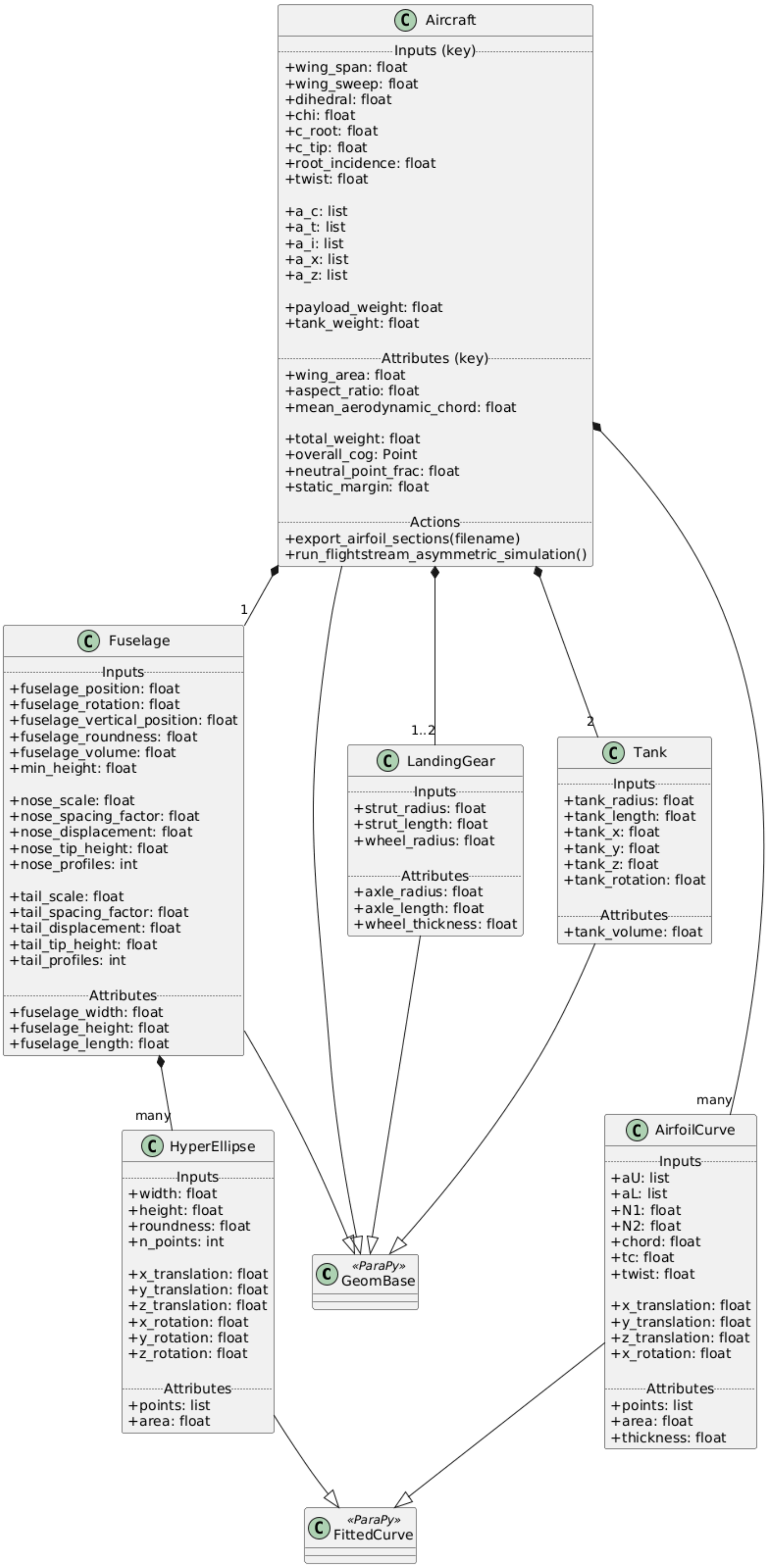

Figure D.1: Simplified Unified Modelling Language (UML) diagram for the ParaPy application